Energy Harvesting in Flexible and Semi-transparent Hydrogenated Amorphous Silicon Solar Cells

by

Ruifeng Yang

A thesis
presented to the University of Waterloo
in fulfillment of the
thesis requirement for the degree of
Doctor of Philosophy
in
Electrical & Computer Engineering

Waterloo, Ontario, Canada, 2016

I hereby declare that I am the sole author of this thesis. This is a true copy of the thesis, including any required final revisions, as accepted by my examiners.

I understand that my thesis may be made electronically available to the public.

Abstract

The goal of this study is to design, characterize, and fabricate efficient hydrogenated amorphous silicon (a-Si:H) photovoltaic (PV) modules, and semi-transparent solar cells on thin, mechanically flexible, optically transparent plastic substrates for energy harvesting applications. The cells are deposited on thin flexible plastics at low temperature (120∼150 °C).

In the first part of study, a-Si:H n-i-p solar cells were fabricated using a plasma enhanced chemical vapor deposition (PECVD) and the deposition conditions were optimized to maximize their efficiency. To improve light absorption, we engineered the front window layer by optimizing p-layer thickness and bandgap (E_g). The best a-Si:H n-i-p solar cell showed open circuit voltage (V_{oc}) of 0.67 V, short circuit current density (J_{sc}) of 7.92 mA/cm^2, fill factor (FF) of 53.73 %, and energy conversion efficiency (η) of 2.86 %. Using developed deposition recipes, the a-Si:H PV modules were designed and fabricated on a 10×10 cm^2 polyethylene-naphthalate (PEN) substrate which consists of 72 rectangular cells. The sub-cells were connected in series forming eight strings with connection pads at the ends, so that the strings of 18 sub-cells were connected in parallel using the external blocking diodes. The typical a-Si:H PV module showed V_{oc} of 12.78 V, J_{sc} of 8 mA/cm^2, FF of 53.8 %, and average η of 3.05 %. The PV module performance is similar to that of individual solar cells, which means good scalability of our module fabrication process.

In the second part, a-Si:H n-i-p solar cells were inverted to fabricate a-Si:H p-i-n solar cells. In this device structure, p-type buffer-layer was introduced to improve the interface between aluminum doped zinc oxide (AZO)/p-layer. The optimum device showed V_{oc} of 0.885 V, J_{sc} of 8.88 mA/cm^2, FF of 52.01 %, and η of 4.09 %.

In the last part of this study, semi-transparent solar cells were fabricated both on glass and plastic substrates to demonstrate feasibility of building integrated photovoltaics (BIPV), based on the a-Si:H p-i-n cells in the second part. To overcome the mechanical stress inside films between AZO and plastic, the barrier-layer coating was used to prevent the delamination which is frequently encountered between plastic substrate and transparent conductive oxide (TCO) layer. Our semi-transparent a-Si:H solar cells showed the η of 4.98 % and 4.77 % for the cells fabricated on glass and plastic substrates, respectively. In addition, the semi-transparent a-Si:H p-i-n solar cell was also used as radiation detector within the visible part of the spectrum. From the Ne spectral lines, the micro-plasma spectral from radiation detector obtained response comparable with fiber optic detector.

Acknowledgements

First and foremost, I would like to thank my supervisor Professor Andrei Sazonov. His insight and guidance have made my study exciting. Besides the professional training of conducting research given by Professor Andrei Sazonov, he also taught me important personal lessons, which will be invaluable in all of my future endeavours.

I would also like to thank all my committee members Professor Siva Sivoththaman, Professor Bo Cui, Professor Vassili Karanassios, and Professor Nazir Kherani for their time and patience in reviewing my work.

I would like to express my appreciation to Professor Mehmet Güneş (Mugla Üniversitesi, Turkey) and Dr. Yuri Vygranenko (CTS-UNINOVA, Portugal) for discussion and collaboration.

Furthermore, I would like to express my gratitude to Giga-to-Nanoelectronics Centre (G2N) lab manager, Richard Barber, for his efforts in G2N lab. I am also thankful to all my colleagues. Special thanks to Dr. Czang-Ho Lee and Zhen Gao for their help during my research. I am also grateful to Alireza Khosropour, Muhammad Ali Martuza, Albert Chen, Shuai Na, Bright Iheanacho, Zhenhao Li, and Dr. Minoli Pathirane for their valuable discussions.

I also owe a lot to my friends and family. I thank Shengying for how wonderful she has made my life since meeting her. Finally, I don't know where I would be without Mum and Dad, who I know have been behind me every step of the way, for this I am grateful beyond words.

Table of Contents

List of Tables

List of Figures

List of Abbreviations

η	Energy conversion efficiency
c-Si	Crystalline silicon
E_g	Bandgap energy
CdTe	Cadmium telluride
CIGS	Copper indium gallium selenide
a-Si:H	Hydrogenated amorphous silicon
CIS	Copper indium selenide
$CuGaSe_2$	Copper gallium selenide
ITO	Indium tin oxide
PV	Photovoltaics
PEN	Polyethylene-naphthalate
BIPV	Building-integrated photovoltaics
PECVD	Plasma enhanced chemical vapor deposition
RIE	Reactive Ion Etching

EQE	External quantum efficiency
TCO	Transparent conductive oxide
DOS	Density of states
E_c	Conduction band edge
E_v	Valence band edge
E_f	Fermi energy
μ_p	Hole mobility
μ_n	Electron mobility
μ_D	Drift mobility
α	Absorption coefficient
a-SiC:H	Hydrogenated amorphous silicon carbide
a-SiGe:H	Hydrogenated amorphous silicon germanium
μc-Si:H	Hydrogenated micro-crystalline silicon
AZO	Aluminum doped zinc oxide
SnO_2	Tin oxide
V_{oc}	Open circuit voltage
I_{sc}	Short circuit current
J_{sc}	Short circuit current density
FF	Fill factor
R_{sh}	Shunt resistance

R_s	Series resistance
FTIR	Fourier transform infrared spectroscopy
PET	Polyethylene-terephthalate
PI	Polyamide
AFM	Atomic force microscopy
RMS	Root mean square
σ_{dark}	Dark conductivity
σ_{photo}	Photo-conductivity
SiH_4	Silane
H_2	Hydrogen
PH_3	Phosphorene
B_2H_6	Diborane
CH_4	Methane
IPA	Isopropanol
a-SiO_x:H	Hydrogenated amorphous silicon oxide
a-SiN_x:H	Hydrogenated amorphous silicon nitride
SF_6	Sulfur hexafluoride
sccm	Standard cubic centimeters per minute
ICP	Inductively coupled plasma
CCD	Charge coupled device

Chapter 1

Introduction

1.1 Overview of solar cell

The first practical solar cell was demonstrated in 1954 by Chapin *et al.* from Bell laboratory [1]. It consisted of small strips of doped single crystal silicon, which exhibited energy conversion efficiency (η) of 6 %. Crystalline silicon (c-Si) is the key semiconductor that drive the first generation of solar cell due to well developed materials science and device theory and its bandgap energy (E_g) of 1.1 eV well-suited for the solar spectrum.

The second generation of solar cell, which has been widely studied as an alternative to the first generation solar cell, is based on thin film materials. The main absorber thickness of thin film solar cells are in the range of 0.1$\sim$2 μm depending on the type of thin film material, which is much thinner compared to that of c-Si solar cells (200$\sim$400 μm) (Figure 1.1(a)). The absorbing layers can be deposited on large-area substrates such as low-cost glass (Figure 1.1(b)). Indeed, thin film solar cells can also made on top of plastic substrates,

which is possible at low-temperature processes (Figure 1.1(b)). Three common thin film materials for the second generation solar cell technology are Cadmium telluride (CdTe), Copper indium gallium selenide (CIGS), and Hydrogenated amorphous silicon (a-Si:H).

Figure 1.2 shows (a) three common thin film solar cell structures and (b) the efficiency vs. bandgap of various solar cell materials. CdTe is a poly-crystalline thin film semiconductor with direct bandgap and E_g of 1.4∼1.5 eV which is ideally suited for absorbing the solar spectrum (Figure 1.2(b)). CdTe solar cells have become the main thin film solar cells showing in manufacturing η of ∼21 % [3]. However, the main disadvantage of CdTe solar cell is high toxicity of Cd if released [4]. Another poly-crystalline thin film semiconductor, CIGS, is composed of a solid solution of Copper indium selenide (CIS) and Copper gallium selenide ($CuGaSe_2$). Depending on the ratio of the two compounds in the solution, this solar material yields E_g that can vary from 1.0∼1.7 eV. The lab-scale CIGS solar cells have already shown η of ∼20.5 % [3], which makes this thin film solar technology very attractive. However, main limitation of CIGS technology is high-cost and shortage of indium, which is a rare metal mainly used for display pixel electrode [4]. The last thin film solar material, a-Si:H, consists of disordered network of Si and H atoms deposited from silane (SiH_4) plasma at relatively low deposition temperatures (100∼300 °C) compared to those of the other two thin film solar materials (∼600 °C). Unlike c-Si, a-Si:H has direct bandgap with E_g near 1.7∼1.8 eV [5]. This specific property permits a-Si:H absorber to be much thinner than c-Si for solar cell applications due to higher absorption in the visible wavelength range [5].

Although the η of a-S:H solar cells is lower (lab-scale ∼10 % & ∼7 % in manufacturing) compared to other thin film solar cells (lab-scale ∼20 %), a-Si:H is preferred to CdTe and CIGS in terms of material science and manufacturing technology, which are similar to those

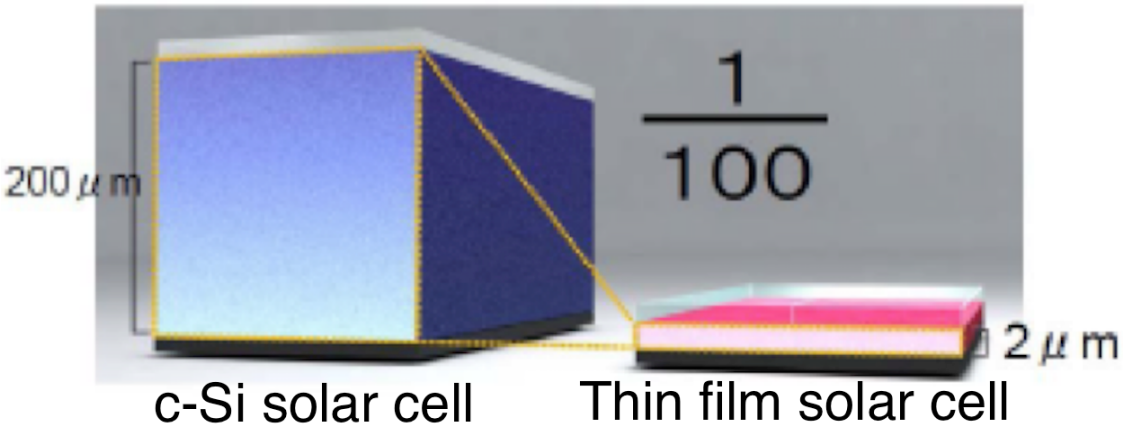

(a)

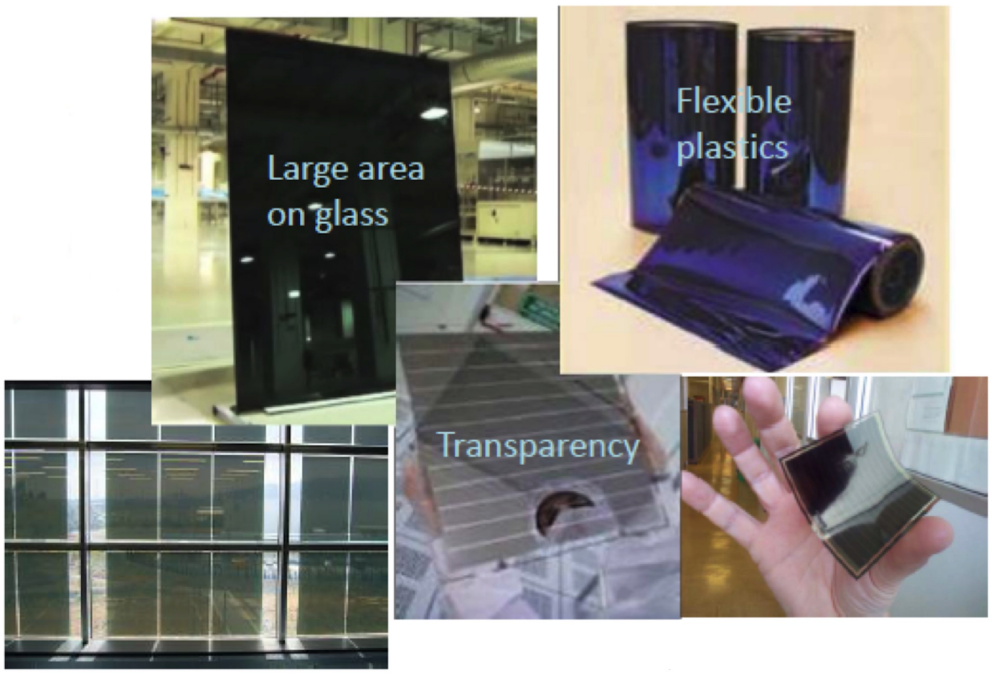

(b)

Figure 1.1: (a) Comparison of absorbing layer thickness between c-Si and thin film solar cells and (b) thin film solar modules on various substrates [2].

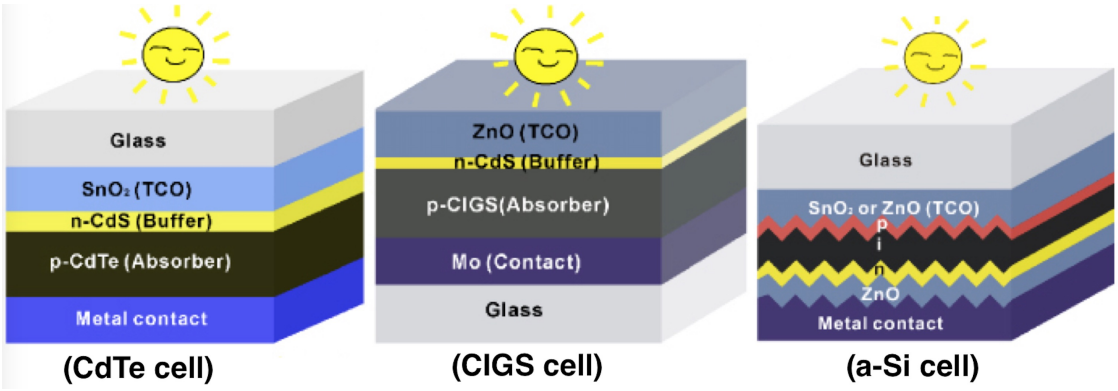

(a)

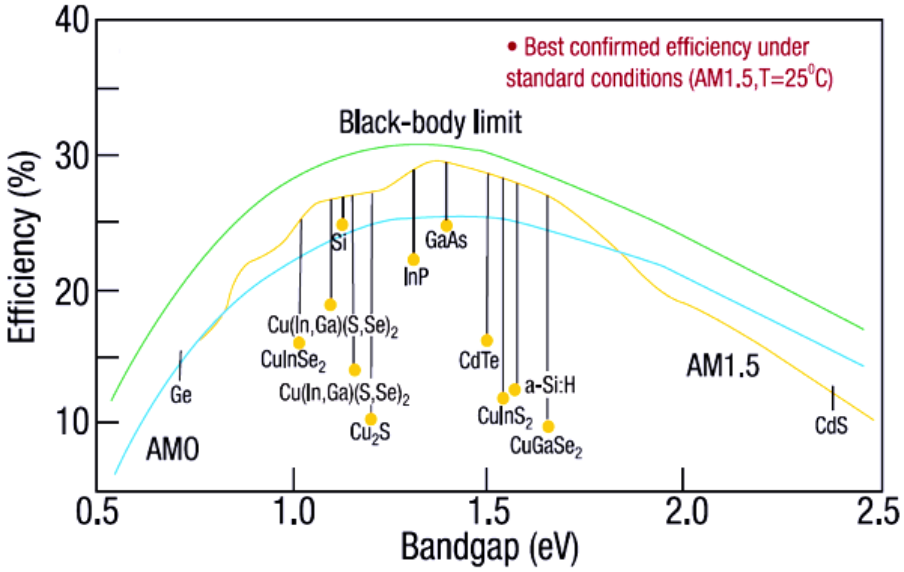

(b)

Figure 1.2: (a) Three common thin film solar cell structures and (b) the efficiency vs. bandgap of various solar cell materials (modified from [2]).

of c-Si. a-Si:H solar cells/modules can be fabricated on large-area glass substrates without any consideration of thermal budget and are suitable for both indoor as well as outdoor applications. Another advantage of a-Si:H is that it can be deposited on the wide range of

substrates (including flexible, curved, and roll types) due to its low-temperature deposition process.

1.2 PV market

Photovoltaics (PV) products have experienced exponential growth for over two decades. During this period, PV has expanded from small-scaled power applications to mainstream electricity source. Figure 1.3(a) shows the growth of global annual production from 2005 to 2014 for key countries [6]. One can see that the growth of global PV production increased about 44 % from 2000 to 2014. The total cumulative PV installations in 2014 in Europe amounted to 48 % of world's total (compared to 58 % in 2013), and in China/Taiwan to 17 % (compared to 13 % in 2013) (Figure 1.3(b)) [6].

Meanwhile, the cost of PV has significantly declined due to improvements in the technology and economy of scale. As the acceptance and development of PV continue to gain momentum globally, so does the ability for PV to compete with conventional energy sources. Figure 1.4 shows production capacity and market share for c-Si and thin film PV technologies. The market share of all thin film technologies in terms of the total annual production was expected to stabilize at ∼7 % in 2015 [6]. The share of c-Si based PV technology was now ∼92 % of the total production in 2014 [6] and the market share for thin film PV continues to grow. By the end of 2014, cumulative PV capacity reached 177 gigawatts, sufficient to supply 1 % of global electricity [6].

As an effective strategy to reduce PV prices, inexpensive absorbing materials and/or substrates have been extensively demonstrated by many researchers [9]. By using the low-cost substrate and thin Si, it is possible to significantly reduce the module costs. Due to

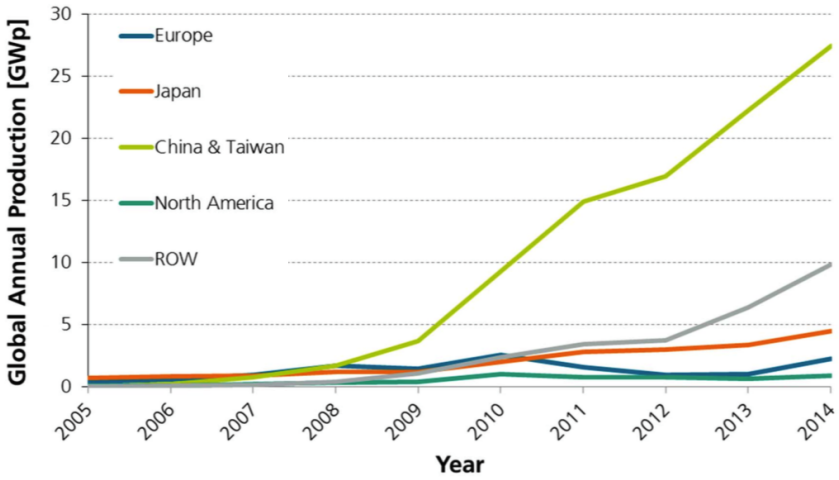

(a)

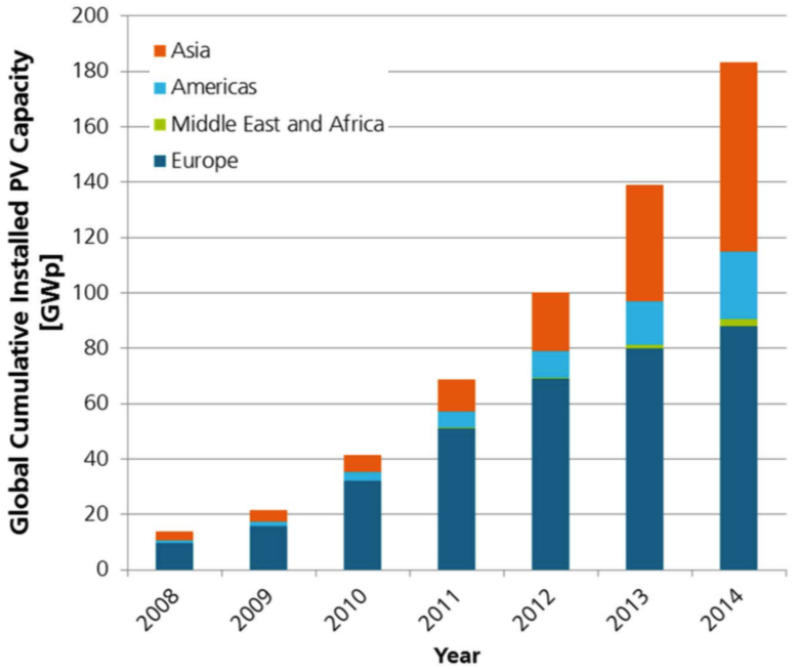

(b)

Figure 1.3: (a) Growth of global annual PV production between 2005 to 2014 and (b) global cumulative PV installation until 2014 (modified from [6]).

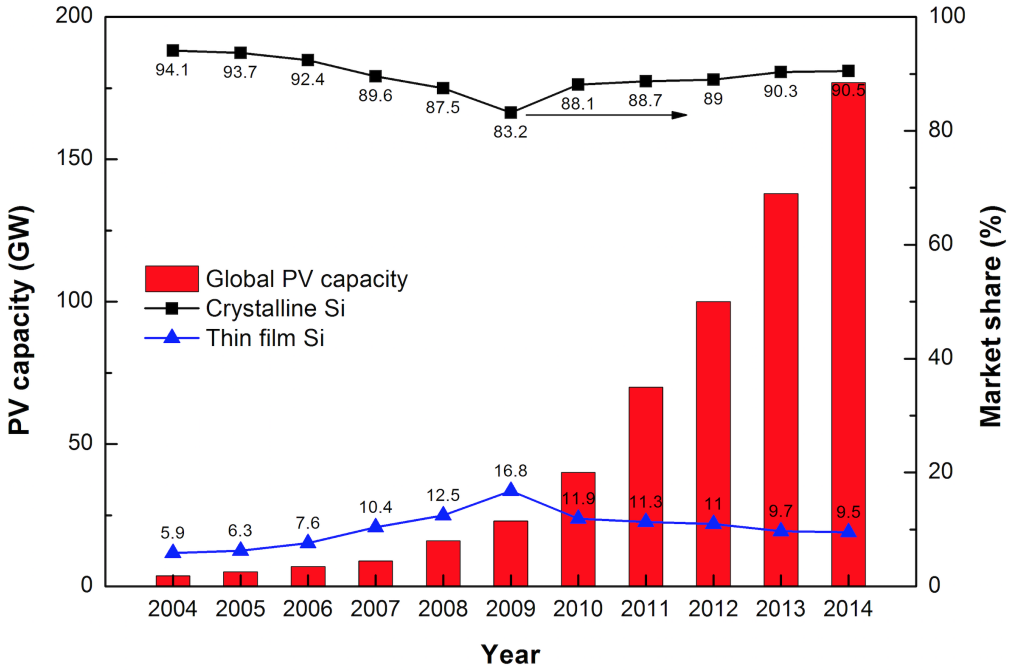

Figure 1.4: Production capacity and market share for c-Si and thin film PV technologies (modified from [6, 7, 8]).

the high cost of producing c-Si wafers, the low-cost thin film materials are thus preferred as shown in Figure 1.5. Clearly, we can realize the advantage of low-cost materials from the cost breakdown data for c-Si and a-Si:H solar cells, showing the raw material portion in total production cost of 52 % cost for c-Si solar cell and only 7 % for a-Si:H solar cell [9, 10].

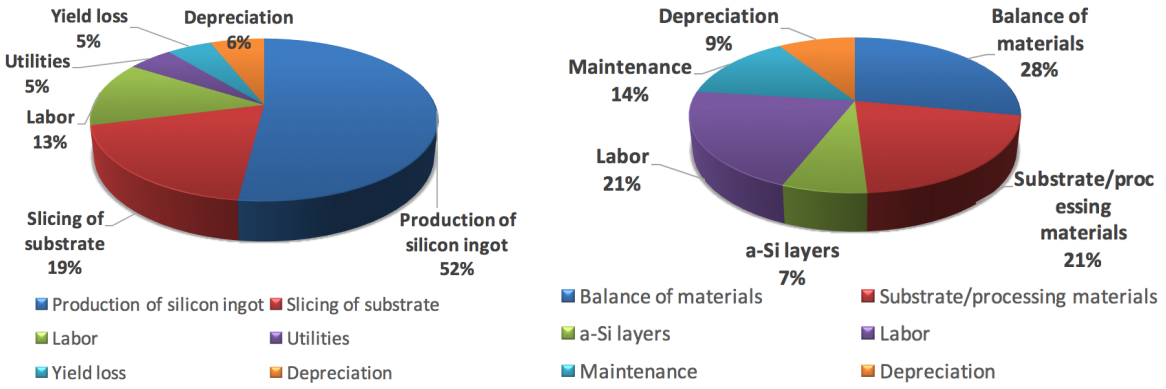

Figure 1.5: Cost breakdown for (a) c-Si and (b) thin film a-Si:H solar cells (modified from [9]).

1.3 Motivation and Objectives

One of the critical metrics for evaluating solar cells is the price-to-performance ratio. Several cost-to-performance phases of a-Si:H solar cell technology are of importance, in order to improve the competitiveness of a-Si:H solar cells on the market, which can be distributed into the following aspects:

1. Major performance improvement is expected by increasing the output current of the solar cells [11]. This increase can result from improved light management (reduction of light absorption loss) such as light absorption and light trapping.
2. While device-grade a-Si:H deposition is the most important part of solar cell fabrication, the total cost of the complete PV module is also highly affected by other fabrication steps. These include the front transparent conductive oxide (TCO) electrode deposition, the multi-layer back electrode deposition, laser scribing for the sub-cell connection, encapsulation, and framing. The choice of overall sequence of

fabrication steps and deposition techniques are determined by the solar cell structure and PV module design. The general trend is to increase the substrate size by lowering the cost per unit area.

a-Si:H solar cells have gained significant research interests as a cheap alternative given their low manufacturing costs compared to c-Si solar cells as already mentioned in section 1.2. Although their energy conversion efficiency (η=10.1$\pm$0.3 %) is lower than that of c-Si solar cells (η=25$\pm$0.5 %) [12, 13, 14], specific material properties and low-temperature fabrication processes of a-Si:H solar cells allow them to be fabricated over various substrates from small-area glass to large-area glass and even over flexible plastic substrates.

Flexible PV devices offer an alternative energy source for both indoor and outdoor applications. In general, the advantages over existing technologies are clear [15].

1. Highly flexible: The true mechanical flexbility of flexible PV modules makes them suitable for applications with different shapes, sizes, and for designing novel PV products.
2. Integratable: The "reel to reel" fabrication process allows PV production with various lengths and widths, which is highly attractive for integrated applications.
3. Light-weight: The PV modules on flexible substrates for applications where low weight is important.
4. Unbreakable: Unlike conventional c-Si PV modules, which are based on fragile glass substrates, flexible PV modules are made of thin polymers, which are tough, durable, and safe to use.
5. Environmentally friendly: Flexible substrates are recyclable. The energy payback time of flexible products is 3-5 times shorter than that of the products based on conventional PV technologies [15].

Compared with ultra-thin c-Si solar cells (lightweight and likely flexible), a-Si:H solar cells deposited on flexible plastic substrates are less to be damaged by abrasions and vibrations. In this thesis, we have studied on a-Si:H thin film solar cells fabricated on flexible plastic substrates at low deposition temperature with the goal to demonstrate efficient PV modules on plastic substrate.

The maximum area of c-Si solar cells is constrained by the size of silicon wafer, which is currently 113 inch square. In order to make a c-Si solar module, c-Si solar cells should be connected each other. However, a-Si:H solar cells/modules can be fabricated up to 3.1×2.9 m^2 (in 2014) with series connection of a-Si:H sub-cells using simple laser patterning technique. As shown in Table 1.1, the prices of glasses and polyethylene-naphthalate (PEN) are much more competitive than that of single crystal silicon wafers.

Table 1.1: Prices of different types of wafer in similar size (modified from [16]).

Wafer type	Diameter (mm)	Thickness (μm)	Price ($)
Ultra-thin silicon	100	75	559
Silicon	100	335	150
Soda lime glass	100	550	36.9
PEN (plastic)	100	75	$\sim$10

Given increasing demand in building energy conservation, building-integrated photovoltaics (BIPV) has attracted considerable attention [17, 18]. BIPV is highly suitable for high density cities since PV systems are attached to building itself without using additional land [19]. Many of BIPVs are just opaque (c-Si based) PV glazed with window glass on-site, which strains the definition of integrated. Semi-transparent PV windows will not only be a sensible idea but a realistic one due to their light admission characteristics. With the intended application of semi-transparent BIPVs, a-Si:H based BIPV becomes a great candidate because it offers advantages such as large-area deposition, high relia-

bility, and semi-transparency (Figure 1.6) [20, 21, 22]. With the goal of demonstrating semi-transparent BIPV and car window mounted PV, we have investigated highly efficient semi-transparent thin film solar cells that are fabricated on both glass and plastic substrates.

(a) (b)

Figure 1.6: (a) Opaque (c-Si based) and (b) semi-transparent (a-Si:H based) BIPVs.

1.4 Organization of the Thesis

Chapter 2 reviews the properties of a-Si:H thin film critical for solar cell application. The device physics of a-Si:H solar cell is also compared to that of c-Si solar cell.

In Chapter 3, fabrication processes (including plasma enhanced chemical vapor deposition (PECVD) and sputtering deposition) are described. An description of various analytical methods (including conductivity analysis, solar cell I-V characteristics, and external quantum efficiency (EQE) measurement) used in this work is given.

Chapter 4 is devoted to fabrication and characterization of a-Si:H solar cells. In order

to investigate an impact of electrodes on the device performance, device modelling is first involved. Then, a-Si:H n-i-p solar cells are fabricated on both glass and plastic substrates were investigated. In addition, PV modules are demonstrated on plastic substrate.

In Chapter 5, a-Si:H p-i-n solar cells fabricated on glass substrate are investigated. Here, the substrate configuration used in Chapter 4 is inverted to superstrate configuration. p-type buffer-layer engineering is carried out in order to improve solar cell performance.

Chapter 6 studies the semi-transparent a-Si:H p-i-n solar cells fabricated by substituting back metal contacts with TCO film. While transferring semi-transparent cell from glass to plastic substrate, the barrier-layer is introduced to obtain improved device performance. In addition, our PV devices are demonstrated as a detector to measure the micro-plasma spectral response compared to fiber optic detector under Ne spectral lines, showing efficacy of functional diversion of PV devices.

Lastly in Chapter 7, we draw the conclusion of the study and discuss the future work.

Chapter 2

Literature Review and Background

In this chapter, we review the background of a-Si:H thin films and a-Si:H solar cells. At first, we overview the a-Si:H solar cell development in section 2.1. The atomic structure, electrical and optical conductivity, and doping mechanism for a-Si:H thin films are reviewed in section 2.2. In section 2.3, PECVD system and its deposition parameters are discussed. The following section 2.4 describes the a-Si:H solar cell operation (we compare two typical Si based solar cells, which are c-Si solar cell and a-Si:H solar cell), ideal solar cell model, I-V characteristics with standard test spectrum, and configurations. In the last section 2.5, the background of PV module is described.

2.1 Overview of a-Si:H solar cell development

Carlson and Wronski demonstrated the first single-junction a-Si:H p-i-n solar cell in 1976 [23]. Their a-Si:H solar cell demonstrated an energy conversion efficiency of 2.4 %.

Most of the research on a-Si:H solar cells was concentrated on developing and characterizing a-Si:H alloys in the 1980s. A p-type hydrogenated amorphous silicon carbide (p-a-SiC:H) was introduced in a-Si:H solar cells as p-type window layer [24]. High E_g of p-a-SiC:H layer allowed more light to pass into absorber layer. Surface textured substrates were incorporated to improve the optical absorption [25]. At the second half of the 1980s, the single-junction a-Si:H p-i-n PV modules were introduced to the market. By the end of this decade, the PV module was expanded to between 0.1 and 0.3 m^2 with a stable efficiency up to 5 %.

In the 1990s, the main effort of research and manufacturing was dedicated towards achieving 10 % stabilized PV module efficiency and high process throughput. Several companies optimized and implemented a hydrogenated amorphous silicon germanium (a-SiGe:H) alloy in tandem (BP Solar [26], Sanyo [27], Fuji Electric [28]) and triple-junction (United Solar [29]) solar cell structures. The emerging a-Si:H based PV modules developed in the 1990s were thus multi-junction structures. The module size reached 1 m^2 with the stabilized efficiency of 6$\sim$7 %. μc-Si:H deposited by PECVD techniques appeared as a new candidate for low bandgap material in multi-junction a-Si:H solar cells. The concept of micromorph tandem solar cell, which consists of a-Si:H top cell and μc-Si:H bottom cell, was introduced by the University of Neuchâtel in 1994 [30]. The micromorph multi-junction solar cells showed stable efficiencies in the range of 11$\sim$12 % [31, 32].

At the turn of the century, research effort was devoted to understanding and improving light trapping techniques, where surface texture and novel TCO materials play an important role in improving the optical path. These efforts have resulted in the industry-wide adoption of novel deposition techniques for conductive ZnO as an alternative TCO material to tin oxide (SnO_2) [33, 34]. Several equipment manufacturers have started developing

commercial production machines for the fabrication of thin film Si solar cells [35]. Today, the fully automated systems and large area deposition lines for a-Si:H based solar module production are over 1 m^2.

Recently, F.-J. Haug reported μc-Si n-i-p solar cells on textured PEN plastic with a stable 8.4 % efficient [36]. The best stabilized efficiency of a-Si:H p-i-n solar cell on textured SnO_2 coated glass have been reported to be 10.11 % by Takuya Matsui [12].

Nowadays, BIPV has received much attention due to the increasing demand in building energy conservation. It can offer an efficient method of installing the required amount of PV without using additional space. In terms of the application aspect of solar cell to BIPV, a-Si:H solar cells take an advantage over c-Si based solar cells because the former can be semi-transparent which enables sun light admission into the building interior. Thus, it is expected that semi-transparent a-Si:H based PV would be able to replace traditional window glass as an energy harvesting for BIPV system. JungWook Lim reported an a-Si:H semi-transparent solar cell with transmittance of 48.75 % and efficiency of 5.36 % [37].

2.2 Hydrogenated amorphous silicon

2.2.1 The atomic structure of a-Si:H

The Si-Si bond structure and possible defects in c-Si and a-Si:H is shown in Figure 2.1. Two Si materials are based on covalent Si-Si bonds in spite of the differences of their micro-structure. The structure of c-Si shows regular lattice of Si atoms (Figure 2.1(a)). Because the number of Si-Si bonds per atom in the atomic structure is called the coordination number or coordination, the coordination number of c-Si is four (also called fourfold

coordinated). Point defects in c-Si are most commonly vacancies, interstitial atoms, or extrinsic defects (Figure 2.1(a)). Unlike c-Si, a-Si:H consists of a random network of Si and H atoms (Figure 2.1(b)), which lacks long range order in a bulk-material. The small deviations from bonding lengths and angles between the neighboring atoms lead to the loss of local ordered structure in a-Si:H. As a result, a defect in a-Si:H is defined as an atom that is over- or under-coordinated in terms of the bonding of Si atoms.

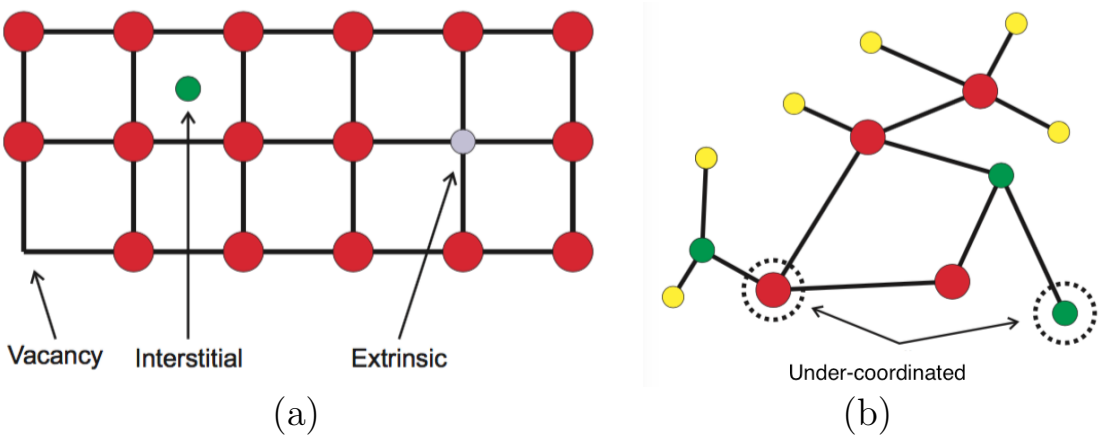

Figure 2.1: Schematic diagram of Si-Si bonds and possible defects in (a) c-Si and (b) a-Si:H.

An under-coordinated Si atom in a-Si:H is a dangling bond which may be neutral or charged [38]. H atoms passivate dangling bond defects as well as increase in E_g due to higher Si-H binding energy (3.55 eV) than Si-Si binding energy (3.26 eV) [39]. Typical device-grade a-Si:H thin films have an Eg of 1.7∼1.8 eV with a H content of ∼15 % [5].

Its higher E_g allows a-Si:H to be a more efficient light absorber below 700 nm for solar cell applications. However, due to existence of deep gap energy states related to dangling bonds, a-Si:H solar cells show lower energy conversion efficiency compared to c-Si solar cells [39, 40]. All of these effects can be explained with density of states (DOS) of a-Si:H.

2.2.2 Electrical properties

Typical conduction of electrons (holes) in a-Si:H occurs via trapping and de-trapping of carriers in the band tail states as shown in Figure 2.2.

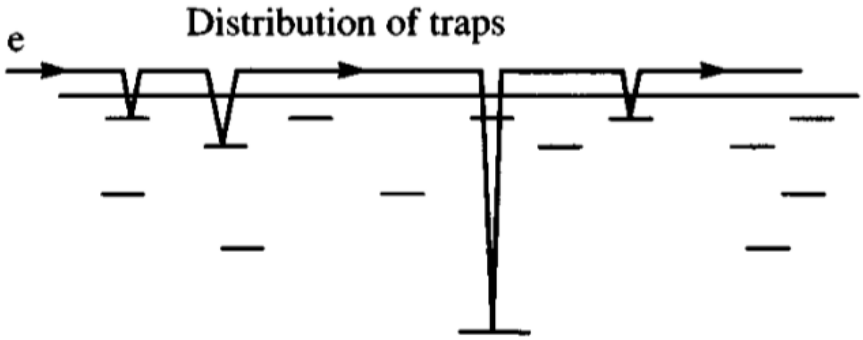

Figure 2.2: The explanation of the distribution of trap [5].

The trap states in the band tails thus affect electronic transport of mobile carriers. As a result, the drift mobility (μ_D) is lower than the band mobility (μ_0) in the conduction states and provides a sensitive means of exploring the DOS distribution in the band tail from equation (2.1) [5]. This definition is also a universal feature of amorphous semiconductors [41].

$$\mu_D = \mu_0 \frac{\tau_{free}}{(\tau_{free} + \tau_{trap})} \tag{2.1}$$

Here: μ_D is drift mobility, μ_0 is band mobility, $\tau_{free}/(\tau_{free}+\tau_{trap})$ is fraction of time that the carrier spends in the traps.

2.2.3 Optical properties

Figure 2.3 shows (a) absorption coefficient (α) of a-Si:H as a function of photon energy compared to c-Si and (b) determination of bandgap energy for intrinsic a-Si:H, p-type a-SiC:H, and a-SiGe:H films [42]. In the visible part of the solar spectrum, a-Si:H absorption coefficient is almost 100 times higher than c-Si (Figure 2.3(a)). This means that a 1 μm thick a-Si:H layer is sufficient to absorb 90 % of the usable solar energy.

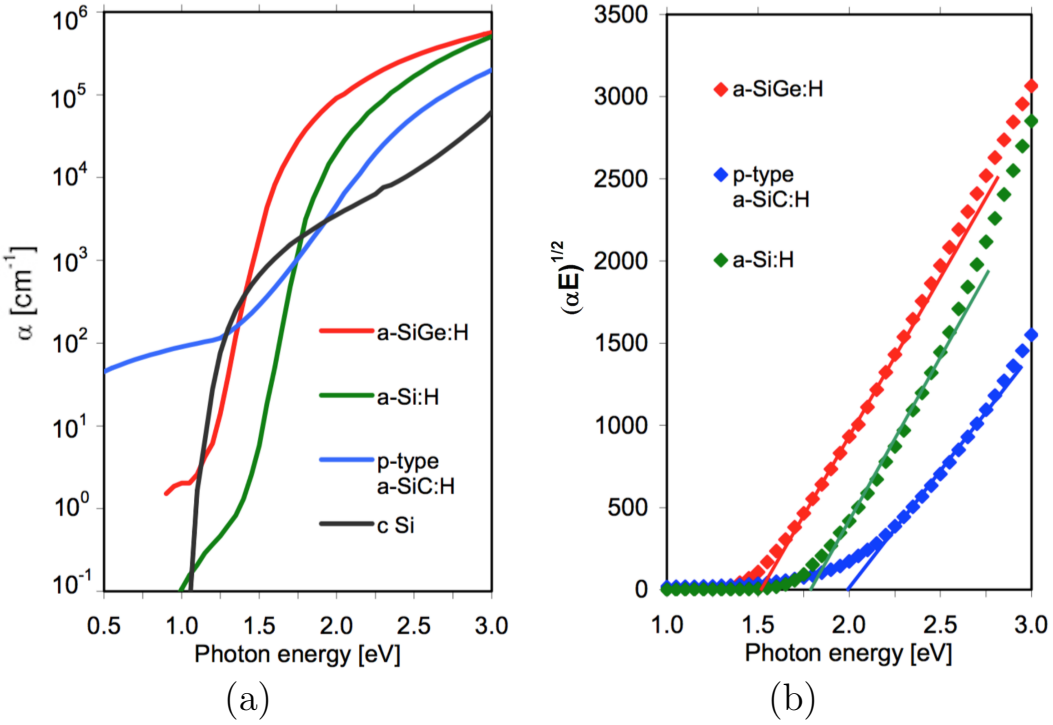

Figure 2.3: (a) Absorption coefficient (α) of a-Si:H as a function of photon energy compared to c-Si and (b) determination of bandgap energy for intrinsic a-Si:H, p-type a-SiC:H, and a-SiGe:H films (modified from [42]).

In practice, the thickness of a-Si:H solar cells is ~300 nm, which is about 1000 times thinner than that of typical c-Si solar cell. In addition, the E_g of a-Si:H can be easily

controlled by isovalent impurities such as Ge for low E_g and C for high E_g [42]. The E_g for device-quality intrinsic a-Si:H film of ∼1.7 eV, p-type a-SiC:H film of ∼1.95 eV, and a-SiGe:H film of ∼1.52 eV, is shown in Figure 2.3(b) [42].

2.2.4 The doping mechanism

In c-Si, a dopant atom is constrained in its fourfold coordination by occupying a lattice site, and weakly bonded electrons or holes are then readily excited from shallow energy states to the conduction or valence band, respectively, at room temperature. The doping mechanism in a-Si:H is different from that of c-Si. R. A. Street discussed that dopants could be incorporated into an a-Si:H network in a similar state if they were ionized before incorporation [5]. In this way, a phosphorus atom would become positively charged and a boron atom would become negatively charged. These states are shown in equation (2.2) & (2.3), where P_x and B_x are noted as phosphorus or boron atom with x electrons present in its outer shell. After incorporation in this manner, dopant atoms would be free to act as acceptors or donors in a similar manner to their behaviour in c-Si.

$$P_5 \rightarrow P_4^+ + e \tag{2.2}$$

$$B_3 \rightarrow B_4^- + h \tag{2.3}$$

The doping efficiency in a-Si:H is very low which is determined by the fraction of dopant atoms with fourfold coordination. The formation of defect compensated donors by phosphorus atoms (defect compensated acceptors by boron atoms) is the major doping mechanism in a-Si:H. The most important result of this model is that doping of a-Si:H

creates dangling bonds. Doped a-Si:H has a two or three orders of magnitude higher defect density than intrinsic a-Si:H.

2.3 PECVD a-Si:H growth

2.3.1 Deposition system and mechanism

The widely used deposition system to produce a-Si:H thin films is PECVD with excitation frequency of 13.56 MHz. The plasma provides an energy source to dissociate SiH_4 gas. The growth of a-Si:H films is accomplished by attaching reactive deposition species (radicals) to the substrate surface. By plasma assistance, the growth of a-Si:H can be made at low deposition temperature (100∼250 °C). The low temperature process allows the use of such substrates as glass and plastic [40].

The PECVD system contains five main parts (Figure 2.4) [39]:

- High vacuum reaction chamber with coupled parallel electrodes, RF power feed through substrate holder and substrate heating assembly.
- Gas handling system which consists of flow controllers and gas valves to handle gas flows required for the deposition of the intrinsic and/or doped layers.
- Pumping system which consists of turbo pump and mechanical rotary pump, which can handle reactive gasses.
- Exhaust system with a scrubber or a burn box to process the outlet gasses.
- Electronic and control part that consists of DC or RF power generator with matching box, and vacuum pressure and temperature gauging.

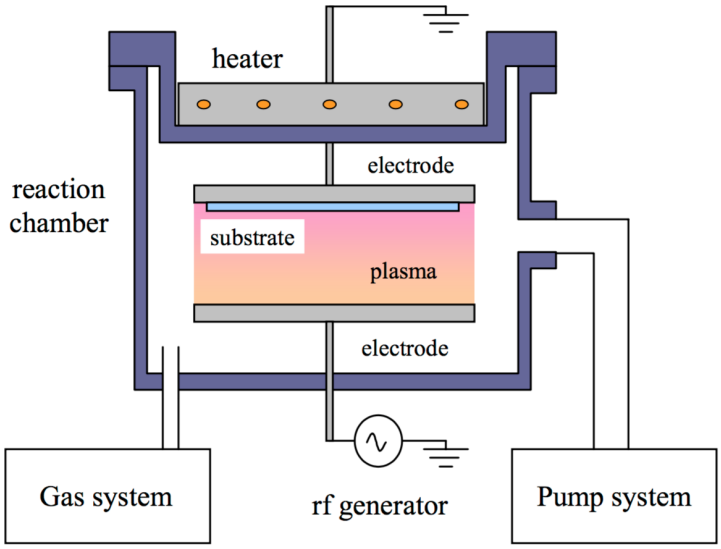

Figure 2.4: Schematic representation of PECVD system [43].

Plasma deposition of a-Si:H layers can be described as a four-step process (Figure 2.5) [43]:

1. Primary reactions where SiH_4 molecules are decomposed by electron impact excitation, generating various neutral radicals, molecules, ions, and electrons.
2. Secondary reactions in plasma among molecules, ions, and radicals which result in the formation of reactive species in large Si and H clusters. Neutral species diffuse to the substrate, positive ions bombard the growing film, and negative ions are trapped within the plasma.
3. Interaction of radicals with the surface of the growing film such as radical diffusion, chemical bonding, or H atoms sticking to the surface.
4. Release of H_2 on the surface and relaxation of the Si network.

Generally, SiH_3 radical is considered to be the one that produces device quality a-Si:H

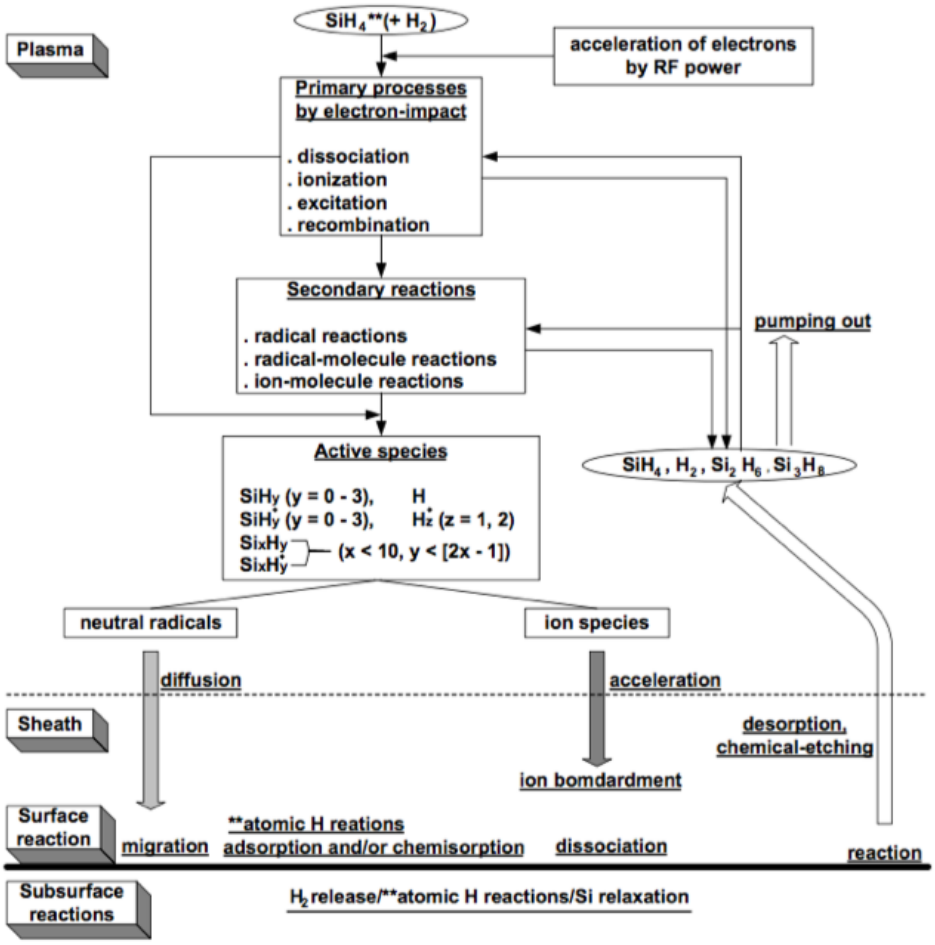

Figure 2.5: Schematic representation of the a-Si:H deposition process [44].

growth [45, 46]. Since most of the growing surface is terminated by hydrogen [47], the SiH_3 radical does not bond to the growing film but diffuses over the surface until it collides with a dangling bond. The SiH_3 radical thus contributes to the growth by collision with the dangling bond [45]. Other radicals do also play an important role in determining the properties of the film although they contribute much less to the growth. The SiH_2 and higher silane radicals (Si_xH_y) have higher sticking coefficients than SiH_3, and can be incorporated directly into the hydrogen terminated surface [5]. However, these radicals

contribute to poor quality films. Therefore, these radicals in the plasma should be avoided.

2.3.2 PECVD parameters

The deposition process is a complex process of radical generation, transport, and surface reactions controlled by deposition parameters such as the gas mixture composition, flow and pressure, the power density and excitation frequency, the substrate temperature, the electrode geometry, etc [48]. This section briefly overviews some deposition parameters that control the properties of a-Si:H during PECVD process.

- Pressure: The pressure required to sustain the plasma is affected by electrode separation. If the pressure is too high (>1 Torr), the secondary reactions yield higher Si_xH_y to be formed along with the SiH_3 radicals within the plasma bulk. This will not only cause formation of macroscopic particles of silicon-containing powder but will also significantly increase the film growth rate. SiH_x would not have sufficient time to diffuse to the substrate, hence it would react with ionized molecules and form polymerized Si_xH_y species (can be negative) [49]. If the pressure is too low, then the mean free path of electrons will be high, and the secondary electrons can reach the anode before colliding with gas molecules, which cannot sustain plasma.
- Electrode gap: The distance between the electrodes also dictates whether the powder formation will prevail over thin film growth or not. At larger electrode separation, SiH_3 diffuses longer to reach the anode [49]. As a result, the probability of powder formation greatly increases. The plasma becomes unstable, which implies that ionization and excitation processes will be diminished. The optimum electrode spacing for thin film deposition has been reported to be 5$\sim$15 cm [50].

- Substrate temperature: The temperature of the substrate surface plays an important role by determining the surface adatom mobility (e.g. SiH_3) with higher temperature breaking weak bonds between atoms at the surface and provide higher amount of energy to SiH_x adatoms. The adatoms can now diffuse across the substrate surface and find a equilibrium positions (lowest free energy spots). Further increase in the substrate temperatures results in the loss of hydrogen from the surface and in the increase of dangling bonds, which raises sticking coefficient of the surface and thus decreases the surface adatom mobility [49].
- Power density: Higher power density increases electric fields at the plasma sheath. This causes positive ions to bombard on to the substrate surface due to acceleration by electric field. As a result, the dangling bond density in deposited film increases. Additionally, large Si_xH_y species will bond to the substrate surface due to their low surface mobility. As a consequence, the combination of these two effects leads to form a porous film with poor electrical and structural properties.
- Gas flow rate: A decrease in the gas flow rate increases the residence time of heavy and short lifetime radicals in the plasma. On the other side, the gas utilization rate is low at higher flow rates [49].
- Hydrogen (H_2) dilution ratio: H_2 dilution of SiH_4 greatly affects the properties of deposited a-Si:H film [49]. Proper H_2 dilution can improve film properties by passivating dangling bonds while high H_2 dilution may induce structure ordering.

2.4 a-Si:H solar cells

p-n junction structure commonly used in c-Si solar cells (based on minority carriers diffusion) does not work efficiently if made of a-Si:H. Photo-generated carriers would recombine

in doped a-Si:H layers before reaching the contacts because of the very short diffusion length. Therefore, typical a-Si:H solar cells are based on p-i-n junction structure. The device contains three layers: p-type a-Si:H layer, intrinsic a-Si:H layer, and n-type a-Si:H layer, which form p-i-n junction. Figure 2.6 shows energy band diagrams of solar cells for (a) p-n junction and (b) p-i-n junction [51], which E_g is bandgap energy, V_{bi} is built-in voltage, E_f is fermi energy.

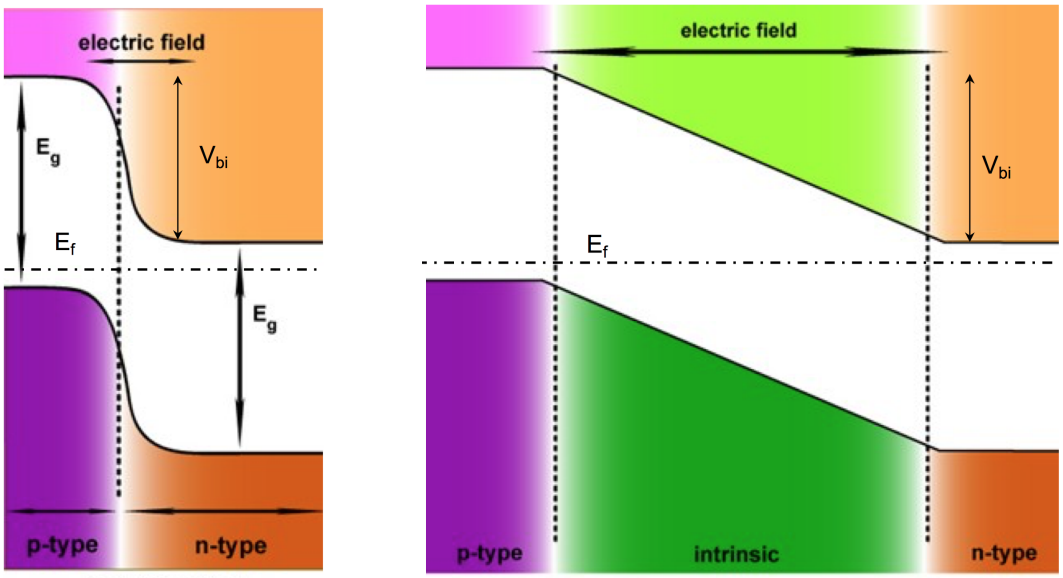

Figure 2.6: Energy band diagram of solar cells for (a) p-n junction and (b) p-i-n junction [51], which E_g is bandgap energy, V_{bi} is built-in voltage, E_f is fermi energy.

Doped layers have two functions in an a-Si:H solar cell. First, they establish an internal electric field across the intrinsic a-Si:H layer. The electric field should be high enough to ensure collection of photo-generated carriers in the intrinsic a-Si:H layer. The electric field is determined by the doping level of doped layers and the thickness of the intrinsic layer. Second, the doped layers form ohmic contacts between a-Si:H p-i-n stack and the

external electrodes. The photo-generated carriers drift towards the doped layers (electrons towards the n-type layer and holes towards the p-type layer) and then are collected by the electrodes.

2.4.1 I-V characteristics of solar cell

Figure 2.7 shows a typical illuminated I-V characteristic of a solar cell. Important points to note are open circuit voltage (V_{oc}), short circuit current (I_{sc}), and the coordinates of the maximum power output point maximum voltage (V_{mp}) and maximum current (I_{mp}).

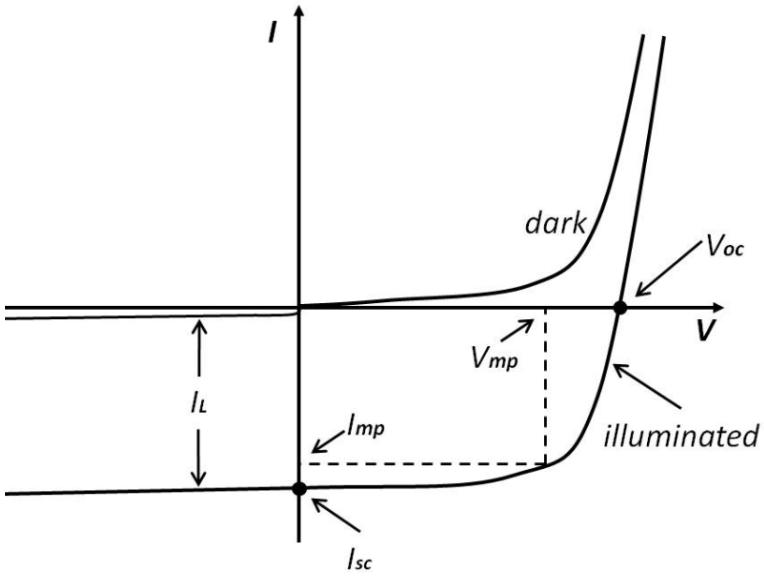

Figure 2.7: A typical illuminated I-V characteristic of a solar cell.

The FF is the ratio of the power that a cell would supply if it is ideal ($P=V_{oc}I_{sc}$), compared to the real maximum output power ($P_{out}=V_{mp}I_{mp}$). The FF defines the "squareness" of the I-V characteristics. The equation for the FF is given by:

$$FF = \frac{V_{mp} I_{mp}}{V_{oc} I_{sc}} \tag{2.4}$$

Here: V_{mp} is the maximum power voltage, I_{mp} is the maximum power current, V_{oc} is the open circuit voltage, and I_{sc} is the short circuit current.

The most common parameter used to evaluate the performance of a solar cell is the energy conversion efficiency. η is defined as the ratio of energy output from the solar cell to input energy from the sun (equation 2.5). In addition to reflecting the performance of the solar cell itself, η depends on the spectrum and intensity of the incident sunlight (AM1.5 standard test spectrum).

$$\eta = 100 \times (\frac{P_{out}}{P_{in}}) = 100 \times (\frac{V_{oc} I_{sc} FF}{A_c E}) \tag{2.5}$$

Here: A_c is the area of the cell and E is the test irradiance.

2.4.2 Ideal solar cell model

The ideal solar cell operation can be described by the equivalent circuit shown in Figure 2.8. It consists of an ideal diode in parallel with a photo-generated current source. The current generated by the current source flows in the opposite direction to the diode forward current. The model also includes shunt resistance (R_{sh}) and series resistance (R_s) represents current loss by recombination inside the diode and would be infinitely large in an ideal device. R_s is the internal series resistance and is heavily influenced by the resistivity and thickness of a-Si:H layer and the interfaces between them.

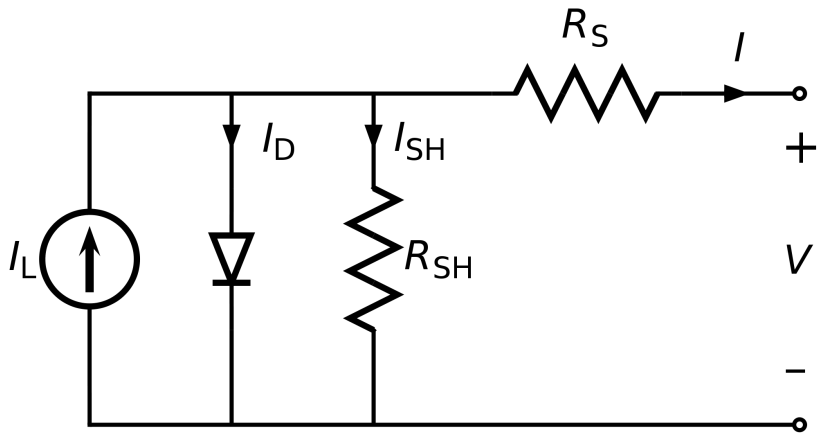

Figure 2.8: Equivalent circuit of an ideal solar cell model.

The expressions for a solar cell in the presence of R_s (equation (2.6)) and R_{sh} (equation (2.7)) are:

$$I = I_L - I_0 exp[\frac{q(V + IR_s)}{nkT}] \tag{2.6}$$

$$I = I_L - I_0 exp[\frac{qV}{nkT}] - \frac{V}{R_{sh}} \tag{2.7}$$

Here: I is the cell output current, I_L is the light generated current, V is the voltage across the cell terminals, T is the temperature, q and k are the electron charge and the Boltzmann constant, and n is the ideality factor.

Figure 2.9 shows schematic representation of the effect of (a) series resistance (R_s) and (b) shunt resistance (R_{sh}) on the solar cell I-V characteristic. R_s does not affect the V_{oc} of the solar cell because the overall current flow through the solar cell, and therefore through the R_s is zero. However, the I-V characteristic is strongly affected by R_s near the V_{oc} (Figure 2.9(a)) [52]. In addition, large R_s will limit I_{sc} as well. Low R_{sh} causes significant power losses in solar cells by providing an alternate current path for the photo-generated

current. Such a diversion reduces the amount of current flowing through the solar cell junction and reduces the V_{oc} from the solar cell (Figure 2.9(b)).

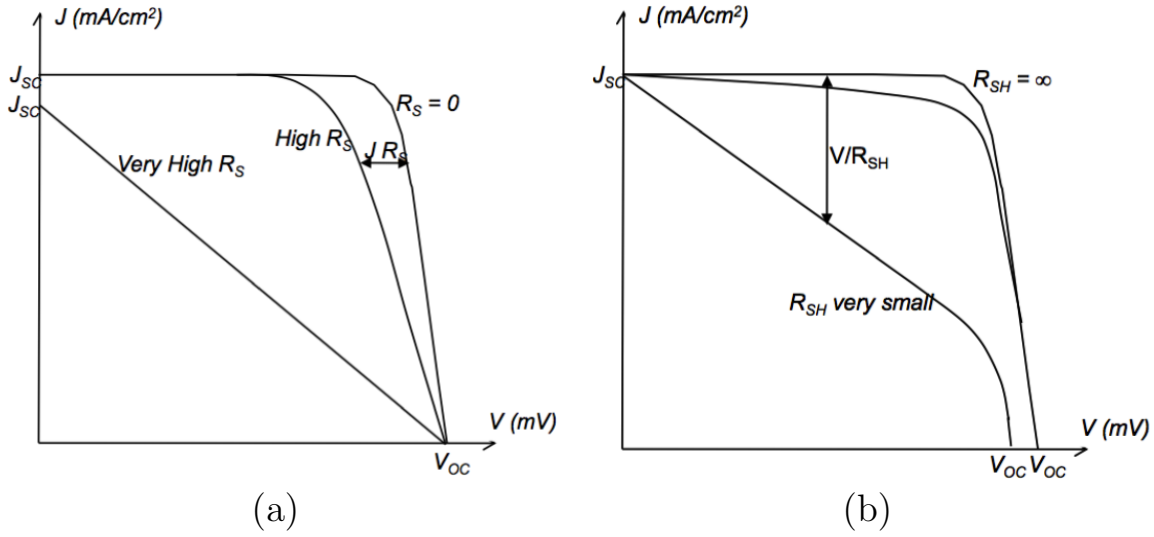

Figure 2.9: Schematic representation of the effect of (a) series resistance (R_s) and (b) shunt resistance (R_{sh}) on the solar cell I-V characteristics [53].

2.4.3 AM1.5 standard test spectrum

Two standard solar spectrums (AM1.5 Global and AM1.5 Direct spectrum) are defined as a standard radiation source to compare performance of solar cells designed for terrestrial use. The standard test spectrum for photovoltaics is AM1.5 Global (Air Mass 1.5) spectrum. It is defined for the range of 200∼5000 nm in units of $Wm^{-2}nm^{-1}$ for a 37° sun facing tilted surface. The total irradiance of AM1.5 Global spectrum is normalized to 100 mW/cm^2 and the power density of any part of the spectrum can be obtained by integrating between the relevant wavelengths. The AM1.5 Direct spectrum is defined for solar concentrator applications. It includes the direct beam from the sun and the circumsolar component in

a disk 2.5° around the sun. The AM1.5 Direct spectrum has an integrated power density of 90 mW/cm^2.

Figure 2.10 shows AM1.5 standard test spectrum in the range 200∼2500 nm published by National Renewable Energy Laboratory (NREL). It can be seen that the maximum of the spectrum is located between 500∼600 nm which matches absorption maximum of a-Si:H.

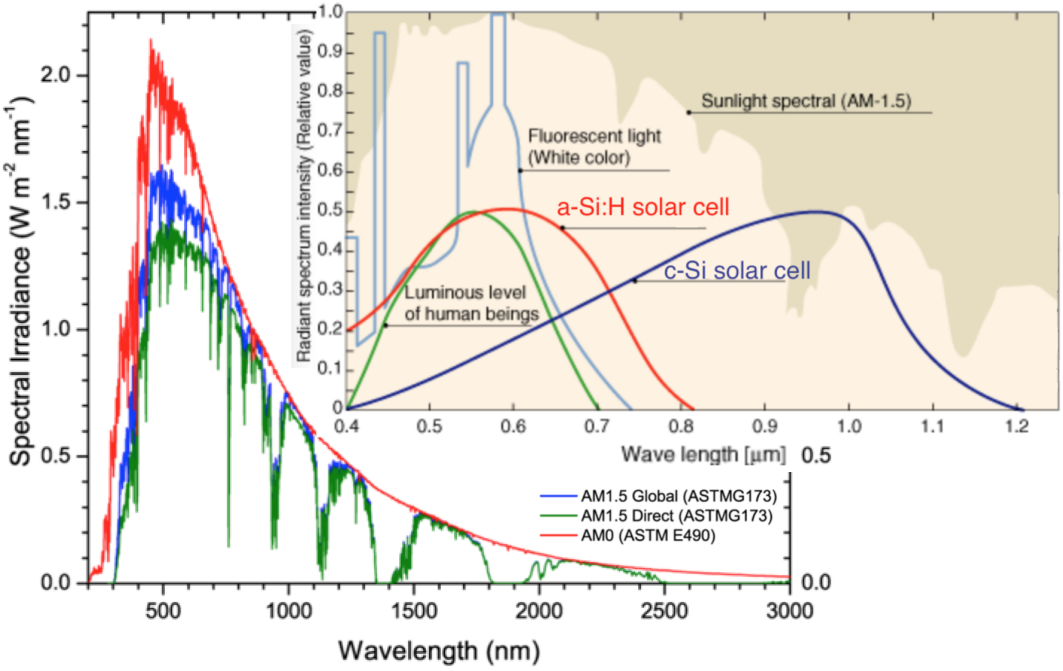

Figure 2.10: AM1.5 standard test spectrum. Inset displays the absorption spectrum of a-Si:H solar cells [54].

2.4.4 a-Si:H solar cell configurations

There are two basic configurations of a-Si:H solar cells, namely n-i-p/substrate configuration and p-i-n/superstrate configuration, which are defined as the sequence of Si thin film

layer deposition on transparent substrate. Figure 2.11 shows schematic representation of (a) substrate configuration and (b) superstrate configuration of a-Si:H solar cell. In the n-i-p solar cells, the n-type layer is deposited first, then the intrinsic layer and the p-type layer is deposited last. In the p-i-n solar cells, the sequence of the deposition is inverted.

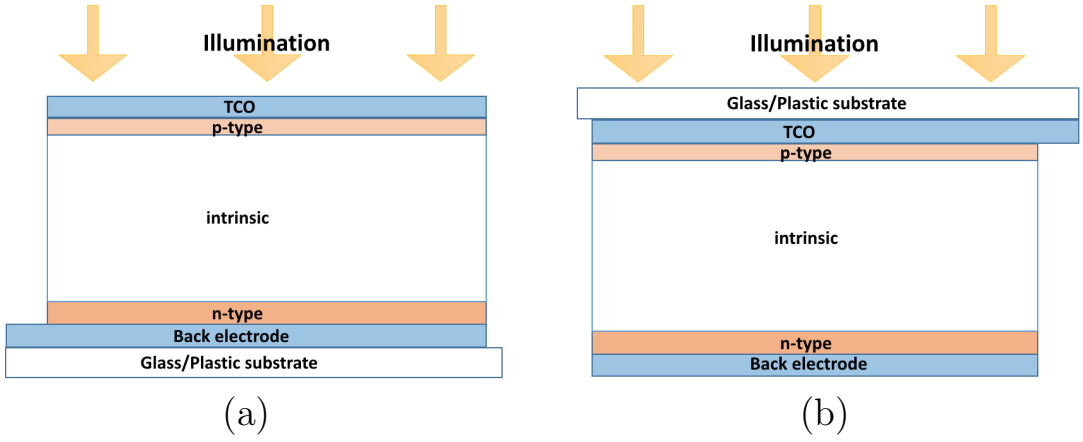

Figure 2.11: Schematic representation of (a) substrate configuration and (b) superstrate configuration of a-Si:H solar cell.

In the substrate configuration (n-i-p structure), the substrate forms the back side of the cell. This allows the use of opaque substrates such as stainless steel. Alternatively the polymer foils may be used as substrates, and can be thin enough to be flexible. A highly reflecting back electrode that contains metal layer such as Ag or Al is deposited onto the substrate. After depositing n-i-p a-Si:H stack, TCO thin film with a metal grid is formed as the front electrode. The improvement is required on the back contact texturing and reflectivity.

In the superstrate configuration (p-i-n structure), the p-i-n deposition sequence requires transparent substrates such as glass and plastic. Usually TCO-coated glass substrate is used. The TCO layer acts as the front electrode as well. The surface textured TCO layer

is used to improve light absorption inside the solar cell due to light scattering at internal rough interfaces. The p-i-n a-Si:H stack is then deposited on top of TCO layer. The back electrode is a metal layer with TCO interlayer. The TCO interlayer is used to improve the reflection from the back electrode by matching the refractive index between the n-type a-Si:H layer and metal layer.

2.5 PV modules

A PV module consists of many solar cells connected in parallel/series to increase the current/produce higher voltage. 36-cells module is the industry standard for high power production. Figure 2.12 shows typical module has 36-cells connected in series [52].

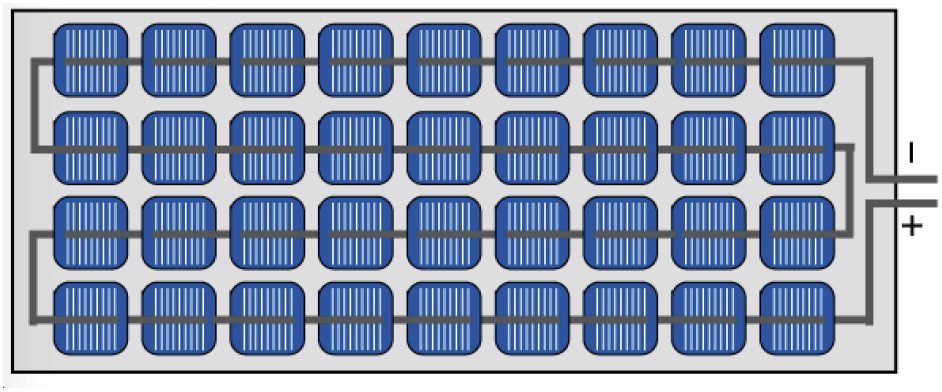

Figure 2.12: Typical module has 36-cells connected in series [52].

There are currently four commercial production technologies for PV Modules [55]:

- c-Si: This is the oldest and more expensive production technique, but it is also the most efficient energy conversion technology available. The average module efficiency is about 10∼12 %.

- poly-Si: This has slightly lower efficiency compared to c-Si but manufacturing costs are also lower. The average module efficiency is about 10∼11 %.
- String ribbon: This is a refinement of poly-Si production, there is less efficiency and costs are even lower. The average module efficiency is about 7∼8 %.
- a-Si or thin film: Silicon material is deposited on glass or other low cost substrates. The cost is lower than any other method. The average module efficiency is about 5∼7 %.

2.5.1 PV module performance

While the voltage from PV module is determined by the number of solar cells connected in series, the current from the module is primarily dependent on the size of solar cells and also on their energy conversion efficiency. The current from a module is not affected by the temperature in the same way as the voltage but is heavily dependent on the tilt angle of the module.

If all the solar cells in a module have identical electrical characteristics, and they are all under the same insolation and temperature, then all the solar cells will yield the same voltage and current. In this case, the I-V curve of the PV module has the same shape as that of the sub-cells.

2.6 Chapter summary

In this chapter, we reviewed atomic structure, electrical and optical properties, and doping mechanism in a-Si:H thin films. Deposition system and its parameters for a-Si:H are

discussed. The a-Si:H solar cell configurations, I-V characteristics under standard test spectrum, and the ideal solar cell model are also described. We also compare c-Si solar cell and a-Si:H solar cell.

Chapter 3

Characterization of Thin films and Hydrogenated Amorphous Silicon Solar Cells

In this chapter, we present characterization of thin films and solar cells. Section 3.1 describes the solar cell structures used in this thesis. Plastic substrate properties are summarized in section 3.2. Section 3.3 discusses the growth rate, micro-structural measurements, transmittance/reflectance measurements, and electrical conductivity measurements of a-Si:H thin films. Characterization of aluminum doped zinc oxide (AZO) thin films is also discussed in section 3.4. Section 3.5 discusses characterization for a-Si:H solar cells including I-V measurements and EQE measurements. PV module fabrication process on plastic substrate and contacts resistance simulation are investigated in section 3.6. At last, sample labeling scheme is described in section 3.7.

3.1 Solar cell characterized

The n-i-p solar cells were fabricated on glass and plastic substrates, and were also used in PV modules on plastic substrate. The substrate was at the back side of the cell. Highly reflecting back electrode (Al) was deposited on the substrate first. After depositing n-i-p a-Si:H stack, AZO thin film with metal grid was deposited as the front electrode.

The p-i-n solar cells were fabricated on glass substrate, and the same structure was used to fabricate semi-transparent solar cells on both glass and plastic substrates. The substrate was at the front side of the cell, and a AZO thin film was deposited over the substrate. After depositing p-i-n a-Si:H stack, Al or AZO thin film was deposited and patterned to form the back electrodes.

3.2 Flexible plastic substrates

3.2.1 Substrate properties

Rigid glass substrate is normally used for a-Si:H solar cells and modules. In our experiments, plastic substrate was also used as an alternative substrate because of its lightweight, flexibility, and low-cost. The widely-used commercial plastics are polyethylene-terephthalate (PET) and polyamide (PI). They both have high strength and toughness, good heat resistance, good chemical resistance, and excellent dimensional stability [56]. Some plastics are able to maintain electrical and mechanical properties over a wide temperature range at 105$\sim$285 °C (Table 3.1).

Table 3.1: Properties of various high performance films [56].

Property	Unit	PEN	PET	PI
Glass transition temperature	°C	155	110	-
Melting point	°C	269	258	360∼410

In this study, 100 μm thickness of Teonex® PEN plastic was chosen for solar cell fabrication. (Teonex® is the trade name of polymer film manufactured by DuPont©). This product has been developed specifically to meet the needs for optically transparent films with performance between that of PET and PI. The key features of PEN plastic include [57]:

- Low thermal shrinkage (0.6 % compared to 1.3 % of PET)
- Excellent dielectric strength (25 % greater than PET)
- High melting point (269 °C compared to 258 °C of PET)

3.2.2 Substrate characterization

Atomic force microscopy (AFM) was used to examine the surface morphology of plastic substrate. In the process of flexible cell fabrication, the surface roughness of deposited metallic back contacts could only be investigated using an optical microscope prior to deposition. While AFM image gave some insight to back contact suitability, there was no substitute for more advanced technique.

100 nm thick Al electrode was deposited onto PEN in sputtering system at room temperature. 4×4 μm^2 area of PEN coated with Al was investigated using AFM scan as shown in Figure 3.1. The root mean square (RMS) surface roughness was measured to be 14.96 nm which is comparable with that of the bare PEN surface roughness. Thus,

we assume that metal layer deposited on top of bare PEN uniformly covers PEN surface, which eventually enables a-Si:H deposition.

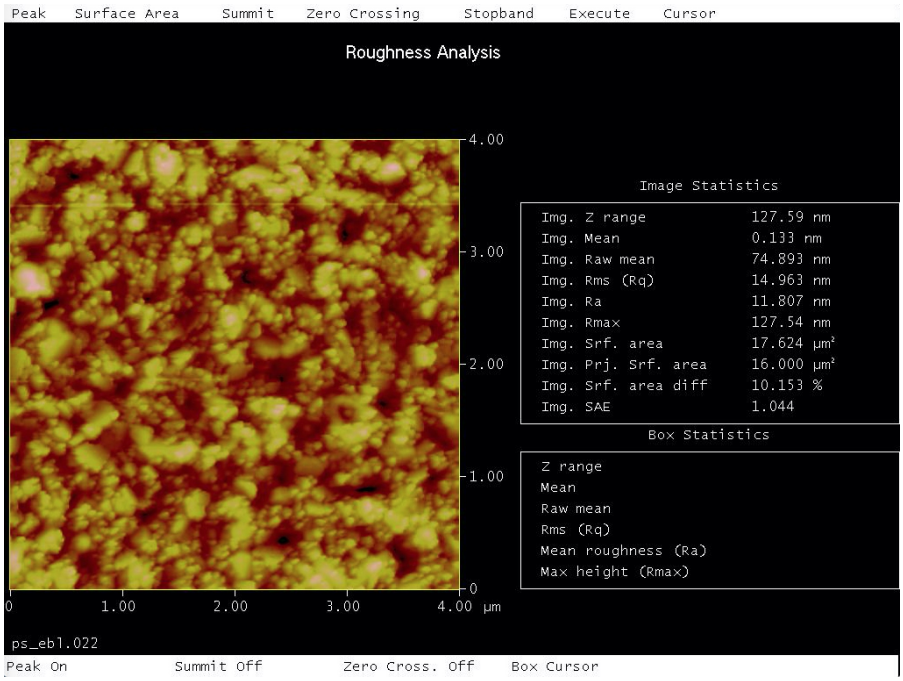

Figure 3.1: The AFM surface morphology image of a 16 μm^2 area of PEN coated with Al.

Small surface roughness is necessary to ensure the formation of a closed film during a-Si:H deposition. As a rule of thumb, the maximum roughness should be less than one third of the seed film thickness [40]. In addition, for 350 nm thick a-Si:H stack, 14.96 nm substrate surface roughness transforms to $\sim$5 % thickness non-uniformity.

3.3 Intrinsic and doped a-Si:H characterization

3.3.1 Growth rate and structure characterization

Dektak-8 stylus profilometer was used for film thickness measurements. Figure 3.2 shows (a) photograph of a-Si:H films of different thickness and (b) film thickness as a function of deposition time for a-Si:H films. Here, a-Si:H films were deposited at $[H_2]/[SiH_4]$=5, deposition pressure of 900 mTorr, RF power of 2 W, and deposition temperature of 150 °C using RF PECVD system [40].

The color change with film thickness indicates that our a-Si:H films can be used for semi-transparent solar cell fabrication with different transmittance for some functional applications (Figure 3.2(a)). It is seen from Figure 3.2(b) that the film growth is almost linear with deposition time, and the growth rate of tested a-Si:H films was calculated to be around 0.1 nm/sec from the fitting of Figure 3.2(b). The growth rate of the a-Si:H films was limited due to hydrogen dilution of SiH_4 ($[H_2]/[SiH_4]$=5), which is essential to yield required electronic properties in the case of low-temperature deposition (∼150 °C) [44]. Fourier transform infrared spectroscopy (FTIR) measurements of a-Si:H films grown with hydrogen dilution and without hydrogen dilution are shown in Figure 3.3. It is seen that the ratio of absorption intensities at 2000 cm^{-1} over 2100 cm^{-1}, which corresponds to Si-H and Si-H_2 bonds and correlates with electronic properties [58], in a-Si:H deposited from hydrogen-diluted SiH_4 is higher than that of 100 % SiH_4 deposited a-Si:H [44]. Here, Si-H is indicative to typical Si-H bonds, while Si-H_2 is indicative to defective Si-H bonding [58]. The result implies that hydrogen dilution could remove/suppress Si-H_2 bonds in a-Si:H network.

Figure 3.4 shows Raman spectra of a-Si:H film ($[H_2]/[SiH_4]$=5) and of nc-Si:H film

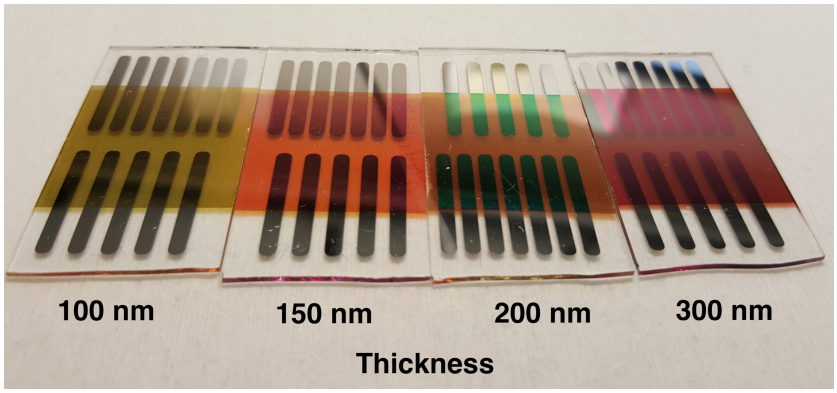

(a)

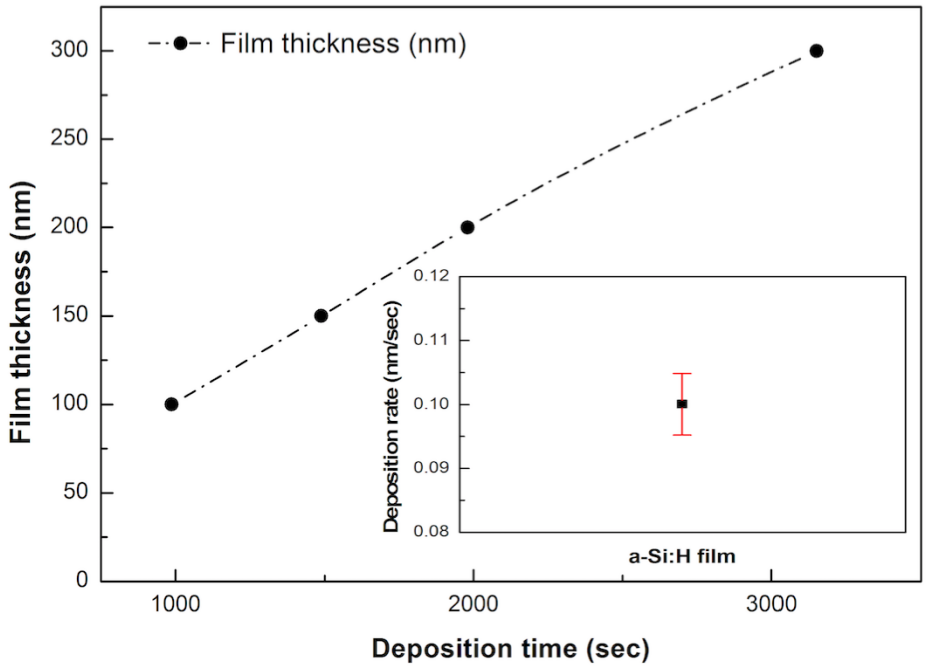

(b)

Figure 3.2: (a) Photograph of a-Si:H films of different thickness and (b) film thickness as a function of deposition time for a-Si:H films. Inset of Figure 3.2(b) displays the measurement error of growth rate of a-Si:H films.

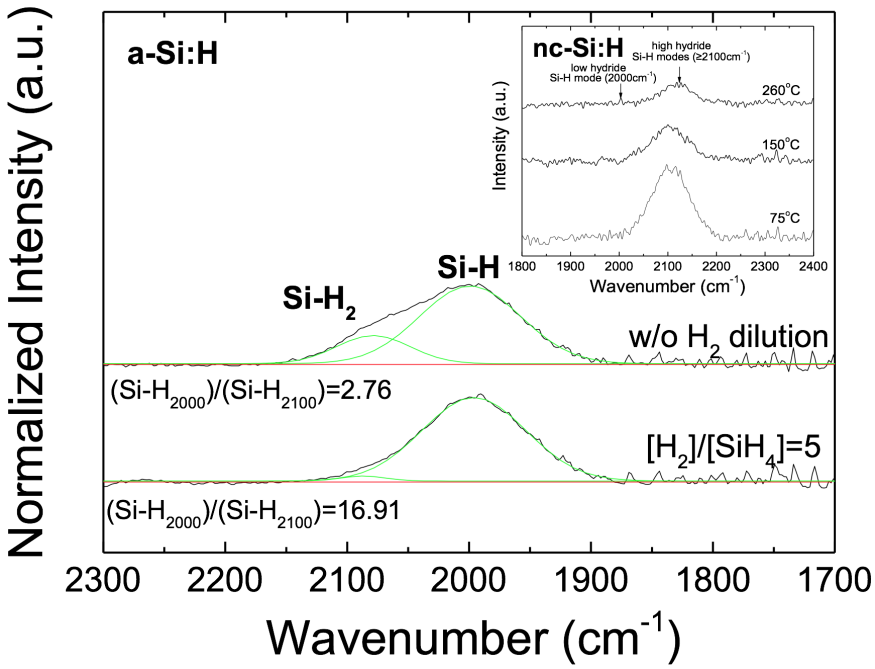

Figure 3.3: FTIR spectra of Si thin films deposited with hydrogen dilution. Inset of Figure 3.3 displays Si-H bonds configuration from nc-Si films for different deposition temperatures [59].

($[H_2]/[SiH_4]$=50) for comparison. The Raman Spectra were measured with 632 nm laser source excitation using Renishaw Micro-Raman 1000 spectrometer. The He-Ne laser source was preferred over 504 nm wavelength Ar laser source because of its longer penetration depth ($\sim$1 μm) than that of Ar laser source ($\sim$50 nm) [60]. The laser intensity on the film surface was controlled to be at a 10 % of maximum intensity (approximately 0.27 mW) to prevent crystallization of a-Si:H film during the measurements. For a-Si:H film, only broad peak at $\sim$480 cm^{-1} is observed, indicating the presence of amorphous phase only. This result also suggests that hydrogen dilution ($[H_2]/[SiH_4]$=5) does not change film structure. At high hydrogen dilution ($[H_2]/[SiH_4]$=50), sharp peak wass observed at $\sim$520 cm^{-1} indicating presence of nano crystallites in the film along with broad peak at $\sim$480 cm^{-1},

which means the growth of two-phase material. The film crystallinity $X=I_{520}/(I_{520}+I_{480})$ where I_{520} is the intensity of ~520 cm^{-1} peak corresponding to crystalline phase and I_{480} is the intensity of ~480 cm^{-1} peak corresponding to amorphous phase, was measured to be 53 %. The presence of nanocrystals in nc-Si thin film was also confirmed by FTIR measurements (Figure 3.3 inset) showing predominant Si-H_2 bonding absorption peak at 2100 cm^{-1}, which indicates presence of Si-H bonds located at nanocrystal surfaces [59].

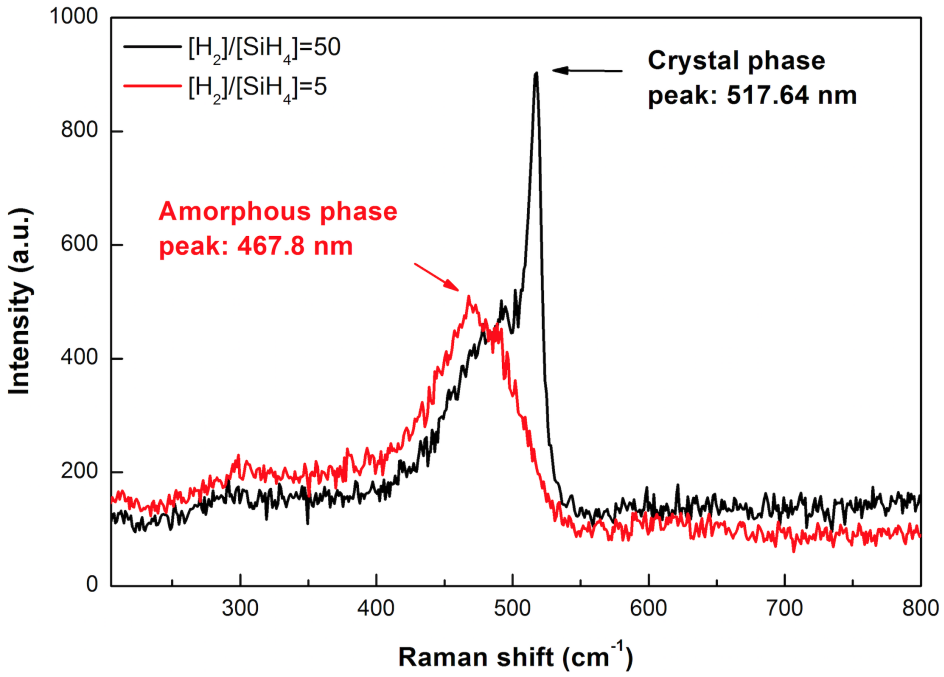

Figure 3.4: Raman spectra of a-Si:H and nc-Si:H films deposited at different hydrogen dilution.

3.3.2 Transmittance/Reflectance measurement

For E_g measurements, we used an ultraviolet-visible light (UV-Vis) spectrometer by Shimadzu (UV-2501PC) with a double-blazed, double-monochromator system. The wave-

length range is 190∼1100 nm, resolution is 0.1 nm, and accuracy is ±0.3 nm. The relationship between α and E_g is discussed in section 2.2.3. α was obtained from the transmittance (T) and reflectance (R) measurements of a-Si:H with known film thickness (d) using approximated equation:

$$T \approx (1-R)^2 e^{-\alpha d} \Leftrightarrow \alpha = -\frac{1}{d} ln\left(\frac{T}{(1-R)^2}\right) \tag{3.1}$$

Figure 3.5 shows (a) transmittance/reflectance and (b) E_g calculation for intrinsic a-Si:H film. Transmittance/reflectance measurements and E_g calculation for p-type a-SiC:H film is also shown in Figure 3.6(a) and Figure 3.6(b), respectively. In order to calculate E_g, $\sqrt{\alpha E_g}$ was plotted vs. photon energy using UV-Vis transmittance/reflectance measurements (Figure 3.5(a) and Figure 3.6(a)) according to equation (3.1). E_g was found to be 1.72 eV and 1.98 eV for intrinsic a-Si:H in Figure 3.5(b) and for p-type a-SiC:H in Figure 3.6(b), respectively. These values are chose to those of device-grade a-Si:H films published in the literature by other researchers [42].

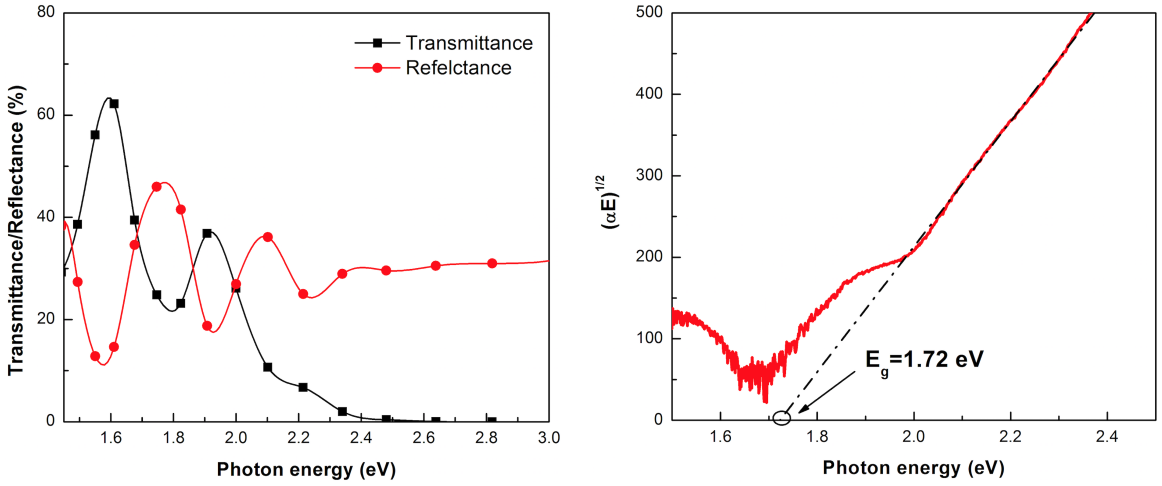

Figure 3.5: (a) Transmittance/reflectance and (b) E_g calculation for intrinsic a-Si:H film.

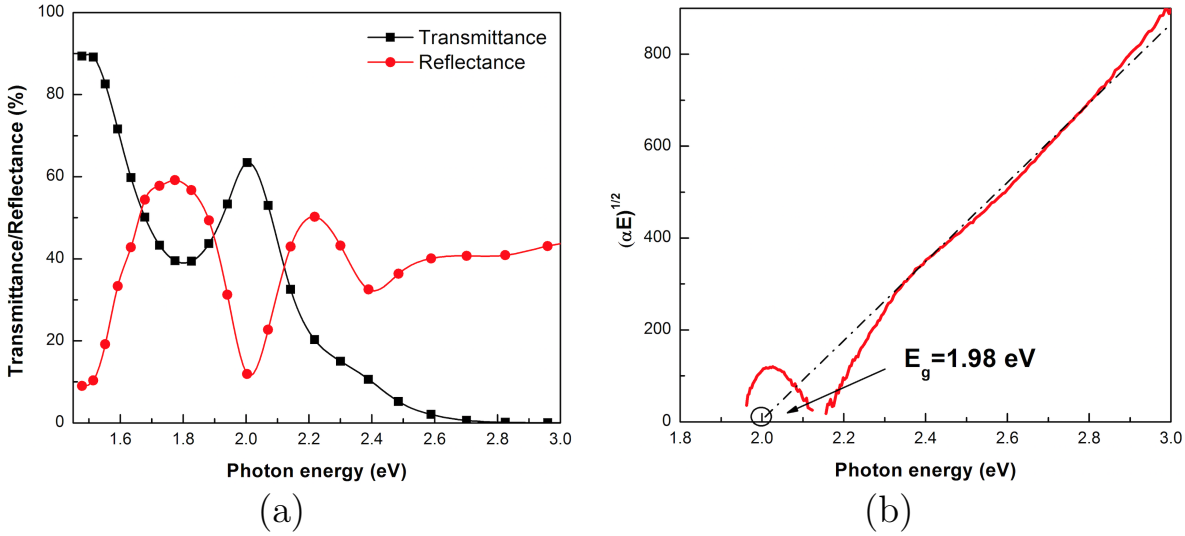

Figure 3.6: (a) Transmittance/reflectance and (b) E_g calculation for p-type a-SiC:H film.

3.3.3 Electrical conductivity measurement

The electrical characteristics of a-Si:H films were evaluated using electrical dark- and photo-conductivity (σ_{dark} and σ_{photo}). Keithley 4200-SCS semiconductor characterization system was used for σ_{dark} measurement. σ_{photo} was measured under illumination using AM1.5 spectrum with incident power of 100 mW/cm^2 (which is close to irradiance of the AM1.5 Global spectrum) using solar simulator (ABET technologies, SUN-2000).

Figure 3.7 shows (a) schematic representation of samples with co-planar electrodes geometry for conductivity measurement and (b) photograph of 300 nm thick a-Si:H film deposited on co-planar 100 nm thick Al electrodes on glass substrate.

The conductivity was calculated by equation (3.2):

$$\sigma = \left(\frac{I}{V}\right)\left(\frac{L}{W}\right)\left(\frac{1}{t}\right) \tag{3.2}$$

Here: V is the voltage bias (80 V), I is measured current, W is the electrode width (1 cm), L is the electrode length (1 mm), and t is the film thickness.

Figure 3.8 shows (a) dark- and (b) photo-current as a function of applied voltage for 300 nm thick a-Si:H film. It is seen that the current is linearly increasing with applied voltage, which typical of an ohmic behavior. σ_{dark} and σ_{photo} were measured to be 5.47×10^{-10} $(\Omega\text{cm})^{-1}$ and 3.3×10^{-5} $(\Omega\text{cm})^{-1}$, respectively. Photoresponse ($\sigma_{photo}/\sigma_{dark}$) is 6×10^4, which is comparable to that of device-grade a-Si:H film reported elsewhere [61].

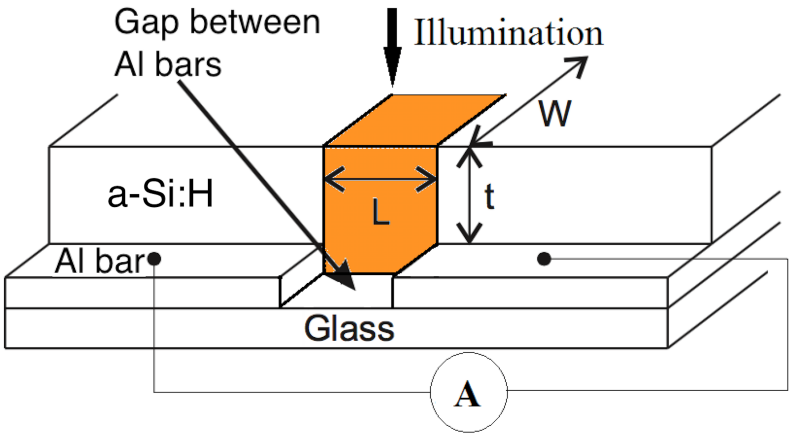

(a)

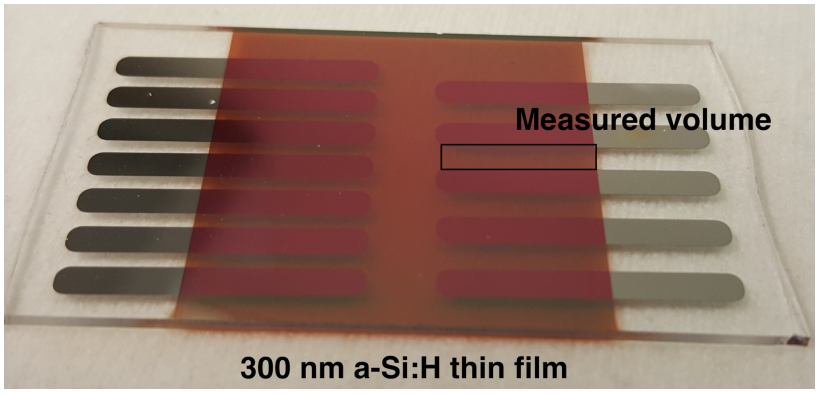

(b)

Figure 3.7: (a) Schematic representation of samples with co-planar electrodes geometry for conductivity measurement and (b) photograph of 300 nm thick a-Si:H film deposited on co-planar 100 nm thick Al electrodes on glass substrate.

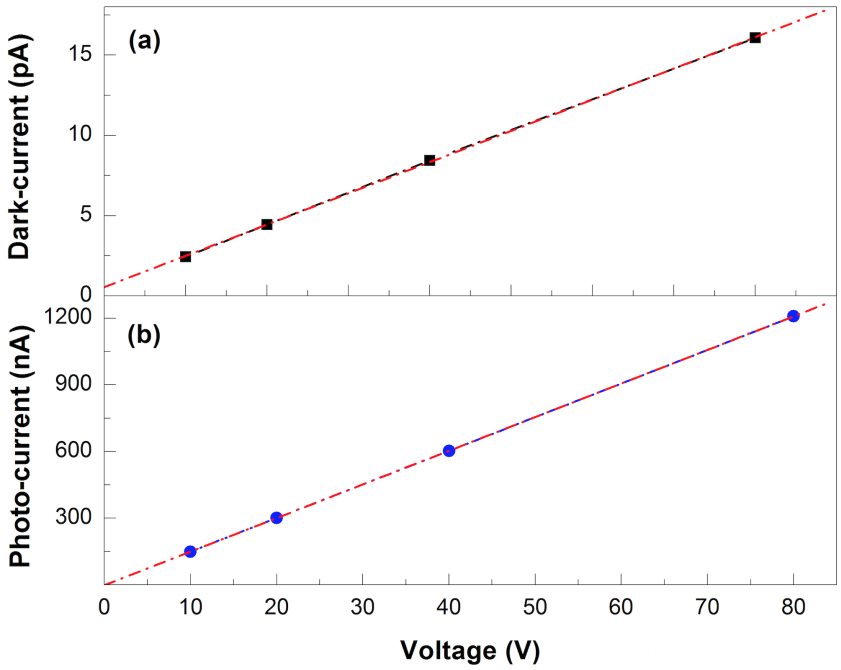

Figure 3.8: (a) Dark- and (b) photo-current as a function of applied voltage for the 300 nm a-Si:H film.

3.4 Characterization of AZO thin films

3.4.1 Deposition temperature effect on AZO thin films

In our study, sputter-deposited AZO was used as transparent front or back electrodes in a-Si:H solar cells. For solar cell application, the characteristics of AZO thin film are determined by trade-off between electrical and optical properties. AZO thin film properties depend on such deposition parameters as Ar gas flow rate, process pressure, substrate temperature, etc. In particular, electrical properties are mainly affected by the substrate temperature without significant degradation of optical properties [62]. Furthermore, the substrate temperature is limited when using plastic substrates by their melting point. Hence we studied effect of substrate temperature (50∼150 °C) on AZO optical and electrical properties.

Figure 3.9 shows (a) optical transmittance and (b) sheet resistance (R_{sh}) of 200 nm thick AZO thin films deposited at different substrate temperatures. The transmittance spectra were in the range of 300∼800 nm, which includes a main absorption range (400∼700 nm) of a-Si:H solar cells The deposition temperature does not affect the optical transmission; there is no significant difference in transmittance spectra for all the samples (Figure 3.9(a)). The average optical transmittance in the visible wavelength range is measured to be above 90 % for all AZO thin films deposited at different deposition temperatures. However, R_{sh} decreases from 220 Ω/□ to 155 Ω/□ when the substrate temperature increases from 50 °C to 150 °C (Figure 3.9(b)). This is attributed to improvement of crystalline structure and the increase of free electron concentration [63]. For our solar cells on plastic substrates, the substrate temperature of ∼150 °C was chosen.

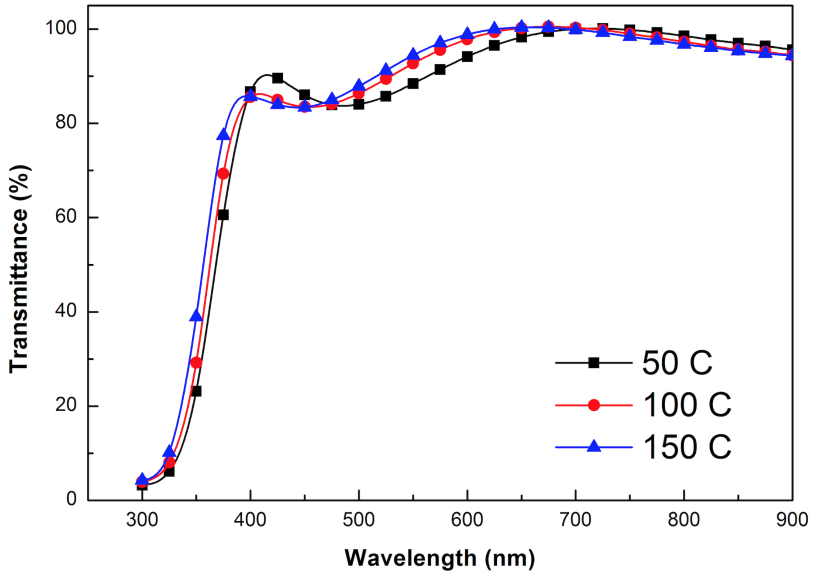

(a)

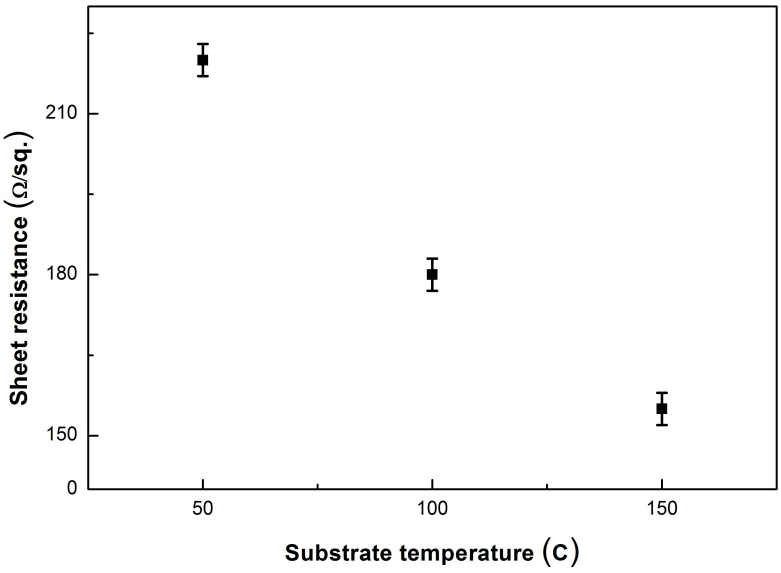

(b)

Figure 3.9: (a) Optical transmittance and (b) sheet resistance (R_{sh}) of 200 nm AZO thin films deposited at different substrate temperatures.

3.4.2 Film thickness effect on AZO thin films

Figure 3.10 shows (a) optical transmittance and (b) sheet resistance (R_{sh}) of AZO thin films of different film thickness deposited at a substrate temperature of 150 °C. As it can be seen from Figure 3.10(a) that increasing AZO film thickness adversely affects the transmittance in the visible wavelength range because of higher absorption of thicker film [64]. While thinner films show better transparency, the R_{sh} increases from 35 Ω/□ to 165 Ω/□ (Figure 3.10(b)). For our solar cell, we selected 200 nm thick AZO deposited at 150 °C, showing 155 Ω/□ corresponding to a dark-conductivity of 3×10^{-3} $(\Omega\text{cm})^{-1}$, indeed comparable to one of the resistivity of 1.17×10^{-3} $(\Omega\text{cm})^{-1}$ reported in the literature [65].

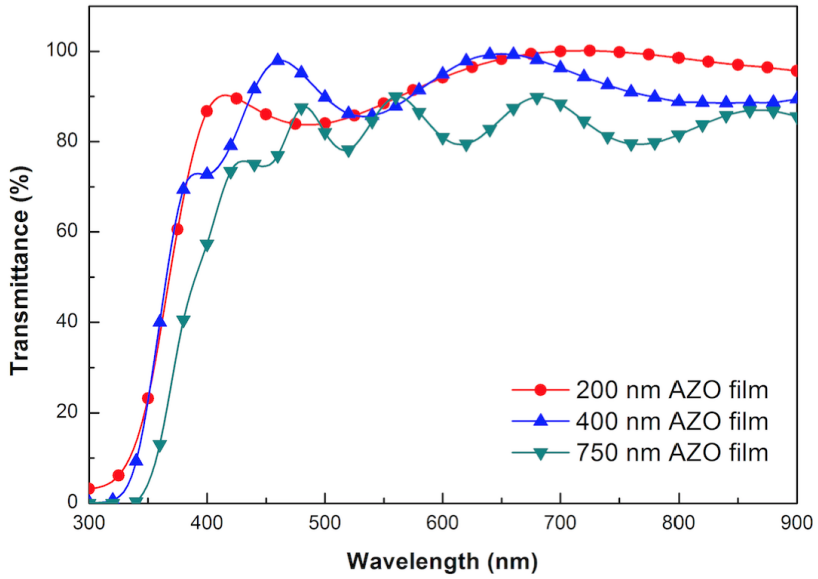

(a)

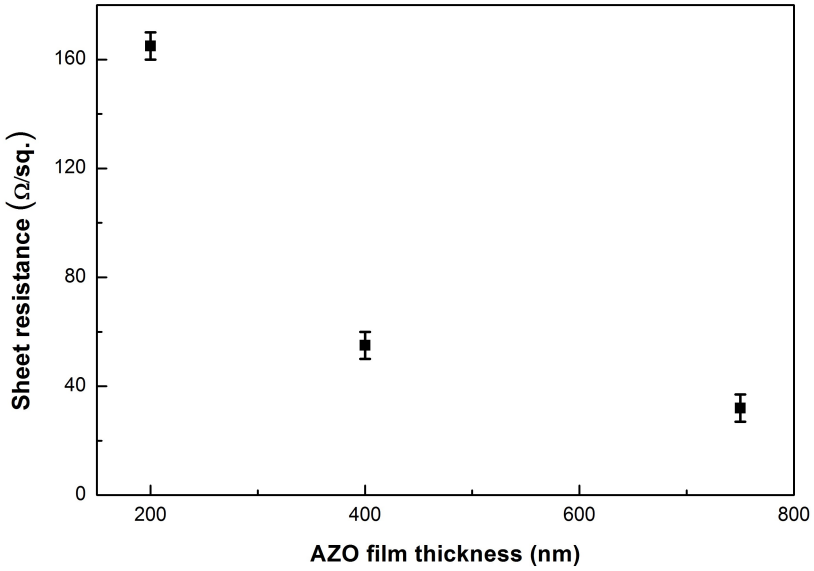

(b)

Figure 3.10: (a) Optical transmittance and (b) sheet resistance (R_{sh}) of different AZO thin film thickness deposited at substrate temperature of a 150 °C.

3.5 Solar cell characterization

Solar cells were characterized by I-V measurements carried out under illumination by Xe-Arc lamp monitored by using a c-Si reference cell calibrated by global AM1.5 spectrum. I-V characteristics were recorded by biasing devices with Keithley 2400 source meter. The current was recorded at each bias point using Tracer I-V measurement software. Figure 3.11 shows the solar simulator system, which provides white illumination needed in the measurement. Solar cell parameters (I_{sc}, V_{oc}, FF, R_{sh}, and R_s) as already mentioned in section 2.4.1 were automatically calculated by the software.

Figure 3.11: Photograph of solar simulator from ABET Technologies.

Figure 3.12 shows measurement setups for (a) a-Si:H n-i-p solar cell and (b) a-Si:H p-i-n solar cell. Note that the distance between the light source and the solar cell was kept the same for both measurements.

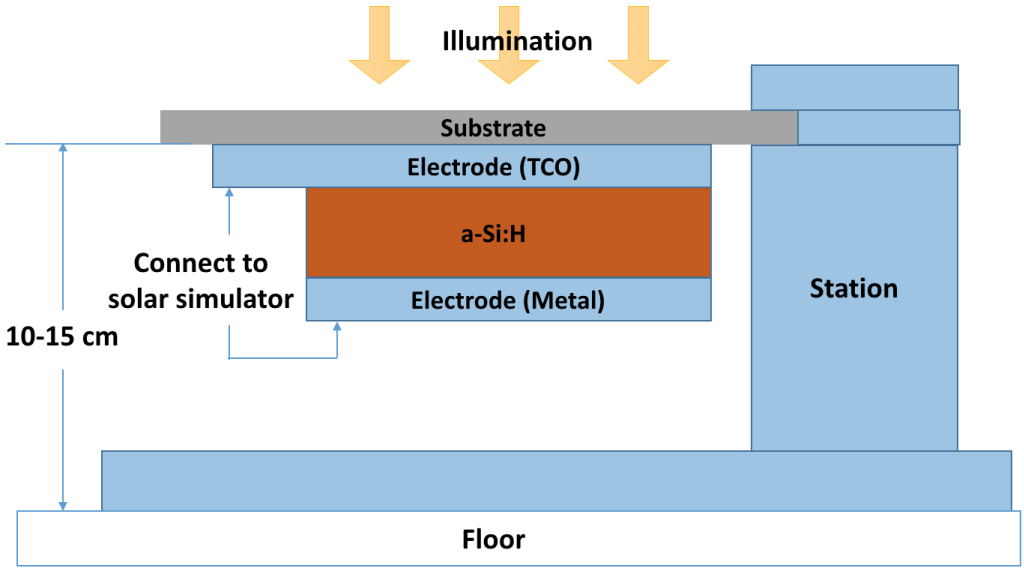

(a)

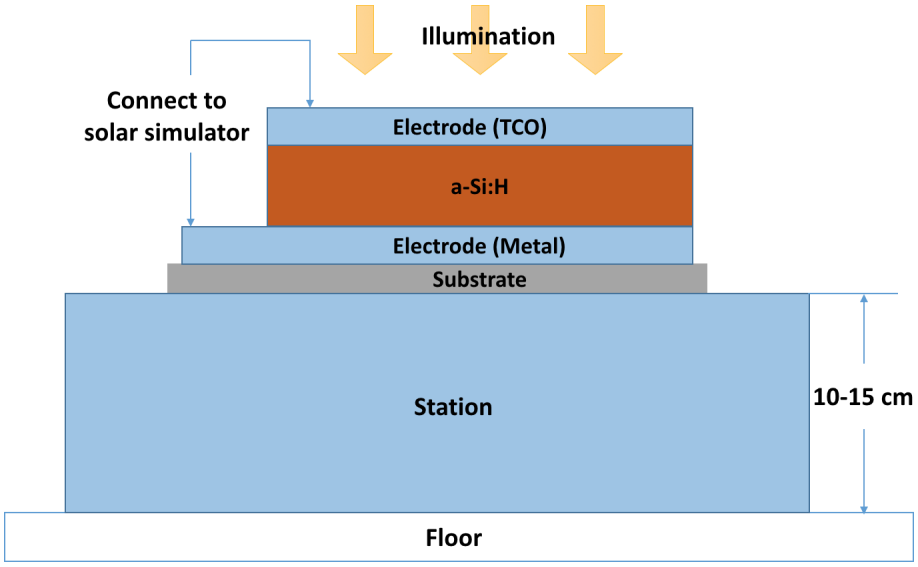

(b)

Figure 3.12: Measurement setup for (a) a-Si:H n-i-p solar cell and (b) a-Si:H p-i-n solar cell.

Two types of frame holders for p-i-n solar cells grown the plastic and glass substrates are shown in Figure 3.13.

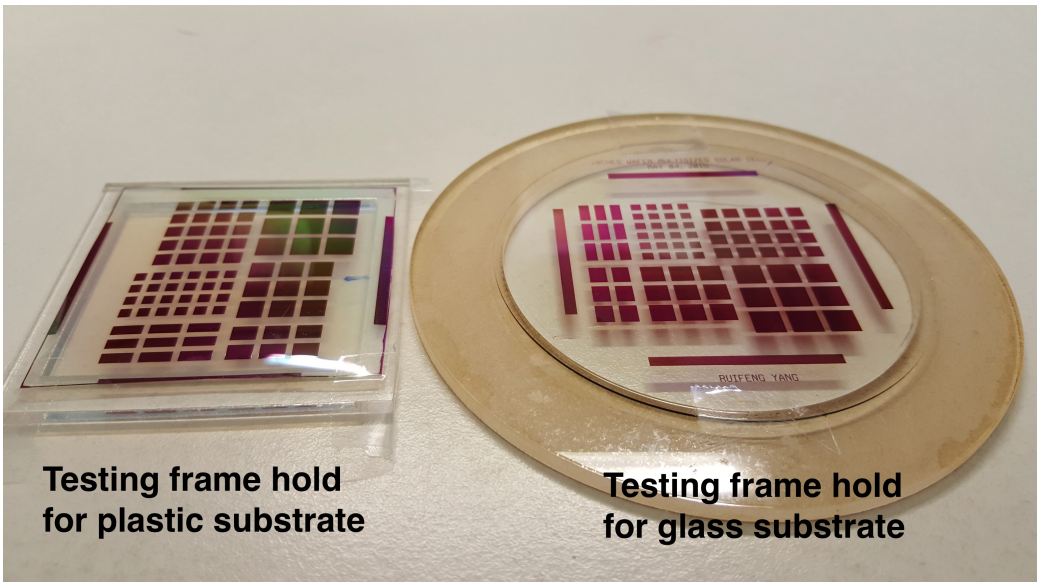

Figure 3.13: Two types of frame holders for different shapes of p-i-n solar cells samples.

Besides I-V characteristics of fabricated solar cells, EQE was measured. EQE is defined as the ratio of the number of charge carriers collected from the solar cell to the number of photons of given energy incident on the solar cell by equation (3.3):

$$EQE = \frac{electrons\ out}{photons\ in} = \frac{current/charge\ of\ one\ electron}{total\ power\ of\ photons/energy\ of\ one\ photon} \tag{3.3}$$

The measurements were performed under short-circuit conditions without background illumination and Figure 3.14 shows photograph of EQE measurement system components. The key point for measuring EQE is to provide the photo-current that a solar cell will produce when illuminated.

Figure 3.14: Photograph of EQE measurement system components.

3.6 PV modules fabricated on plastic substrates

3.6.1 PV module fabrication

The PV module was fabricate by using three-mask process as shown in Figure 3.15. The device fabrication started with plastic substrate cleaned in an isopropanol (IPA) bath for about 1 minute. After drying plastic substrates using N_2, 200 nm thick a-SiO_xN_y:H films on both surfaces, as the back encapsulation layer and front barrier-layer, using single-chamber PECVD system at a deposition temperature of 150 °C. Then, the substrate was attached to the carrier (Figure 3.15(a)) with shadow mask #1 (Figure 3.15(b)) followed by loading into the metal sputtering system. 200 nm Al/10 nm Cr layers were deposited using RF sputtering at room temperature. The a-Si:H n-i-p stack layer was then deposited using multi-chamber RF PECVD using developed deposition recipes in section 4.1. Typical thickness of a-Si:H solar cell layers were 15 nm for p-a-Si:H, 300 nm for i-a-Si:H, and 20 nm for n-a-Si:H. AZO front electrode was then deposited through a shadow mask #2 (Figure 3.15(c)) in the sputtering chamber. To perform via opening, the a-Si:H stack layer was selectively etched using dry etching process. After the dry etching process, 150 nm Al was

sputtered through shadow mask #3 (Figure 3.15(d)) to form the back metal deposition.

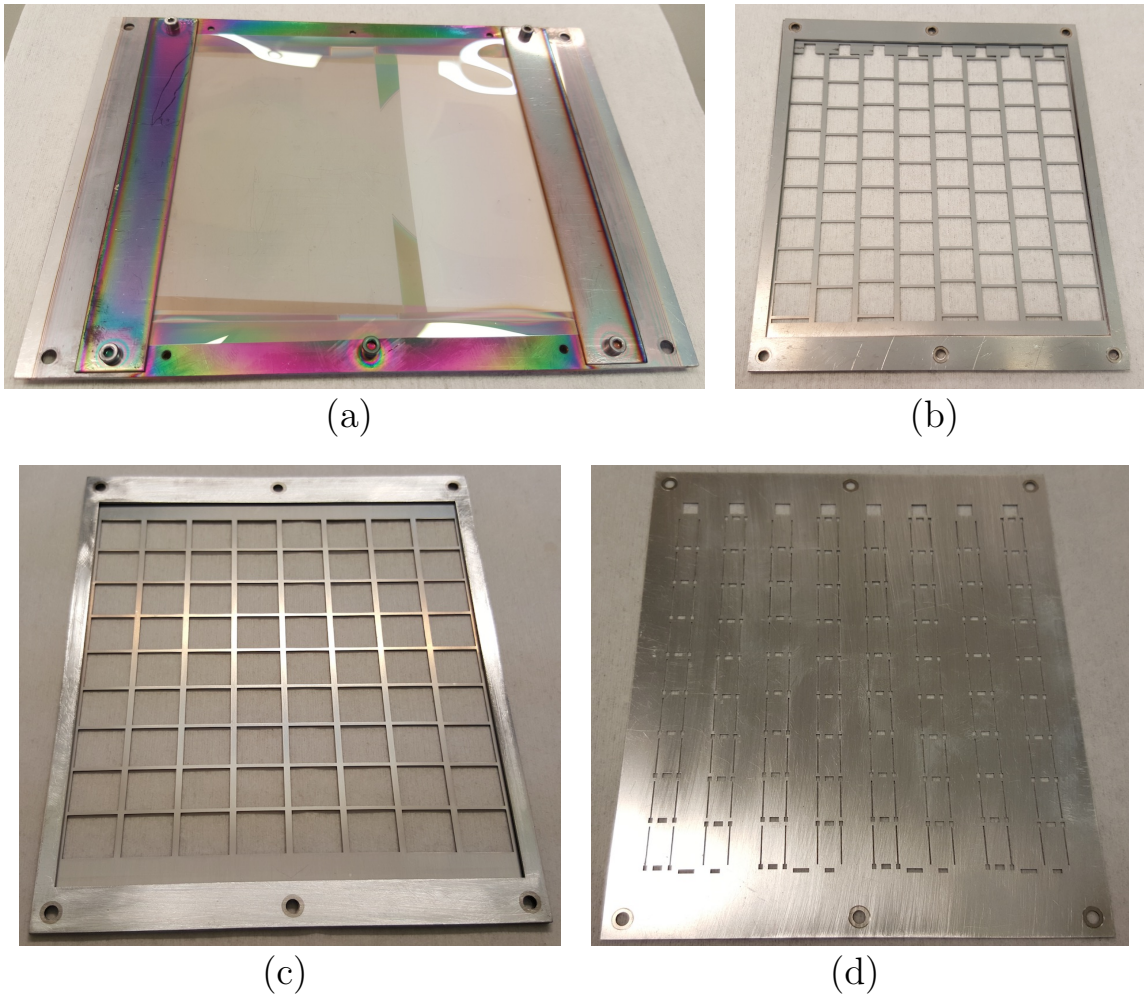

Figure 3.15: (a) Substrate carrier, (b) shadow mask #1 for back metal electrodes deposition, (c) shadow mask #2 for AZO thin-film deposition, and (d) shadow mask #3 for front metal electrodes deposition.

Figure 3.16 shows process flow diagram for a-Si:H n-i-p PV module on plastic substrate using shadow masks.

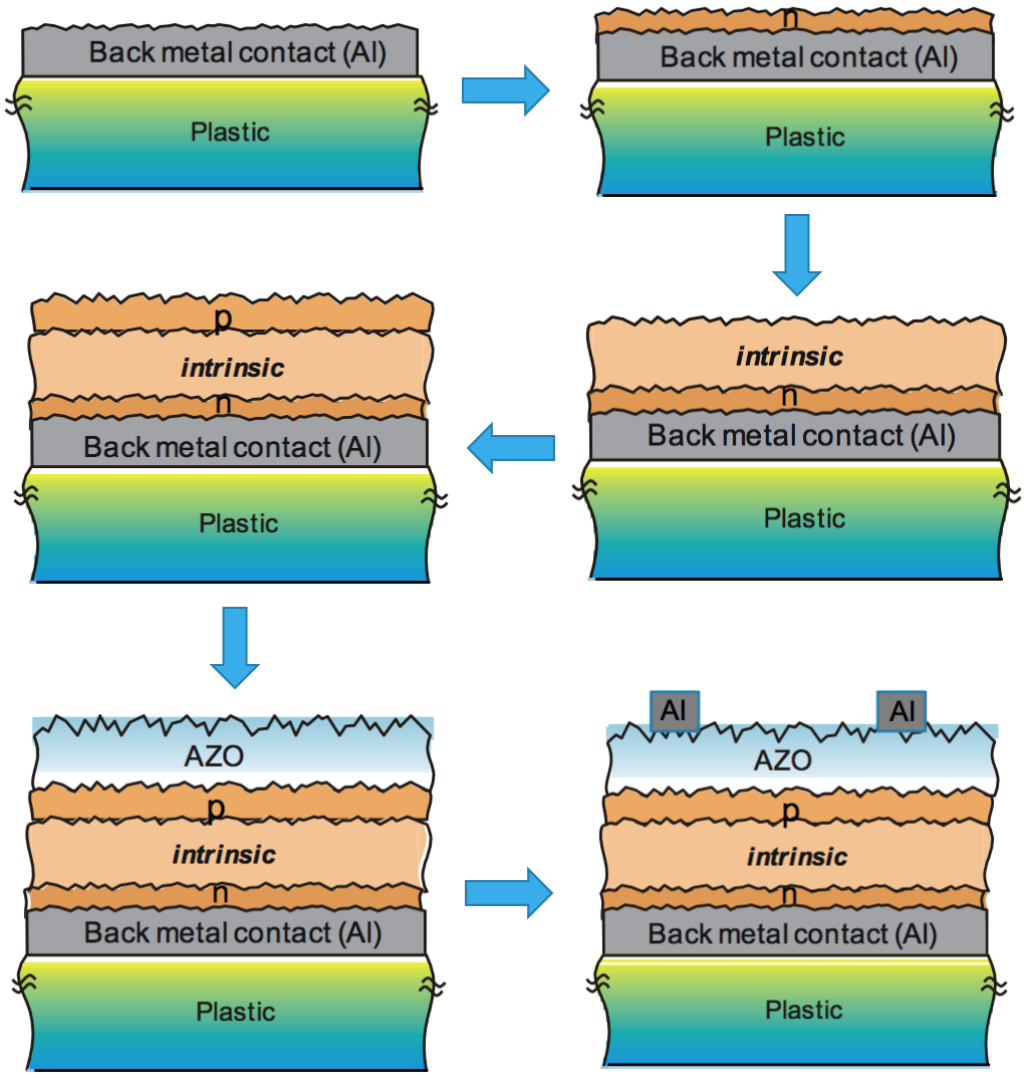

Figure 3.16: Process flow diagram for a-Si:H n-i-p PV module on plastic substrate using shadow masks.

3.6.2 Simulation of contact resistance

In a-Si:H PV modules, each cell is connected to other to effectively collect power in the module structure. For efficient PV module fabrication, besides solar cell layers, contact

layers such as AZO and Al should be optimized/engineered to suppress any power loss. Hence, before fabricating the PV modules, we carried out contact layers (AZO and Al) simulation for better module operation.

Two-dimensional simulation if sheet resistance was performed to characterize the device design. HSPICE simulator was used to perform calculations, then linked to MATLAB to form the input file, readout data from the output file, and visualize the results. Input parameters include the dimensions of the cell, R_{sh} of the AZO and top metal layers, net series resistance (R_p), parameters of the diode, and current source elements.

3.7 Sample labeling scheme

For better management with fabricated solar cells, tested cells are named as "substrate type (g: glass & p: plastic)-fabrication data-number of cell". For example, cell "g-150729-2" represents the second cell made on glass substrate on the 29th July, 2015.

3.8 Chapter summary

In this chapter, we summarize plastic substrate properties included AFM analysis to investigate the PEN surface morphology. The growth rate, micro-structural measurements, transmittance/reflectance measurements, and electrical conductivity measurements of a-Si:H thin films are discussed. Characterization of AZO thin films is also discussed, and then I-V characteristics measurement and EQE measurement is discussed to evaluate a-Si:H solar cells. We also discuss PV module fabrication on plastic substrate. At last, we describe the sample labeling scheme.

Chapter 4

Fabrication and Characterization of N-I-P Solar Cells

We presented the characterization of a-Si:H and AZO thin films in Chapter 3. In this chapter, results of fabrication and characterization of a-Si:H n-i-p solar cells on glass and plastic substrates are presented. In section 4.1, after a discussion about effect of p-a-Si:H thickness on solar cell performance, we show effect of incorporation of p-type a-SiC:H window layer on solar cells performance. Section 4.2 discusses the performance of PV modules fabricated on flexible plastic substrates. Simulation of contact resistance in PV modules was performed, and then J-V characteristics were measured to investigate the PV module performance.

4.1 N-i-p solar cells fabricated on glass substrate

4.1.1 Effect of p-layer thickness on solar cell performance

p-type a-Si:H layer (p-layer) thickness is critical for efficient a-Si:H solar cells. If the p-layer is too thick, I_{sc} will decrease due to a degradation of short wavelength absorption resulting from high absorption in highly defective p-layer. If the p-layer is too thin, V_{oc} will decrease due to degradation of built-in potential. If the p-layer is very thin, it may not be able to sustain electric field over the intrinsic region in which case collection of generated carriers will be impacted, resulting in lower R_{sh} and short circuit current density (J_{sc}). Hence, we study the effect of p-layer thickness on our solar cell performance.

For this test, a-Si:H n-i-p solar cells were fabricated with different p-layer thicknesses of 15 nm (g-141203-2), 25 nm (g-141203-1), and 50 nm (g-141201-1). The gas flow ratio of $[B_2H_6]/[B_2H_6+H_2]$ was 0.67 % while SiH_4 and H_2 were constant at 40 sccm and 80 sccm, respectively. The thickness of intrinsic a-Si:H (i-layer) and n-type a-Si:H (n-layer) was fixed at 350 nm and 30 nm, respectively. The other deposition conditions were the same for all the solar cell layers; substrate temperature, process pressure, RF power were kept at 150 °C, 900 mTorr, and 2 W, respectively.

Figure 4.1 shows (a) J-V characteristics and (b) solar cell performance parameters of a-Si:H n-i-p solar cells for different p-layer thickness. The device performance parameters are also listed in Table 4.1. It is seen that a-Si:H solar cell with thinner p-layer shows higher J_{sc}, hence higher η. Although V_{oc} does not change significantly, the increase in J_{sc} is from 3.10 mA/cm^2 to 4.71 mA/cm^2 when decreasing p-layer thickness. This result is attributed to higher optical transmittance of p-layer which leads to improve carrier generation in i-layer. However, FF decreases from 58.34 % to 53.76 % at low p-layer thickness, which is

probably related to decreased R_{sh} (see in Table 4.1). Overall η is improved from 1.35 % to 1.84 % when decreasing p-layer thickness from 50 nm to 15 nm (Figure 4.1(b)).

Table 4.1: Device performance parameters for different thicknesses of p-layer.

Cell	g-141201-1	g-141203-1	g-141203-2
p-layer thickness (nm)	15	25	50
V_{oc} (V)	0.774	0.742	0.743
J_{sc} (mA/cm^2)	4.71	3.88	3.10
FF (%)	53.76	57.40	58.34
η (%)	1.84	1.65	1.35
R_s (Ωcm^2)	12.52	14.60	14.95
R_{sh} (Ωcm^2)	2.25×10^4	4.43×10^4	3.99×10^4

Figure 4.2 shows the spectral response characteristics of a-Si:H n-i-p solar cells with different p-layer thicknesses corresponding to Figure 4.1. One can see that EQE is increased over the entire wavelength region from 400 nm to 700 nm by reducing the p-layer thickness. The presence of interference fringes in the wavelength range above 600 nm is related to the cell reflection spectra [66]. This result means that more light comes through p-layer to i-layer. Thus, EQE results well agree with improved J_{sc} at lower p-layer thickness.

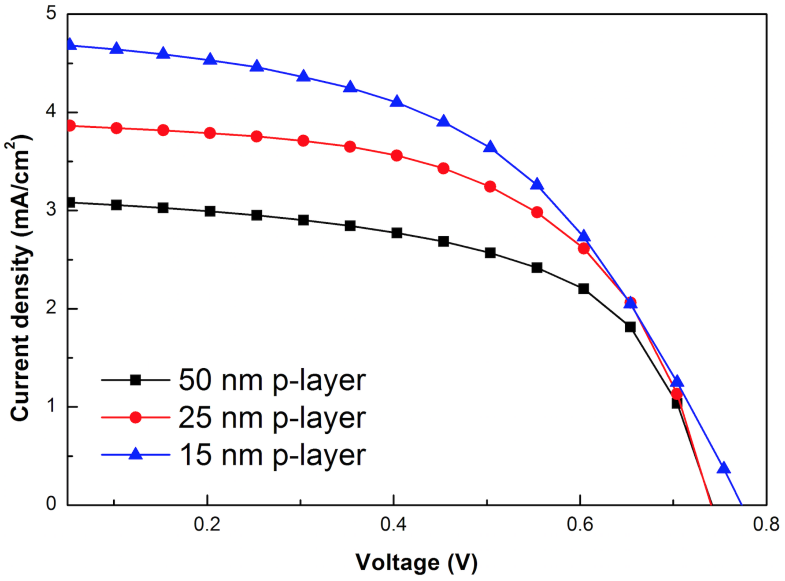

(a)

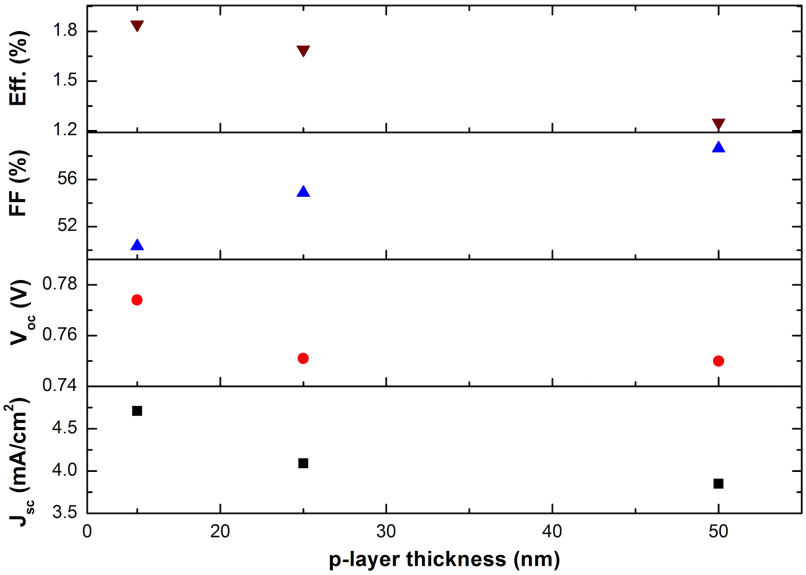

(b)

Figure 4.1: (a) J-V characteristics and (b) solar cell performance parameters of a-Si:H n-i-p solar cells with different p-layer thicknesses.

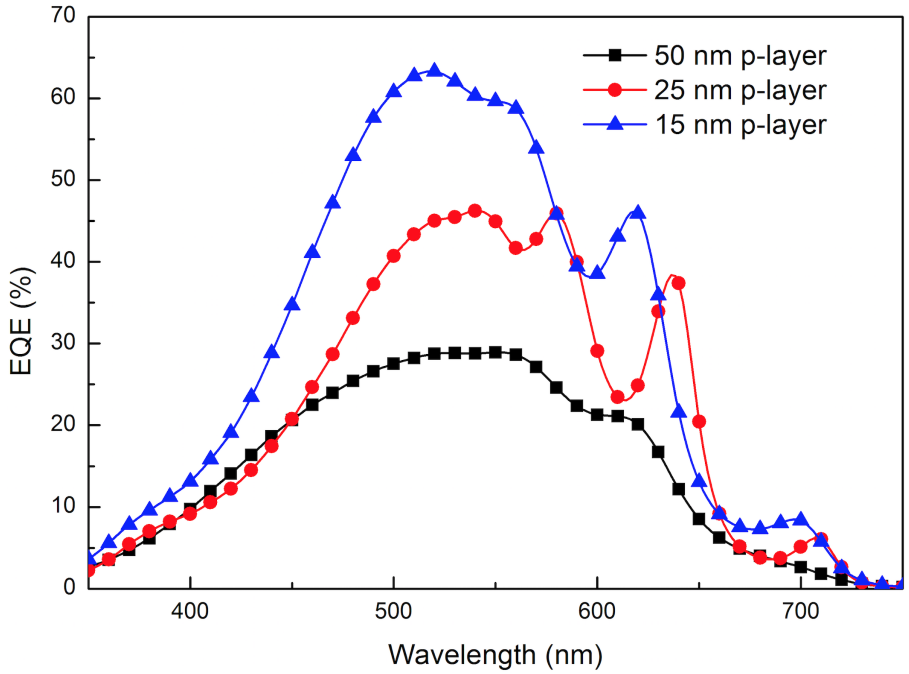

Figure 4.2: Spectral response characteristics of a-Si:H n-i-p solar cells with different p-layer thicknesses corresponding to Figure 4.1.

4.1.2 Incorporating p-type a-SiC:H window layer

Even though the J_{sc} was increased with engineering p-layer thickness, the value of J_{sc} (~4.5 mA/cm^2) is still low compared to the state of art for low-temperature solar cells published (~10 mA/cm^2) [49]. The main reason may be due to the use of p-type a-Si:H. p-type a-Si:H shows lower E_g (~1.65 eV) compared to intrinsic a-Si:H (E_g of ~1.75 eV) [49]. The absorption of the p-layer is the limiting factor for J_{sc}.

p-type a-SiC:H (p-a-SiC:H) layer shows higher E_g (~2 eV) dependent on C content in the films [49], and can be used in a-Si:H solar cell p-layer as a high E_g window layer. High E_g (~1.98 eV) of p-a-SiC:H was also confirmed in section 3.3.2. Indeed, a-Si:H solar cells adopting p-a-SiC:H layer as a p-layer are expected to show higher J_{sc} and V_{oc} compared

to them with p-a-Si:H as a p-layer. Hence, we study the effect of p-a-SiC:H layers as a window layer on a-Si:H solar cell performance.

For this test, a-Si:H n-i-p solar cells were fabricated with the p-layer employing the C atom introduced by using CH_4 gas. The p-layer doping gas mixture included SiH_4, 2 % B_2H_6 diluted in H_2, CH_4, and H_2. The gas flow of SiH_4 and H_2 was fixed at 15 sccm and 35 sccm, respectively. p-a-SiC:H, i-a-Si:H, and n-a-Si:H thin-film thickness kept at 20 nm, 350 nm, and 30 nm, respectively. Other deposition conditions are the same for all solar cell layers; substrate temperature and process pressure were kept at 150 °C and 900 mTorr, respectively. We varied the gas flow ratios of $[B_2H_6]/[CH_4]$ and RF power to characterize solar cell performance.

Figure 4.3 shows (a) J-V characteristics and (b) solar cell performance parameters at different $[B_2H_6]/[CH_4]$ ratio at constant RF power of 4 W. It is seen that J_{sc} is increased compared to p-a-Si:H layer. Furthermore, J_{sc} is increased from ∼6 mA/cm^2 to ∼7.4 mA/cm^2 with increasing $[B_2H_6]/[CH_4]$. However, V_{oc} does not change compared to that in p-a-Si:H based solar cells and even Schottky barrier behavior occurs for a low $[B_2H_6]/[CH_4]$=62.5 %. It is assumed that the low V_{oc} and FF observed may be related to a poor interface of p-SiC:H/a-Si:H. The band bending at AZO/p-a-SiC:H interface may degrade built-in potential and charge collection (Figure 4.4) [67], thereby showing a poor device performance. Nevertheless, the overall efficiency improves from 1.27 % to 2.38 % with increasing $[B_2H_6]/[CH_4]$ from 62.5 % to 88.9 % as shown in Figure 4.3(b).

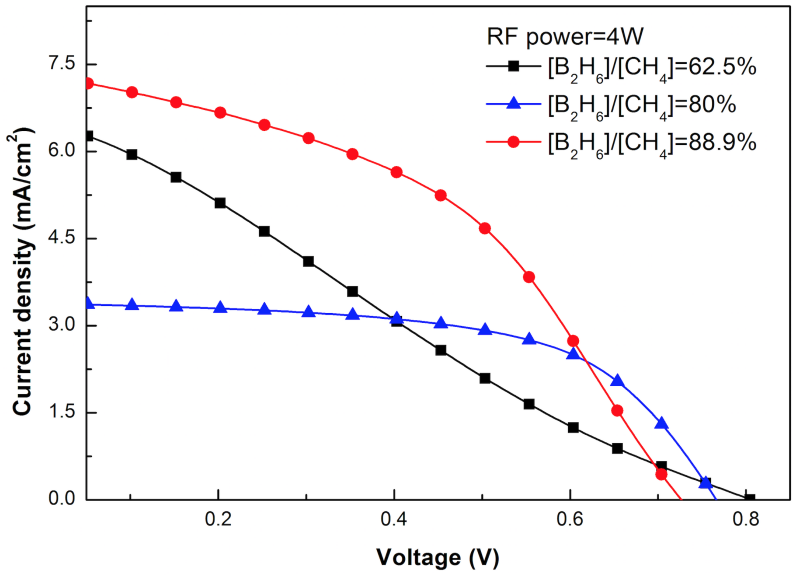

(a)

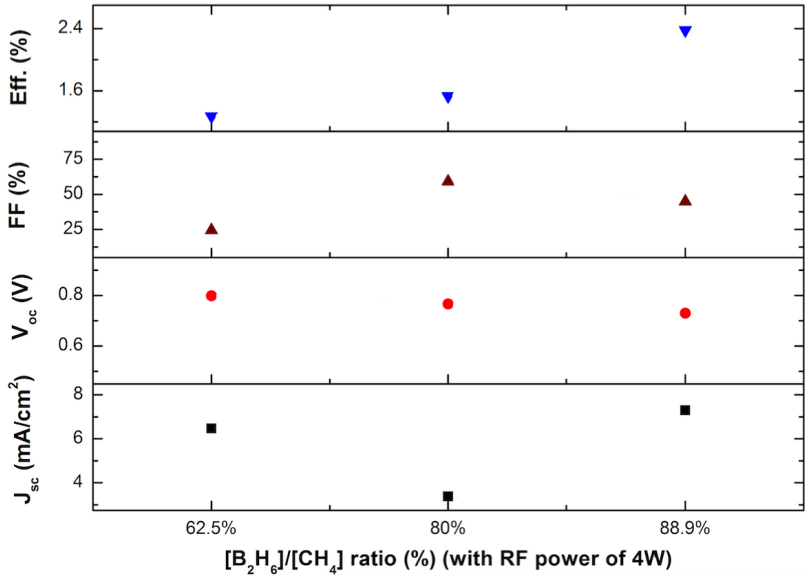

(b)

Figure 4.3: (a) J-V characteristics and (b) solar cell performance parameters at different $[B_2H_6]/[CH_4]$ ratio at constant RF power of 4 W.

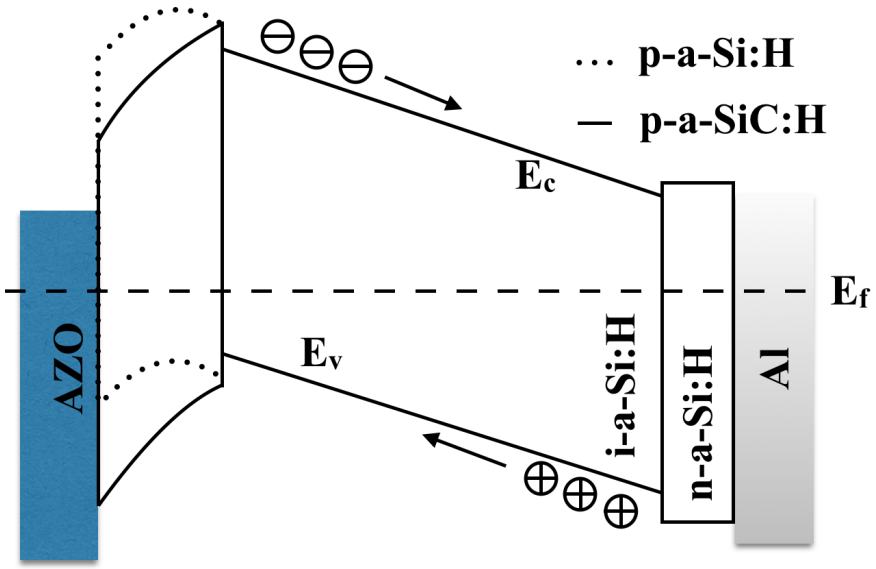

Figure 4.4: Band diagram of a-Si:H solar cell with p-a-SiC:H layer.

Figure 4.5 shows (a) J-V characteristics and (b) solar cell performance parameters for different RF powers used in deposition process of p-a-SiC:H for constant $[B_2H_6]/[CH_4]$=62.5 %. It is seen that both J_{sc} and FF increase at lower RF power, thereby increasing cell efficiency. For the solar cell with p-a-SiC:H layer deposited at low RF power of 2 W, the J_{sc}, V_{oc}, FF, and η are 7.92 mA/cm^2, 0.67 V, 53.73 %, and 2.86 %, respectively (Figure 4.5(b)). This result implies that the interface of p-a-SiC:H/i-a-Si:H is subject to damage presumably by ion bombardment during deposition at higher RF power, which leads to poorer device performance. Furthermore, V_{oc} value is lower than in the case of solar cell with p-type a-Si:H layer. This can be attributed to band mismatch between p-a-SiC:H and i-a-Si:H layers due to E_g difference (E_g=1.98 eV for p-a-SiC:H and E_g=1.72 eV for i-a-Si:H). This issue needs to be addressed. We will study interface engineering and its effect on solar cell performance in Chapter 5.

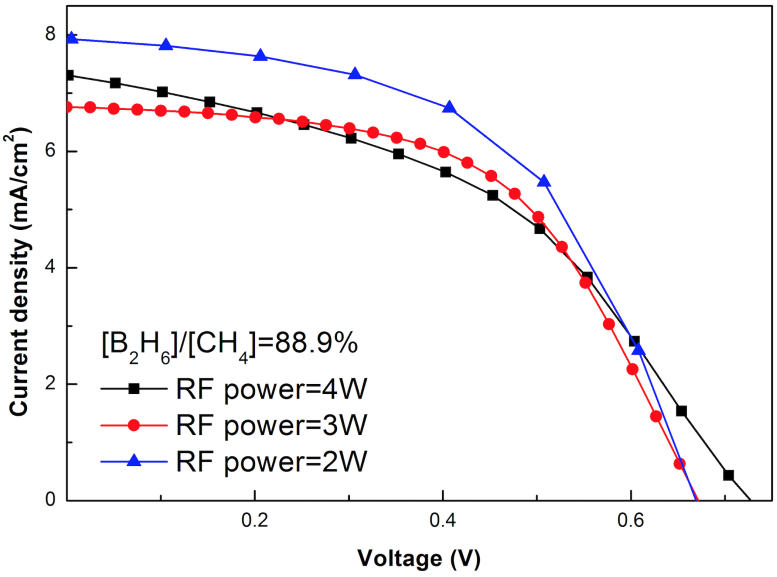

(a)

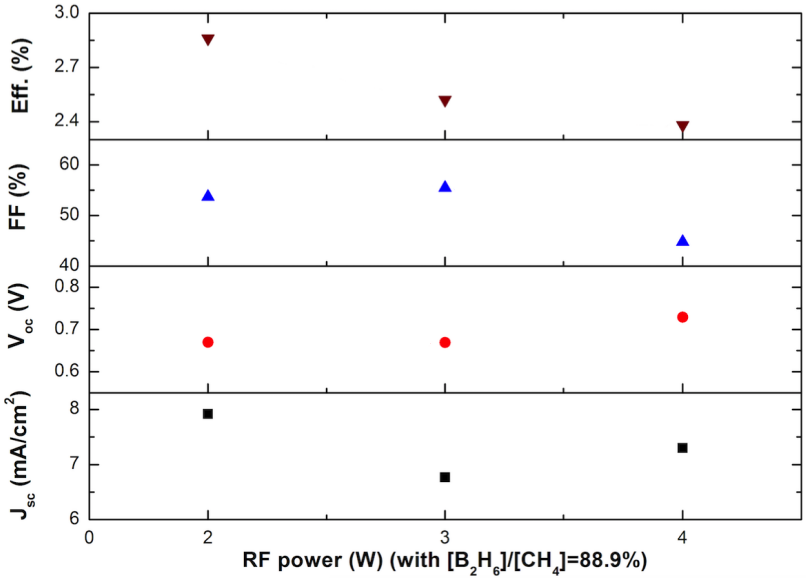

(b)

Figure 4.5: (a) J-V characteristics and (b) solar cell performance parameters for different RF powers used in deposition process of p-a-SiC:H for constant $[B_2H_6]/[CH_4]$=62.5 %.

4.2 Characterization of PV modules

The size of PV module was 10×10 cm^2 which consists of 72 rectangular sub-cells (Figure 4.6(a)), and inset figure shows magnified layout of two cells connected in series. The sub-cells were connected in series forming eight rows with connection pads. Figure 4.6(b) shows the photograph of PV module under bending. Its interconnections are illustrated in Figure 4.6(c).

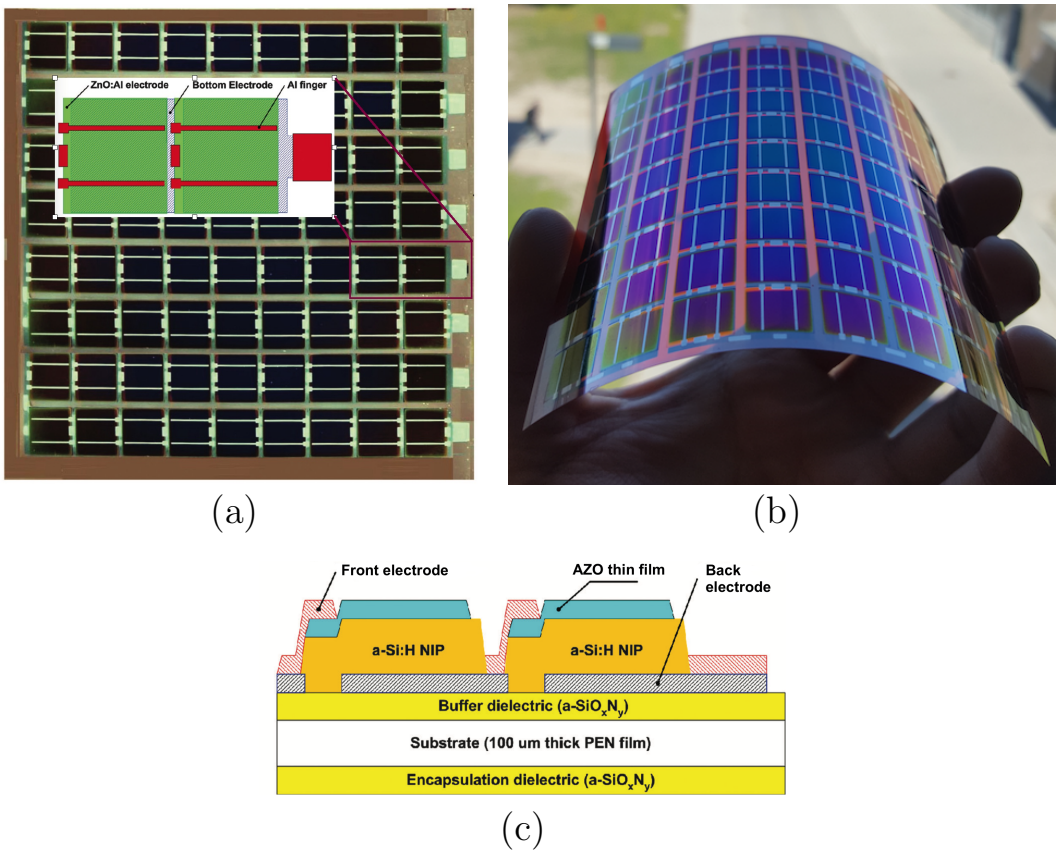

Figure 4.6: (a) Layout of the PV module, (b) photograph of PV module under bending, and (c) cross-sectional view of the cells. Inset of Figure 4.6(a) shows magnified layout of two cells connected in series.

4.2.1 Simulation of contact layers for PV module

Figure 4.7 shows (a) equivalent circuit of the sub-cell and (b) simulated cell with uniform mesh. An equivalent circuit of the sub-cell includes a diode, a current source representing current generation in the n-i-p structure, the resistors, including the resistance of the p-layer and contact resistance of the interface of p/AZO (R_p), the top metallization resistor (R_x), and resistance of AZO (R_y), respectively (Figure 4.7(a)). The sub-cell is divided into rectangular parts with a node at the centre of each sub-cell (Figure 4.7(b)). Note that R_{sh} of the bottom metal is at least two orders of magnitude lower than that of the AZO film, and the R_s component is not taken into account. Nodes at the front edge of Al grid are defined as the current sink in this model with the boundary condition being the applied bias.

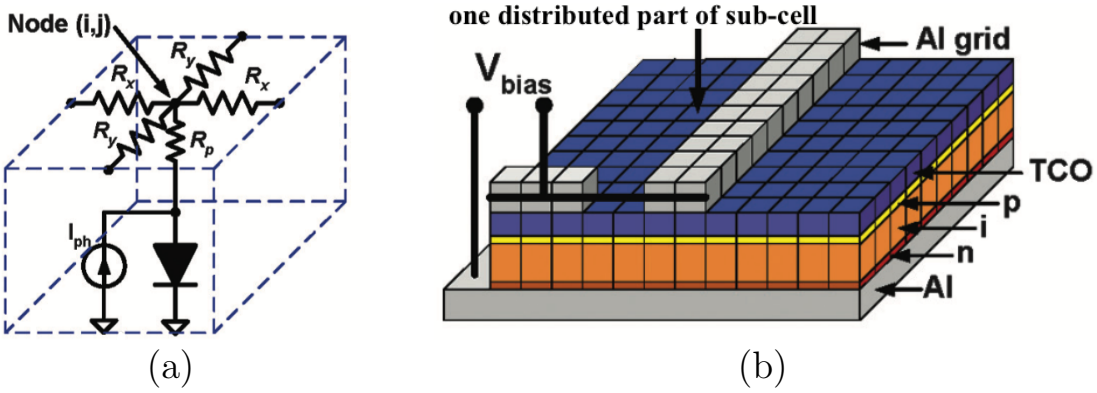

Figure 4.7: (a) Equivalent circuit of the sub-cell and (b) simulated cell with uniform mesh.

The diode forward current is:

$$I = J_0 L_x L_y [exp(\frac{qV}{nkT}) - 1] \tag{4.1}$$

Here: J_0 is the saturation current density, L_x and L_y are the sub-cell dimensions in the direction X and Y, respectively. q is the elementary charge, n is the photo-diode ideality factor, k is Boltzmann's constant, and T is the temperature. The output of the current source is:

$$I_{ph} = J_{ph} L_x L_y \tag{4.2}$$

Here: J_{ph} is the photo-current density. For n-i-p cells, J_{ph} is the bias voltage dependent function [68]:

$$J_{ph} = J_{ph,0} \frac{V - V_{bi}}{V_r} [1 - exp(\frac{V_\mu}{V - V_{bi}})] \tag{4.3}$$

$$V_\mu = \frac{{d_i}^2}{\mu\tau} \tag{4.4}$$

Here: $J_{ph,0}$ is the photo-current, V_{bi} is the built-in voltage, d_i is the intrinsic layer thickness, and τ is the mobility lifetime product also known as the drift length of the carriers.

Figure 4.8 shows (a) simulated I-V curve and (b) potential distribution across the emitter (top surface of the cell) at the bias voltage of 0.5 V. Input parameters used for simulation are J_0=2.3×10^{-20} A/cm^2, n=1.4, V_{bi}=1.1 V, V_μ=0.1 V, R_p=1.5 Ωcm^2, and $J_{ph,0}$=9 mA/cm^2. Here, the voltage drop across the Al finger is 10 V and voltage variation across the transparent electrode is up to 50 mV at 0.4 Ω/□ and 100 Ω/□ are the shunt resistances of the respective layers. Joule losses in the Al finger and AZO electrode are 22 μW and 61 μW, respectively.

Based on those simulation values, the thickness of the transparent electrode was optimized to minimize the optical and electrical losses. Reflection minimum of TCO coating at the wavelength, λ_0, is at discrete values of film thickness (equation (4.5)):

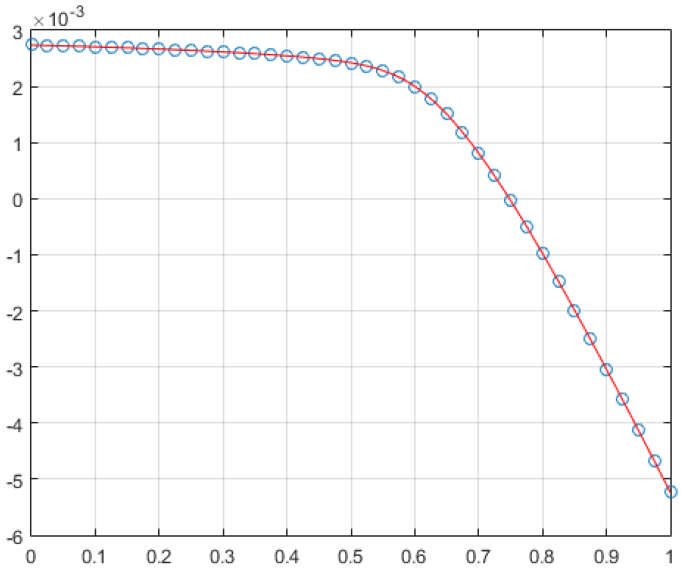

(a)

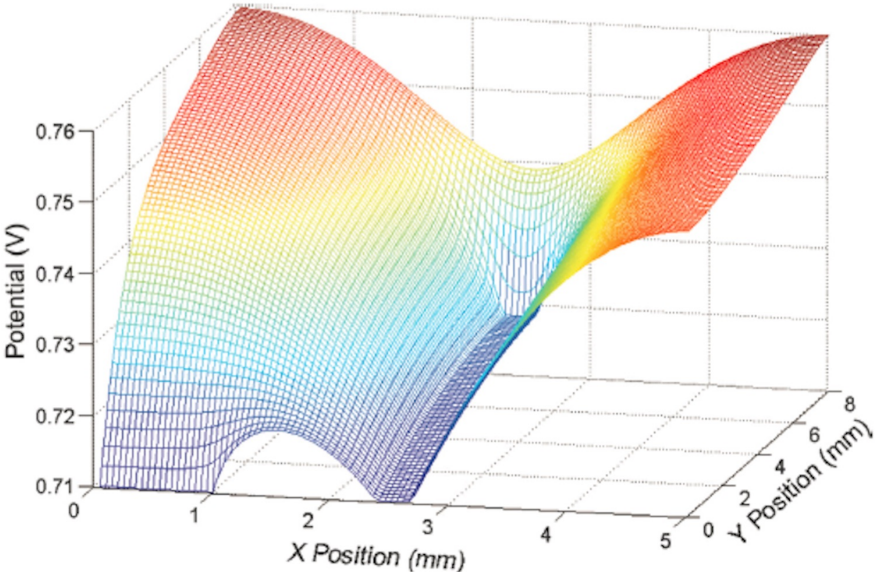

(b)

Figure 4.8: (a) Simulated I-V curve and (b) potential distribution across the emitter at a biasing voltage of 0.5 V.

$$d_{TCO} = \frac{\lambda_0(2m+1)}{4n_r} \tag{4.5}$$

Here: n_r is the refractive index at 0, and m = 0, 1, ...

Figure 4.9 shows (a) the calculated Joule losses in the Al and AZO top layers and (b) simulated solar cell parameters (η and FF) as a function of AZO thickness. Higher thickness leads to the reduction of Joule losses in the emitter and to FF enhancement due to decreasing R_s. However, the η reaches its peak value at a thickness of $3\lambda_0/4n_r$, then it decreases due to higher absorption loss. We performed device simulation at AZO thicknesses that corresponds to the first four reflection minima at λ_0=460 nm. To consider the absorption loss within the AZO layer, $J_{ph,0}$ was calculated for the given film thicknesses using α of AZO film measured in the visible wavelength range. Based on this modelling result, AZO thickness in the module structure was chosen to be at 200 nm.

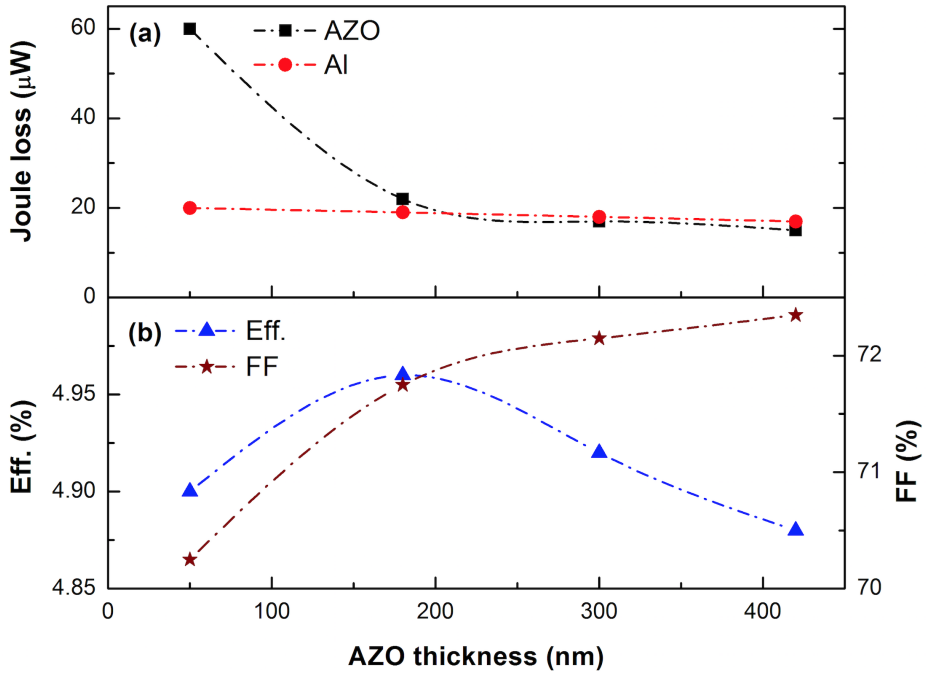

Figure 4.9: (a) The calculated Joule losses in the AZO and Al top layers and (b) simulated solar cell parameters (η and FF) as a function of AZO thickness.

Figure 4.10 shows (a) the calculated Joule losses in the AZO and Al top layers and (b) simulated solar cell parameters (η and FF) as a function of R_{sh}. Apparently the metal grid resistance must be lower than the resistance of AZO to minimize Joule losses. For our AZO electrode with 60 Ω/□ R_{sh}, metal R_{sh} has to be below 0.4 Ω/□. 150 nm thick Al layer with 0.25 Ω/□ was chosen for modules as a tradeoff between the sputtering time and device performance.

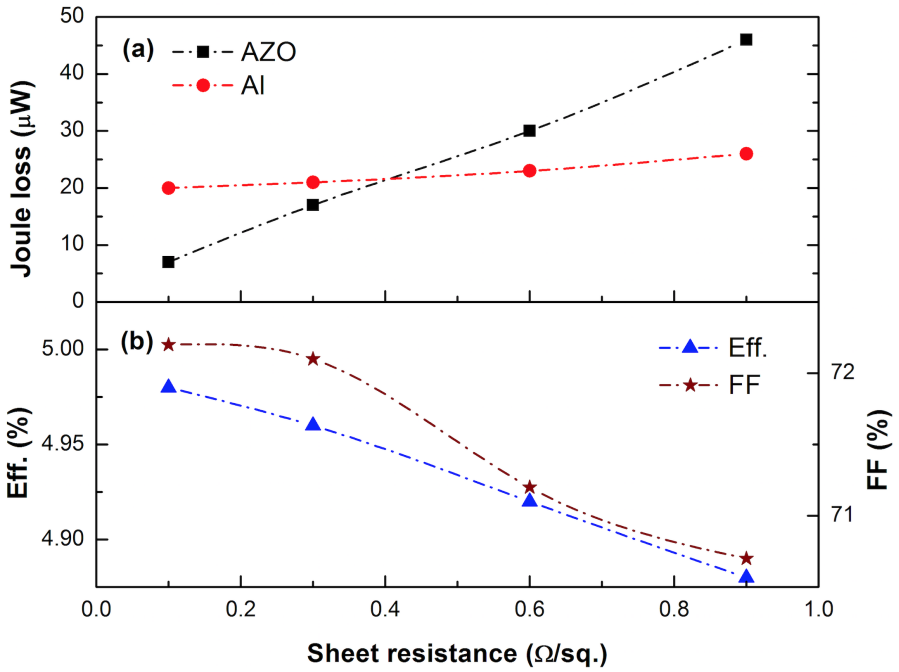

Figure 4.10: (a) The calculated Joule losses in the AZO and Al top layers and (b) simulated solar cell parameters (η and FF) as a function of R_{sh}.

4.2.2 PV modules performance

Figure 4.11 shows J-V characteristics of two random chosen sub-cells from different PV modules. The performance parameters are also listed in Figure 4.11. J_{sc}, V_{oc}, FF, and η are observed to be 8±0.17 mA/cm^2, 0.67±0.01 V, 50±4 %, and 2.75±0.1 %. Low deviation of all performance parameters for the sub-cells and for sub-cells presented in section 4.1.2, suggests that our fabrication processing is reproducible and scalable.

J-V characteristics of several PV modules fabricated are shown in Figure 4.12. Device performance parameters are also listed in Table 4.2. In the module, J_{sc} and FF are limited by the smallest J_{sc} shown by a sub-cell in the string while V_{oc} is added up for all the sub-cells. Based on the sub-cell performance from Figure 4.11, the values of J_{sc}, V_{oc}, and

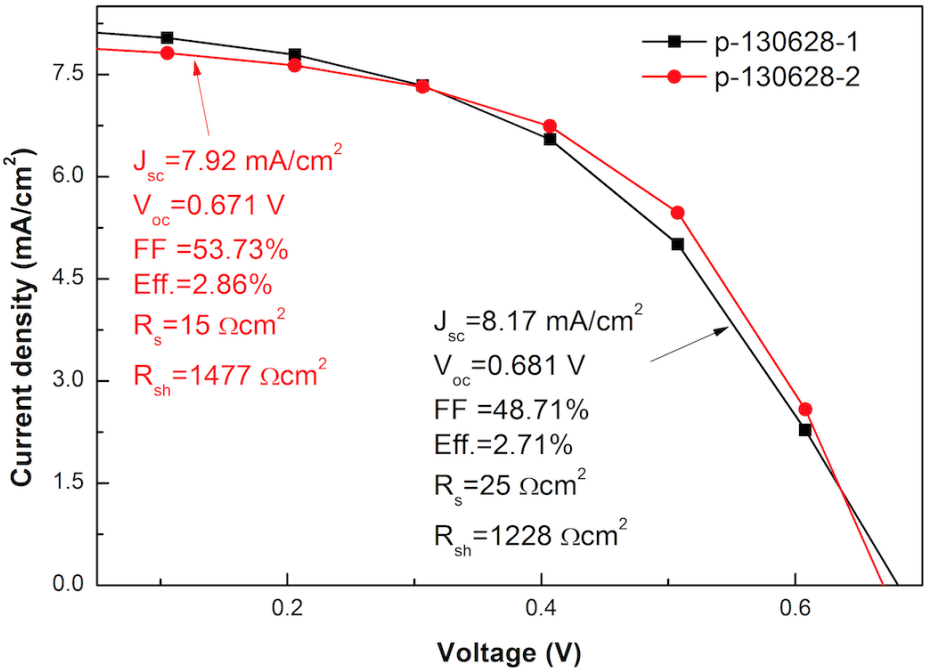

Figure 4.11: J-V characteristics of two random chosen sub-cells from different PV modules.

FF in one module can be expected to be 8±0.17 mA/cm^2, 10.475±2.5 V, and 50±4 %, respectively. J_{sc} and FF seem to be in the expected value range, while V_{oc} shows a higher variation between the strings. We assume that this may be due to the mismatch of sub-cells in the module.

Table 4.2: Device performance parameters for several mini PV module strings.

Cell	p-130404-1	p-130404-2	p-130318-2	p-130318-4	p-130318-5
V_{oc} (V)	10.475	9.103	13.099	11.139	11.064
J_{sc} (mA/cm^2)	8.12	8.14	7.66	7.86	7.89
FF (%)	54.39	58.23	55.18	52.52	52.90
Average η (%)	2.57	2.40	3.08	2.56	2.56

In real cases, all the sub-cells in a module may be not identical in terms of device performance. In addition, illumination may not be uniform, which affects the device per-

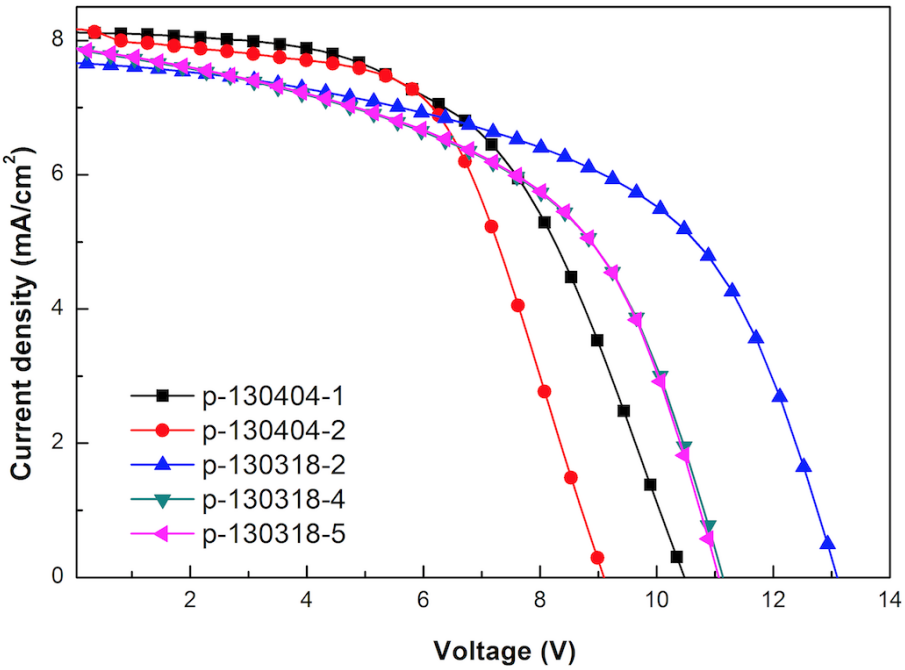

Figure 4.12: J-V characteristics of several PV module strings (18 sub-cells connected in series).

formance. Such variation of electrical output in sub-cells is called "mismatch". Figure 4.13 shows mismatch in voltage and current for cells in series.

For the mismatch in voltage connected in series, since the voltage just adds up (V_{oc}=V_1+V_2), the resulting overall V_{oc} will be the sum of all V_{oc}s in the string. For the mismatch in current for the cells connected in series, the resulting overall J_{sc} will be the same as that of worst J_{sc} cell because the current is limited by the smallest J_{sc} flowing through sub-cell (I_{sc}=I_{sc1}) [53]. Based on the mismatch in sub-cells in the module, we suspect that observed variation in V_{oc} values may be due to non-uniformity interfaces of AZO/p-layer/i-layer, which affects V_{oc} in sub-cells.

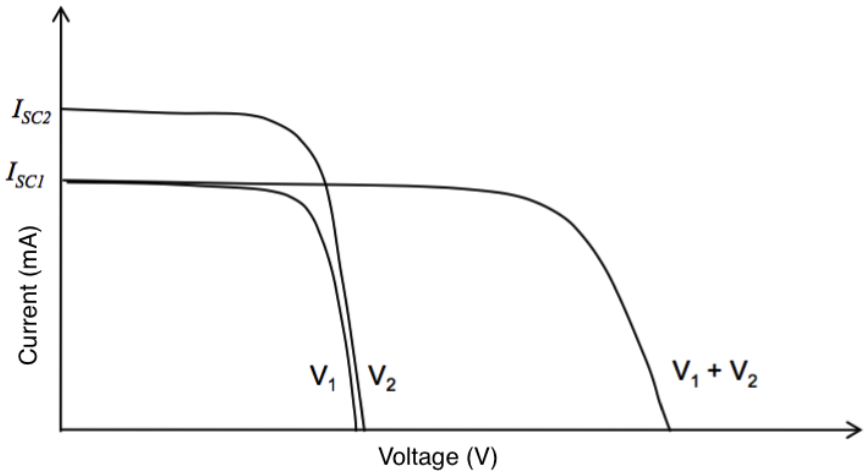

Figure 4.13: Mismatch in voltage and current for cells connected in series (modified from [53]).

4.3 Chapter summary

In this chapter, we discuss fabrication and characterization of low-temperature a-Si:H n-i-p solar cells. It was found that optimizing p-a-Si:H thickness and bandgap were important to improve the solar cell performance. The a-Si:H n-i-p solar cells with 15 nm thick p-a-SiC:H (p-layer) window layers resulted in J_{sc} of 8±0.17 mA/cm^2, V_{oc} of 0.67±0.01 V, FF of 50±4 %, and η of 2.75±0.1 %. To characterize the device design for PV module, two-dimensional simulation was performed and suggested the optimized AZO thickness (∼200 nm) for low Joule loss. Monolithic a-Si:H PV modules were fabricated on the plastic substrate using 150 °C deposition temperature. The sub-cell which randomly chosen from the modules shows J_{sc} of 7.92 mA/cm^2, V_{oc} of 0.67 V, FF of 53.73 %, η of 2.86 % comparable to those of sub-cells. Although there are some performance variations due to mismatch in sub-cell, the best module η was ∼3 %.

Chapter 5

Fabrication and Characterization of P-I-N Solar Cells

Results of the fabrication and characterization of a-Si:H n-i-p solar cells and flexible PV module are shown in Chapter 4. a-Si:H p-i-n solar cells are fabricated on glass substrates; where the cell structure is inverted from substrate to superstrate configuration. The initial device performance and issues in a-Si:H p-i-n solar cells are discussed in section 5.1. In section 5.2, effect of p-type buffer-layer on solar cell performance is discussed, and the effect of p-layer thickness on a-Si:H p-i-n solar cell performance is also investigated.

5.1 a-Si:H p-i-n solar cells: device performance

5.1.1 Initial device performance of a-Si:H n-i-p and p-i-n solar cells

For the fabrication of a-Si:H p-i-n solar cells, the deposition recipes used to fabricate n-i-p solar cells were used at first. The fabrication of a-Si:H p-i-n solar cells started with deposition of 200 nm thick AZO film on glass substrate, and then a-Si:H p-i-n stack was continuously deposited using the same deposition recipes for layers as mentioned in Chapter 4. Finally, 150 nm thick Al film was sputtered and patterned using standard lithography process to form the back electrode. Fabricated a-Si:H p-i-n solar cells are shown in Figure 5.1.

Figure 5.2 shows J-V characteristics of a-Si:H p-i-n solar cell on glass substrate. J-V characteristics of a-Si:H n-i-p solar cell fabricated using the same deposition recipes is also shown here for comparison. The device performance parameters are also listed in Table 5.1. Even though the V_{oc} value of 0.77 V is comparable to that of a-Si:H n-i-p solar cells, the J_{sc} of 3.83 mA/cm^2 and FF of 28.66 % are significantly lower, thus showing η of 0.83 %. In particular, the shape of J-V characteristics shows dominance of series and shunt resistances. From Table 5.1, the values of R_{sh} and R_s are about two orders of magnitude lower and about 20 times higher, respectively, compared to those of a-Si:H n-i-p solar cells. Although it is hard to distinguish which of them has most significant effect on degradation of J-V characteristics, based on the values of R_{sh} and R_s, p-i-n device may be assumed to have poor junction interface and/or bulk properties. However, the bulk properties of both devices are believed to be similar. Thus, the main focus of optimization was determined to the junction interface, which may result from the different structure for both devices.

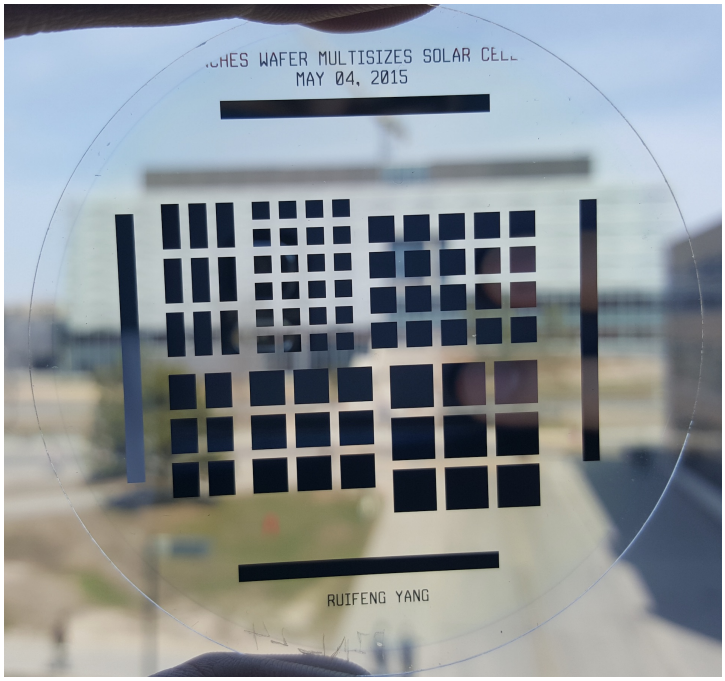

Figure 5.1: Photograph of a-Si:H p-i-n solar cells on glass substrate.

The n-i-p structure consists of glass/back metal/a-Si:H n-i-p stack/front AZO, while the p-i-n structure is composed of glass/front AZO/a-Si:H p-i-n stack/back metal [69]. It is generally believed that the anode parts of metal/n-i and i-n/metal for the n-i-p and p-i-n devices, respectively, do not create the transport issue because the collection efficiency of electron is high due to its high mobility [70]. So, we assumed that the difference in cathode parts may be a main source of resistances. In the cathode parts, poor hole transport and ohmic contact may affect device performance. The AZO/p-i part for the p-i-n device thus seems to be different from the i-p/AZO for the n-i-p device in terms of carrier transport and interface. It will be further studied in details next section.

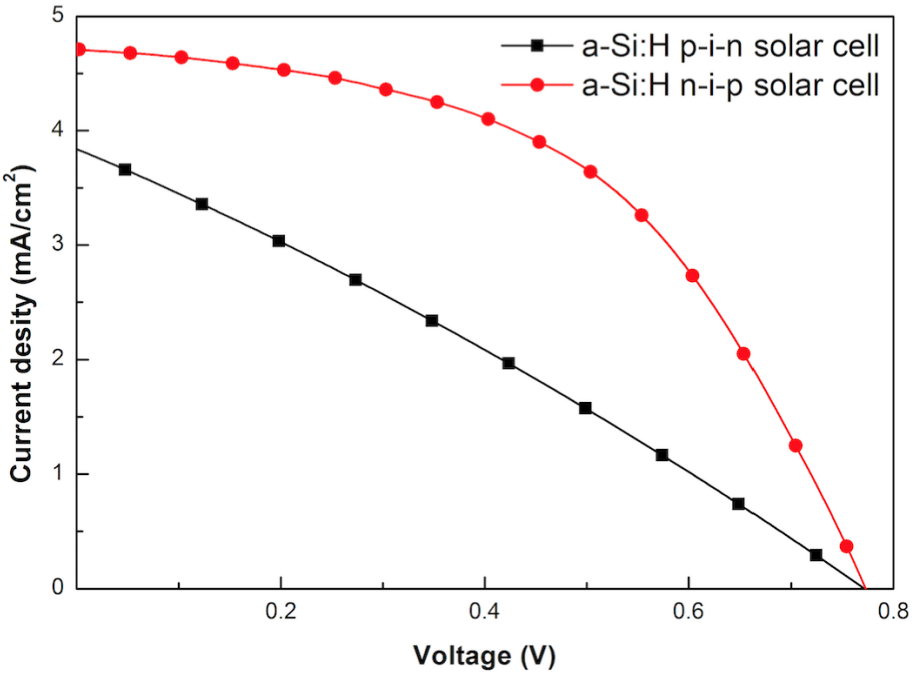

Figure 5.2: J-V characteristics of initial a-Si:H p-i-n solar cell on glass substrate along with J-V curve of a-Si:H n-i-p solar cell.

Table 5.1: Device performance parameters of initial a-Si:H p-i-n solar cell and a-Si:H n-i-p solar cell with the same deposition recipes.

Cell	g-150413-1	g-141201-1
V_{oc} (V)	0.77	0.77
J_{sc} (mA/cm^2)	4.71	3.83
FF (%)	53.76	28.26
η (%)	1.84	0.83
R_{sh} (Ωcm^2)	2.25×10^4	136.24
R_s (Ωcm^2)	12.52	273.84

5.2 Efficiency improvement in p-i-n solar cells

5.2.1 Effect of p-type buffer-layer on solar cell performance

p-type a-Si:H buffer-layer (namely Δp-layer in this thesis) was deposited using 2 % B_2H_6 diluted by H_2, mixed with SiH_4 as the source gas. The gas flow of H_2 was fixed at 80 sccm. We varied the gas flow ratio of $[B_2H_6]/[SiH_4]$ from 0.2 % to 2 % at RF power of 10 W, and the Δp-layer thickness was selected to be 15 nm and 10 nm. p-type a-Si:H, intrinsic a-Si:H, and n-type a-Si:H thin-film layers were kept at 15 nm, 350 nm, and 15 nm, respectively. Other deposition conditions were the same for all the solar cell layers; substrate temperature, process pressure, and RF power were kept at 150 °C, 900 mTorr, and 2 W, respectively.

Figure 5.3 shows J-V characteristics of a-Si:H p-i-n solar cells with different $[B_2H_6]/[SiH_4]$ ratio of Δp-layer of constant thickness of 15 nm, along with J-V curve of solar cell fabricated without Δp-layer for comparison. Device performance parameters are also listed in Table 5.2. Note that solar cells with Δp-layer show improved performance compared to that without Δp-layer. Furthermore, increasing $[B_2H_6]/[SiH_4]$ ratio leads to V_{oc} and FF increase from 0.8 V to 0.87 V and from 48 % to 50.91 %, respectively. This is attributed to improve AZO/p-a-Si:H interface. Also, the Δp-layer deposited with high doping gas ratio is expected to reduce contact resistance of AZO/p-a-Si:H interface. However, the J_{sc} value (7.89 mA/cm^2) is lower at 2 % $[B_2H_6]/[SiH_4]$ ratio than at 0.2 % $[B_2H_6]/[SiH_4]$ ratio (8.43 mA/cm^2) which means that there still may exist some absorption and/or carrier recombination using highly doped Δp-layer.

In order to increase photon transmission into i-layer, thinner Δp-layer was deposited (minimum Δp-layer thickness was found to be 10 nm). Figure 5.4 shows J-V characteristics

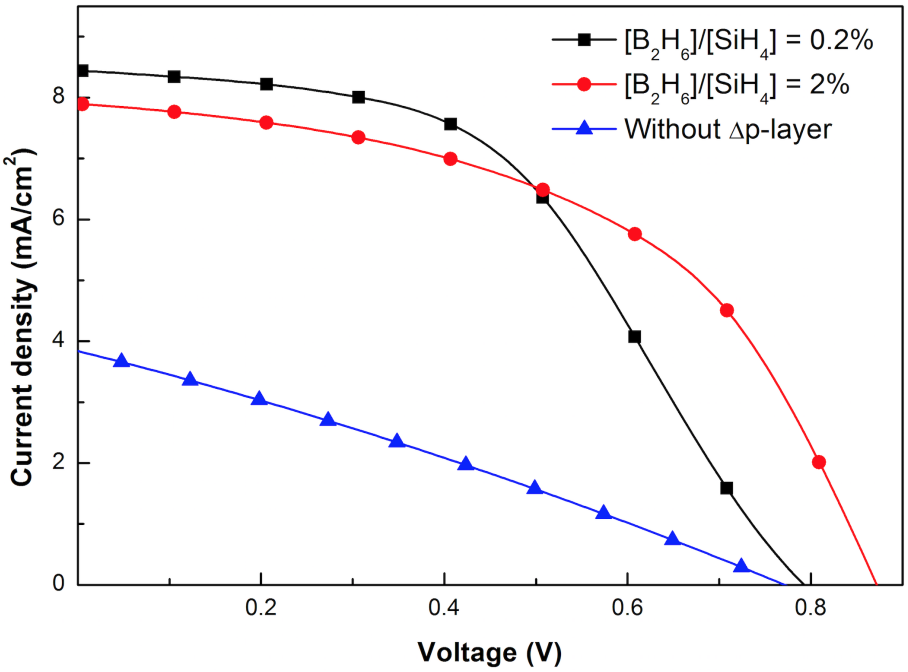

Figure 5.3: J-V characteristics of a-Si:H p-i-n solar cells with Δp-layer fabricated at different $[B_2H_6]/[SiH_4]$ ratios and thickness of 15 nm, along with the J-V curve without Δp-layer for comparison.

Table 5.2: Device performance parameters at different $[B_2H_6]/[SiH_4]$ ratio of Δp-layer.

Cell	g-150525-1	g-150525-2	g-150211-2
$[B_2H_6]/[SiH_4]$ ratio (%)	0.2 %	2 %	-
V_{oc} (V)	0.80	0.87	0.77
J_{sc} (mA/cm^2)	8.43	7.89	3.83
FF (%)	48.28	50.91	28.26
η (%)	3.27	3.50	0.83
R_{sh} (Ωcm^2)	32.29	23.21	136.24
R_s (Ωcm^2)	85.49	23.60	273.84

of a-Si:H p-i-n solar cells with 10 nm Δp-layer thickness in comparison with that for 15 nm Δp-layer thickness. Device performance parameters are also listed in Table 5.3. It can be seen that the change in the Δp-layer thickness does not affect V_{oc} and J_{sc}. However,

FF is slightly increased at lower Δp-layer thickness, thereby improving the cell efficiency from 3.27 % to 3.50 %. It is attributed to reduction of R_s.

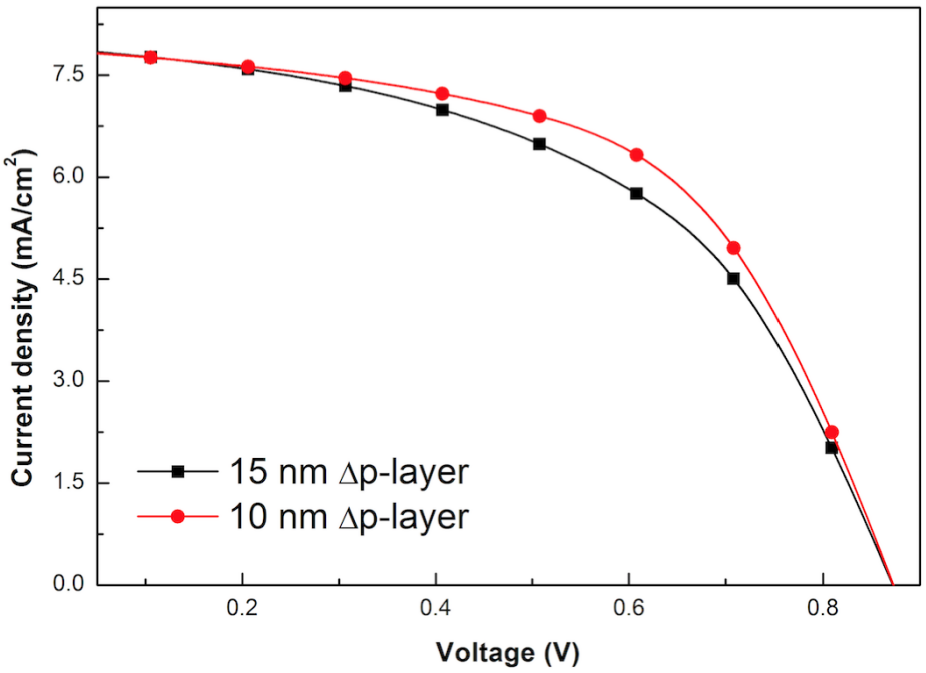

Figure 5.4: J-V characteristics of the a-Si:H p-i-n solar cells with 10 nm and 15 nm thick Δp-layer.

Table 5.3: Device performance parameters of solar cells with different thickness of Δp-layer.

Cell	g-150612-2	g-150525-4
Δp thickness (nm)	15	10
V_{oc} (V)	0.872	0.873
J_{sc} (mA/cm^2)	7.89	7.87
FF (%)	50.91	56.17
η (%)	3.50	3.86
R_{sh} (Ωcm^2)	23.21	26.26
R_s (Ωcm^2)	23.60	20.28

Based on presented experimental results, device performance improvement of a-Si:H p-i-n solar cells can be explained by modification of work function by adding Δp-layer at the

interface of AZO/p-a-Si:H as shown in Figure 5.5. The work function difference between the AZO layer and p-a-Si:H layer causes band bending effect and builds high interface potential barrier, which impedes the extraction of photo-generated holes from intrinsic a-Si:H layer [69, 71]. Usually, conductive buffer-layer such as p-a-SiC:H or p-μc-Si:H enhances hole collection to lower interface potential barrier [72, 73]. The use of buffer-layer at the interface of TCO/p-a-Si:H results in an improvement of V_{oc}, due to lowering of Schottky barrier height [72]. This insertion can also reduce R_s at the interface of AZO/p-a-Si:H, and build an ohmic contact [74].

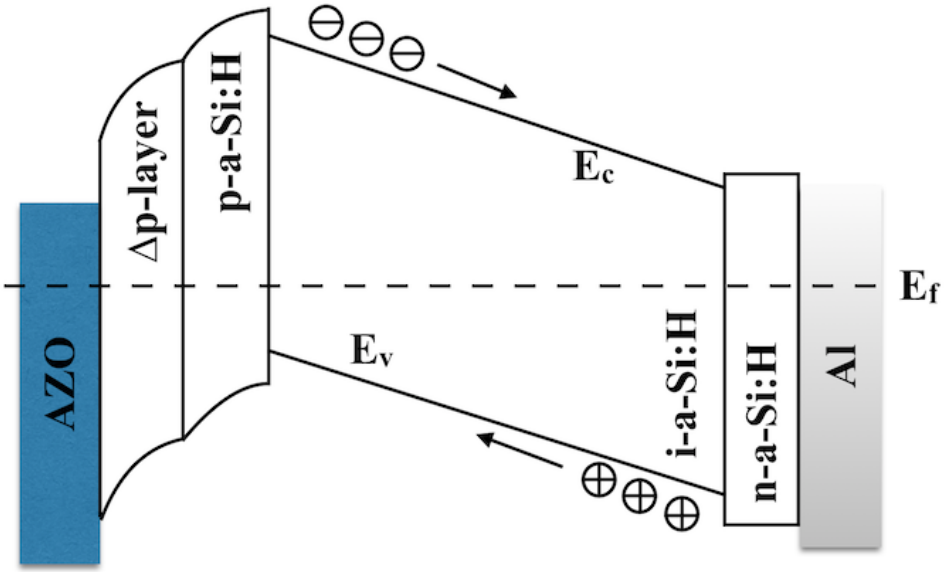

Figure 5.5: Schematic representation of a-Si:H p-i-n solar cell band diagram variation with Δp-layer at the interface of AZO/p-a-Si:H.

5.2.2 Effect of p-layer thickness on solar cell performance

Further study of the effect of p-layer total thickness on solar cell performance was carried out at Δp-layer thickness being kept constant. Figure 5.6 shows J-V characteristics of

a-Si:H p-i-n solar cells with different p-layer total thickness and 10 nm Δp-layer thickness. Device performance parameters are also listed in Table 5.4. It is observed that a-Si:H p-i-n solar cells with thinner p-layer show an increase in J_{sc} from 7.87 mA/cm^2 to 8.88 mA/cm^2, which is the same trend as shown in section 4.1.1. This result implies that more light can pass through p-layer into i-layer, thereby improving charge generation. However, FF decreases from 56.17 % to 52.01 % with decreasing p-layer thickness, which is related to increased contact resistance. Regardless of FF degradation, overall η is improved from 3.86 % to 4.09 % with decreasing p-layer thickness from 15 nm to 5 nm (Table 5.4).

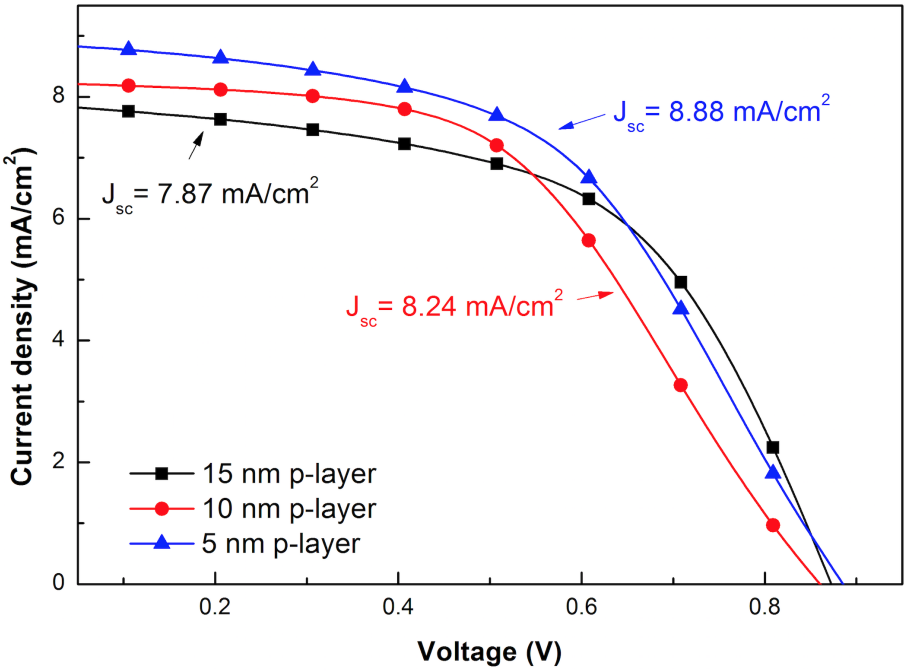

Figure 5.6: J-V characteristics of the a-Si:H p-i-n solar cells with different p-layer thickness and 10 nm Δp-layer thickness.

Figure 5.7 shows spectral response characteristics of a-Si:H p-i-n solar cells with different p-layer thickness at Δp-layer thickness corresponding to Figure 5.6. EQE is increased over the entire wavelength region from 400 nm to 700 nm by decreasing the p-layer thickness.

Table 5.4: Device performance parameters of a-Si:H p-i-n solar cells with different thickness of p-layer with buffer-layer thickness of 10 nm.

Cell	g-150525-4	g-150620-1	g-150620-2
p-layer thickness (nm)	15	10	5
V_{oc} (V)	0.873	0.862	0.885
J_{sc} (mA/cm^2)	7.87	8.24	8.88
FF (%)	56.17	51.94	52.01
η (%)	3.86	3.69	4.09

In addition, EQE curve shifts towards higher wavelength region at lower p-layer thickness [66]. This result means that more light comes through p-layer into intrinsic layer. Thus, EQE results well correspond to J_{sc} with decreasing p-layer thickness.

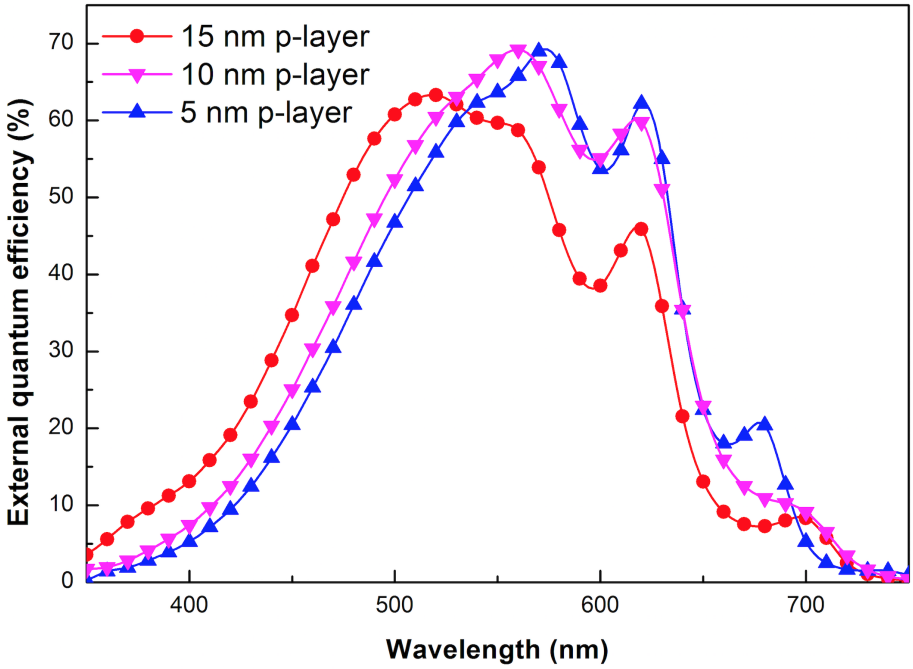

Figure 5.7: Spectral response characteristics of a-Si:H p-i-n solar cells for different p-layer thickness at 10 nm Δp-layer thickness corresponding to Figure 5.6.

5.3 Chapter summary

In this chapter, a-Si:H p-i-n solar cells were fabricated by inverting n-i-p structure on glass substrate. p-type buffer-layer inserted between the AZO layer and p-layer improves solar cell performance by lowering the interface potential barrier, and building up an ohmic contact. Moreover, more light pass through p-layer into i-layer, showing improvement in J_{sc} and hence energy conversion efficiency.

The efficiency is close to that previously reported for a-Si:H p-i-n solar cells [69]; the best measured efficiency was 4.09 % for an a-Si:H p-i-n solar cell fabricated on glass substrate.

Chapter 6

Fabrication and Characterization of Semi-transparent Solar Cells

In this chapter, we describe fabrication and characterization of semi-transparent a-Si:H p-i-n solar cells on glass and plastic substrates to investigate the feasibility of BIPV application using our current fabrication process. Characterization of semi-transparent a-Si:H p-i-n solar cells on glass substrates are presented in section 6.1. Section 6.2 discusses the characterization of semi-transparent a-Si:H p-i-n solar cells on plastic substrates, and the effect of barrier-layer. The semi-transparent a-Si:H p-i-n solar cells are used as radiation detectors and investigated the response in the visible part of spectrum is shown in section 6.3.

6.1 Semi-transparent a-Si:H p-i-n solar cells on glass substrate

For optically transparent solar cells, ∼200 nm thick AZO layers were used as electrodes instead of Al back reflective metal. The rest of solar cell structure was made using the conditions described in section 5.2.1. Figure 6.1 shows (a) schematic representation of device structure and (b) photograph of semi-transparent a-Si:H p-i-n solar cell fabricated on glass substrate.

Figure 6.2 shows transmittance spectra of semi-transparent a-Si:H p-i-n solar cell fabricated on glass and a bare glass substrate. Whereas the bare glass substrate shows over 90 % transparency over the measurement range, the average transparency of semi-transparent solar cell is over 60 % in the spectral region above 600 nm, which is suitable for BIPV applications.

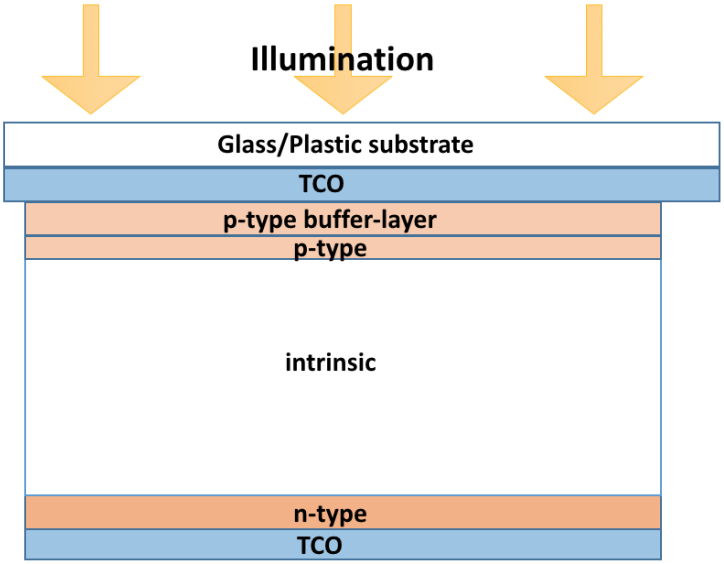

(a)

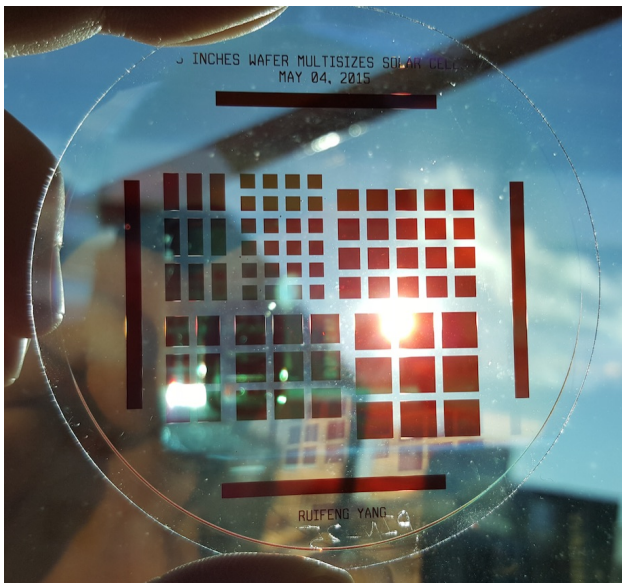

(b)

Figure 6.1: (a) Schematic representation of device structure and (b) photograph of semi-transparent a-Si:H p-i-n solar cell fabricated on glass substrate.

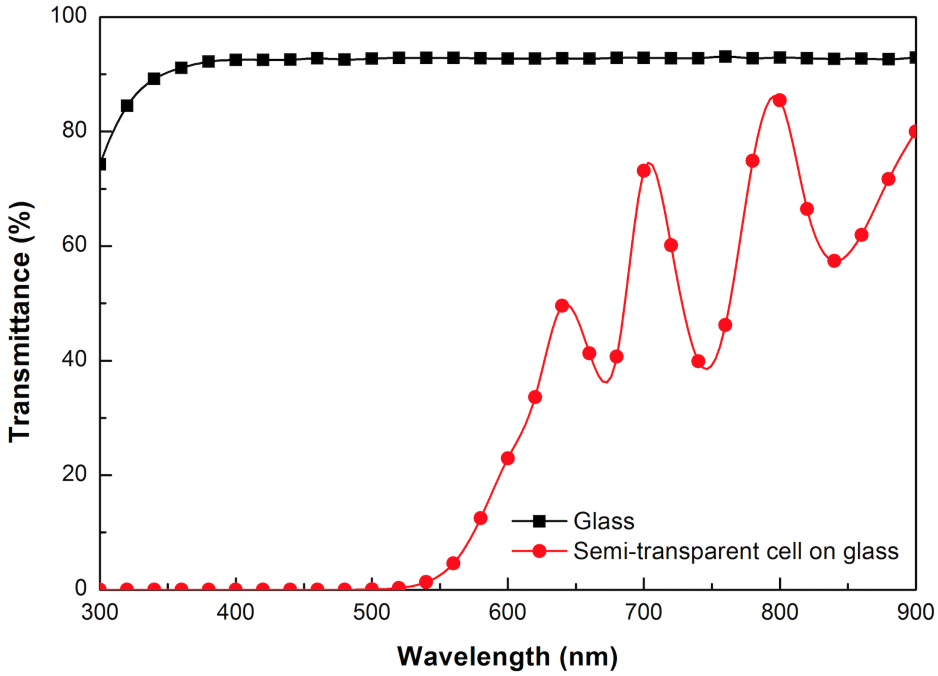

Figure 6.2: Comparison of transmittance spectra of a semi-transparent a-Si:H p-i-n solar cell fabricated on glass and a bare glass substrate.

6.1.1 Performance of semi-transparent vs̀tandard solar cells

Figure 6.3 shows (a) J-V characteristics and (b) spectral response of semi-transparent a-Si:H p-i-n solar cell fabricated on glass substrate, along with standard a-Si:H p-i-n solar cell as a comparison. Device performance parameters are listed in Table 6.1. We achieve a η of $\sim$5 % with J_{sc}, V_{oc}, and FF being 9.93 mA/cm^2, 0.86 V, and 58.10 %, respectively (Figure 6.3(a)). The results confirm the functionality of a-Si:H p-i-n solar cells for BIPV application. Note that the semi-transparent solar cell performance is better than that for standard a-Si:H p-i-n solar cells (J_{sc} of 8.88 mA/cm^2, V_{oc} of 0.885 V, FF of 52.01 %, and η of 4.09 %) fabricated in Chapter 5 (Table 6.1). There are still open questions why the semi-transparent solar cells show better performance because higher J_{sc} and FF are expected for

the standard p-i-n solar cells with a Al back contact due to its high conductivity and better back reflectivity. It is assumed that this may be due to solar cell layers (a-Si:H layers) by ion bombardment Al back contact sputtering, thus degrading solar cell performance. EQE reaches the maximum value of 68.02 % at 530 nm (Figure 6.3(b)). The results confirmed that the EQE is high over the entire wavelength region from 400 to 650 nm. There is no presence of interference fringes in the wavelength range above 600 nm related to the cell reflection spectra [66], because of high transparency of AZO film compared to opaque metal.

Table 6.1: Device performance parameters comparison for semi-transparent a-Si:H p-i-n solar cell and standard a-Si:H p-i-n solar cell.

Cell	Semi-transparent a-Si:H p-i-n solar cell	Standard a-Si:H p-i-n solar cell
V_{oc} (V)	0.86	0.885
J_{sc} (mA/cm^2)	9.93	8.88
FF (%)	58.10	52.01
η (%)	4.98	4.09

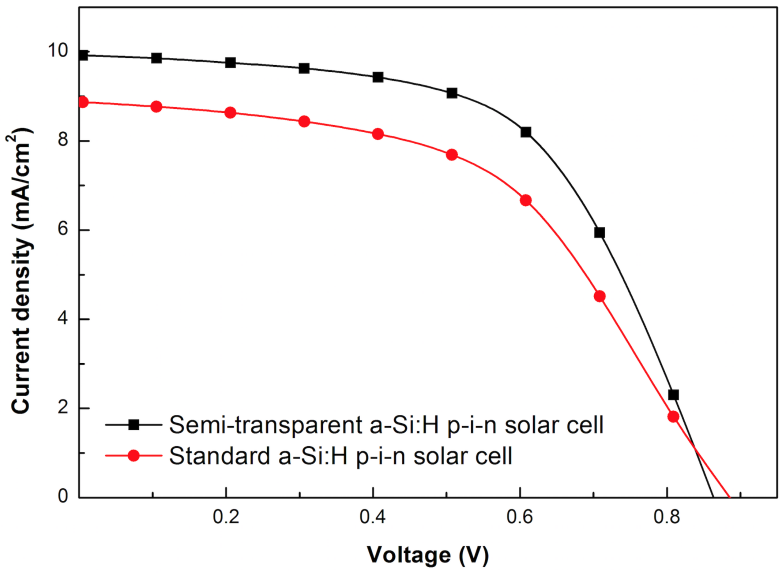

(a)

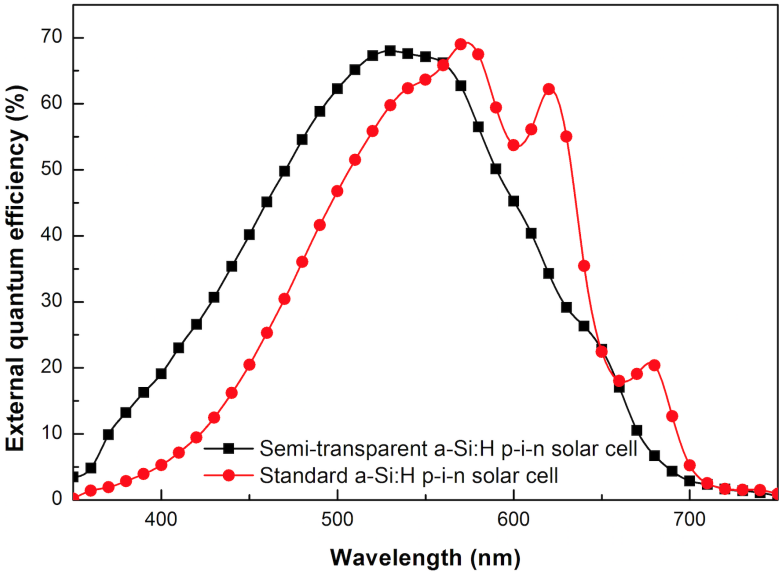

(b)

Figure 6.3: (a) J-V characteristics and (b) spectral response of semi-transparent a-Si:H p-i-n solar cell fabricated on glass substrate.

6.2 Semi-transparent a-Si:H p-i-n solar cells on plastic substrate

Following the results from section 6.1, the fabrication process was transferred from glass to PEN substrate. In the course of fabrication process, the front AZO film was found to be cracked (Figure 6.4) after deposition and subsequent 30-minute cooling. This was attributed to thermal stress between plastic substrate and AZO film [75]. In order to overcome this issue, barrier-layer was deposited before depositing AZO film. In our study, we deposited 100 nm thick a-SiO_x:H thin-films grown by PECVD on PEN plastic substrate as barrier-layers not only to suppress stress issue but also to improve adhesion issue. The barrier-layer properties were characterized by visual inspection and optical transmission [76].

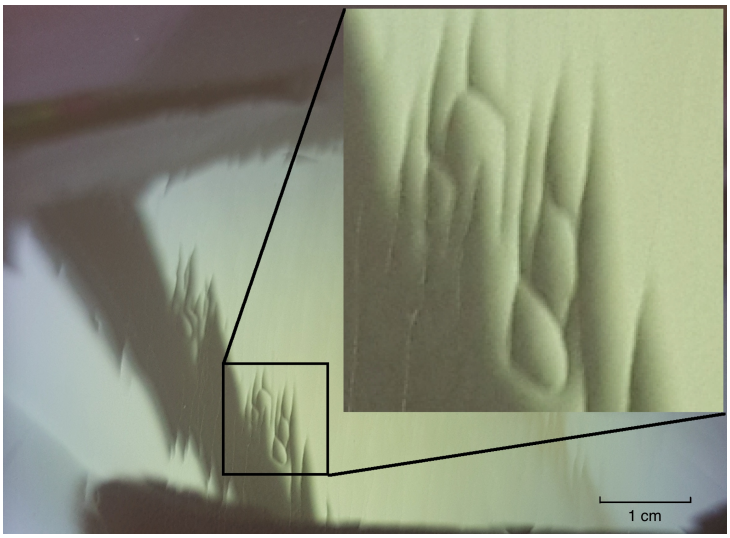

Figure 6.4: The cracked AZO film on PEN substrate (after deposition with 30-minute cooling).

We observed no cracks in AZO film over the substrate surface when using barrier-layer.

In addition, the average transparency of PEN substrate with a-SiO_x:H barrier-layer was measured to be above 60 % in the visible wavelength region as shown in Figure 6.5, which is ∼15 % lower than that of bare PEN substrate. Using AZO film with barrier-layer, we fabricated semi-transparent a-Si:H p-i-n solar cells on PEN substrates using the same deposition recipes as mention in section 6.1.

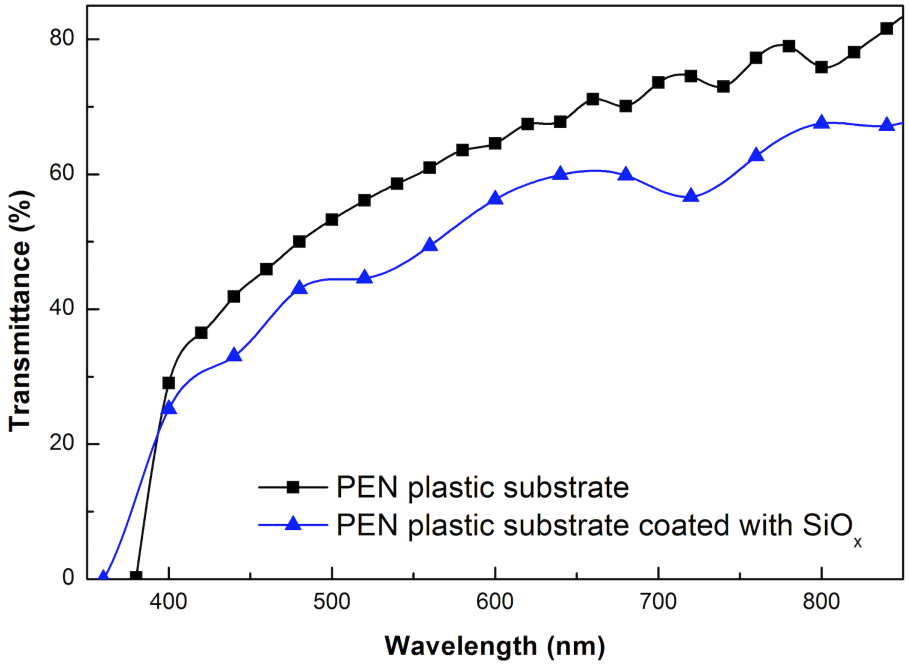

Figure 6.5: The average transparency of PEN substrate with a-SiO_x:H barrier-layer.

The photograph of (a) flat and (b) bent semi-transparent a-Si:H p-i-n solar cells fabricated on PEN substrate is shown in Figure 6.6.

In addition, Figure 6.7 shows transmittance spectra of bare PEN substrate, a-SiO_x:H barrier-layer coated PEN, and semi-transparent a-Si:H p-i-n solar cell fabricated on a-SiO_x:H coated PEN substrate. The average transparency decreases by 10 % for each samples 80 %, 60 %, 50 %, however, the a-Si:H p-i-n solar cells are still semi-transparent

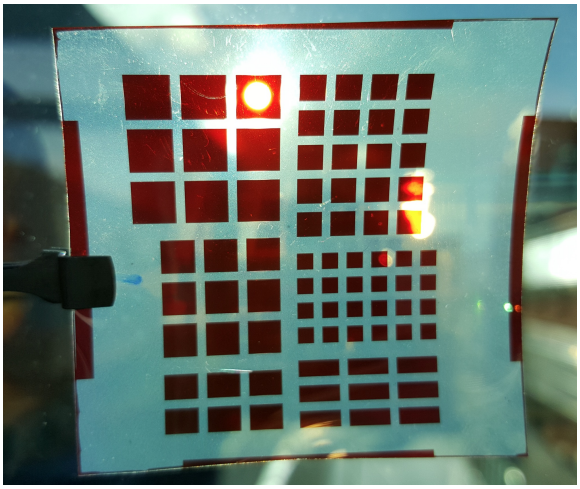

(a)

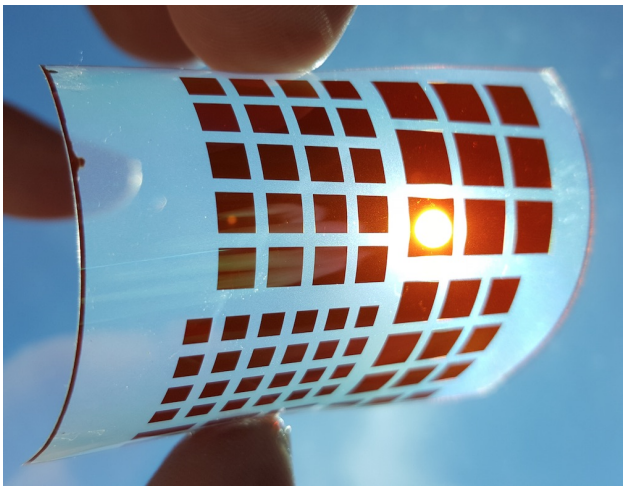

(b)

Figure 6.6: Photograph of (a) flat and (b) bent semi-transparent a-Si:H p-i-n cells fabricated on PEN substrate.

in the visible range (over 600 nm wavelength region).

Figure 6.8 shows (a) J-V characteristics and (b) spectral response characteristics of semi-transparent a-Si:H p-i-n solar cells fabricated on plastic substrate. a-SiO_x:H barrier-

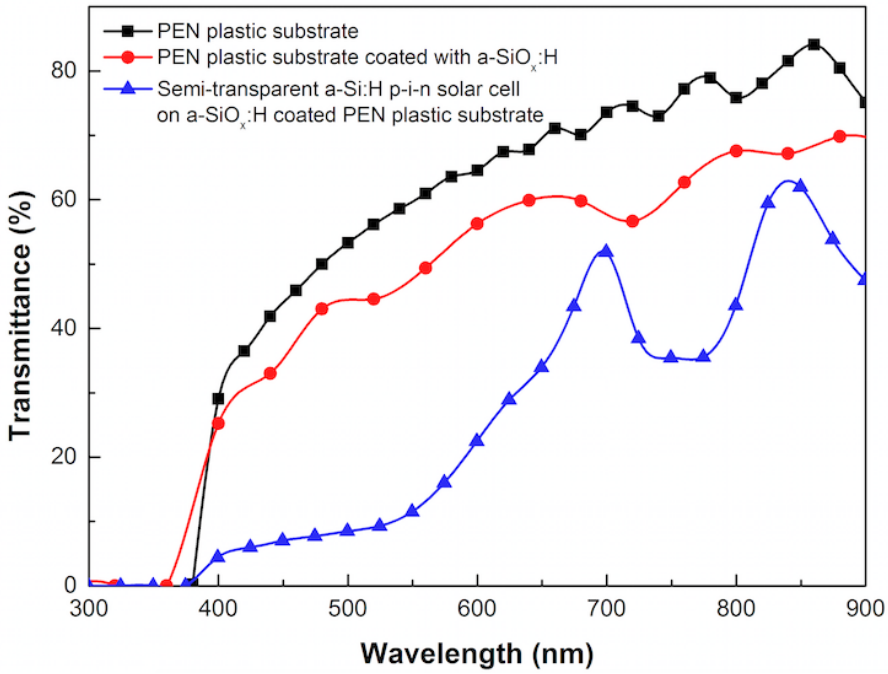

Figure 6.7: Transmittance spectra of bare PEN plastic substrate, a-SiO$_x$:H barrier-layer coated PEN, and semi-transparent p-i-n solar cell fabricated on a-SiO$_x$:H coated PEN plastic substrate.

layer acts as antireflective layer, hence improving J_{sc} [77]. We achieve η of ~4.6 % that J_{sc}, V_{oc}, and FF are 10.535 mA/cm^2, 0.795 V, and 55.02 %, respectively (device performance in Figure 6.8(a)). The EQE reaches the maximum value of 65.50 % at 550 nm (Figure 6.8(b)). The results confirmed that EQE is similar to that of semi-transparent a-Si:H p-i-n solar cells fabricated on glass substrate.

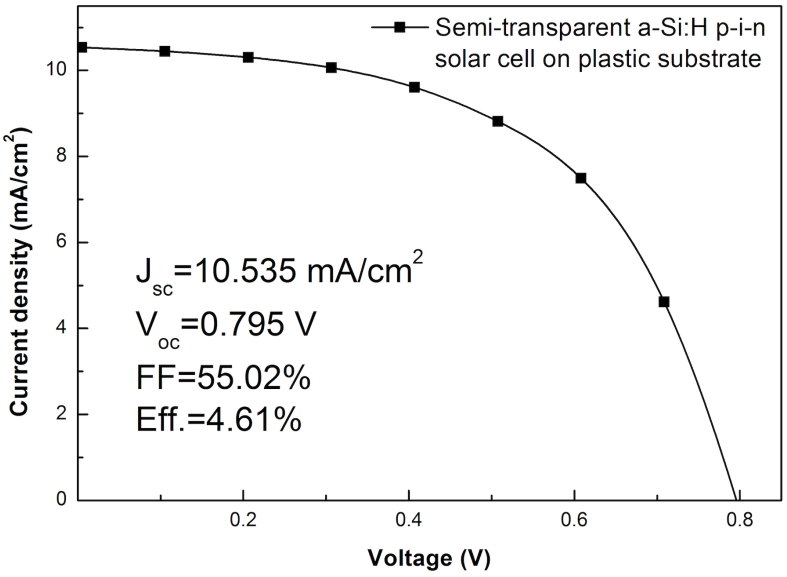

(a)

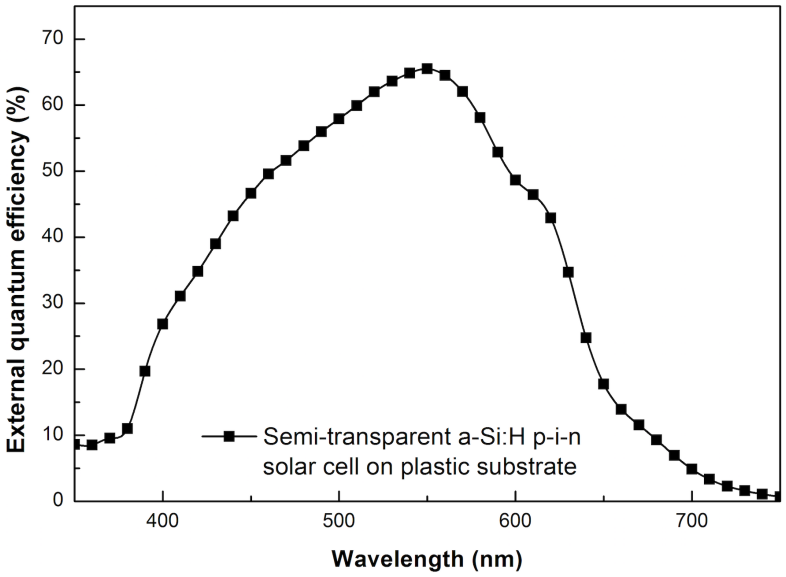

(b)

Figure 6.8: (a) J-V characteristics and (b) spectral response characteristics of semi-transparent a-Si:H p-i-n solar cells on plastic substrate.

6.3 Semi-transparent a-Si:H solar cell as a photodetector

Semi-transparent a-Si:H p-i-n solar cells are known to have very low dark current and does not require cooling hence can be used as radiation detector [78]. The objective for this application is to develop an inexpensive and portable a-Si detector with the response in the visible part of the spectrum [79].

Inductively coupled plasmas (ICPs) are widely-used for elemental analysis. Generally, an ICP uses 15∼20 L/min of Ar gas and consumes 1∼2 kW of electrical power [80]. In addition, due to their size and weight, typical ICPs are used not portable. Miniaturized, light-weight and small-size plasmas (or micro-plasmas) could potentially be used for chemical analysis on-site [81]. Unlike ICPs, micro-plasmas consume 250 mL of an inert gas (such as: Ar and Ne), and they can be operated from a battery due to electrical power consumption of 10∼15 W [79]. Thus, micro-plasmas are suitable for chemical analysis on-site.

Figure 6.9 demonstrates (a) photograph of micro-plasma and (b) the testing system component. A coin has been included for size comparison, and the micro-plasma fits inside the letter A (Figure 6.9(a)). The micro-plasma was formed between two electrodes 1 and 2 (E1 and E2) initially used as a spectral lamp, and securely fastened at the entrance slit of the monochromator. One spectrometer (left hand side of Figure 6.9(b)) was a scanning monochromator with the a-Si detector affixed to its exit slit. The other spectrometer (right hand side of Figure 6.9(b)) was a portable spectrometer, with a charge coupled device (CCD) detector and a fiber optic cable to guide light emission from the micro-plasma onto its entrance slit.

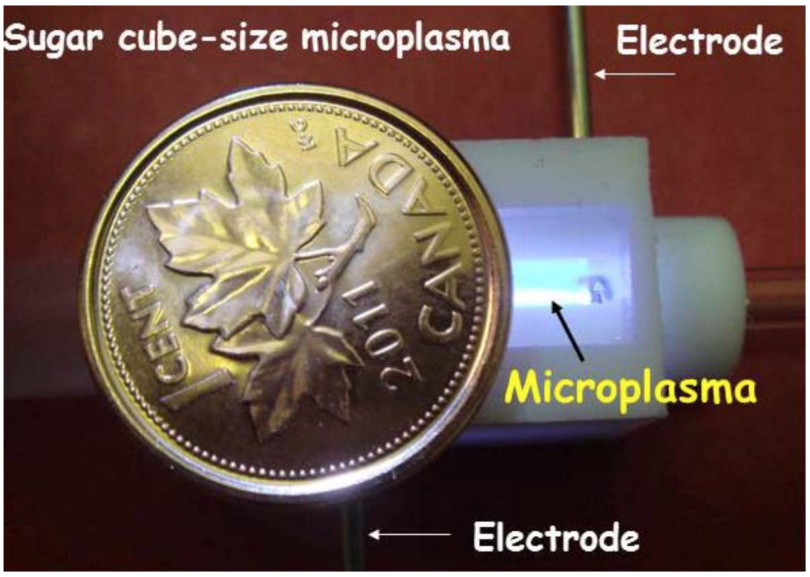

(a)

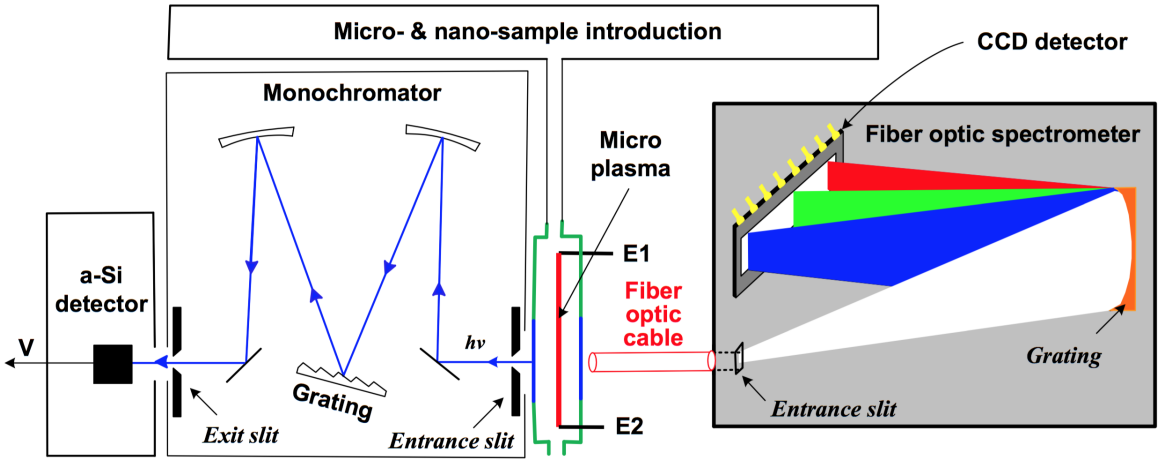

(b)

Figure 6.9: (a) Photograph of micro-plasma and (b) the testing system component.

The width of the entrance and exit slits were adjusted to 1000 μm, so that the spectral bandpass of the monochromator matched approximately that of the spectrometer with a

fiber optic cable. The voltage output from the a-Si detector was amplified 2000 times using a voltage amplifier (model SRS-560) designed by Stanford Research Systems. The voltage output of the amplifier was digitized [78]. The fiber optic spectrometer (from StellarNet Inc.) had an entrance slit of 25 μm and a focal length of 12 cm. The fiber optic spectrometer was equipped with a 600 μm diameter fiber optic cable and a 2048-pixel CCD detector.

Figure 6.10 shows the comparison of the micro-plasma spectral background obtained using both spectrometers. From availability of Ne spectral lines, it can be concluded that the detector is sensitive to visible light, at least between about 580 nm and 700 nm. Ne spectral line around 650 nm perfectly fitted between the a-Si detector (on the monochromator) and the CCD detector of the fiber optic spectrometer.

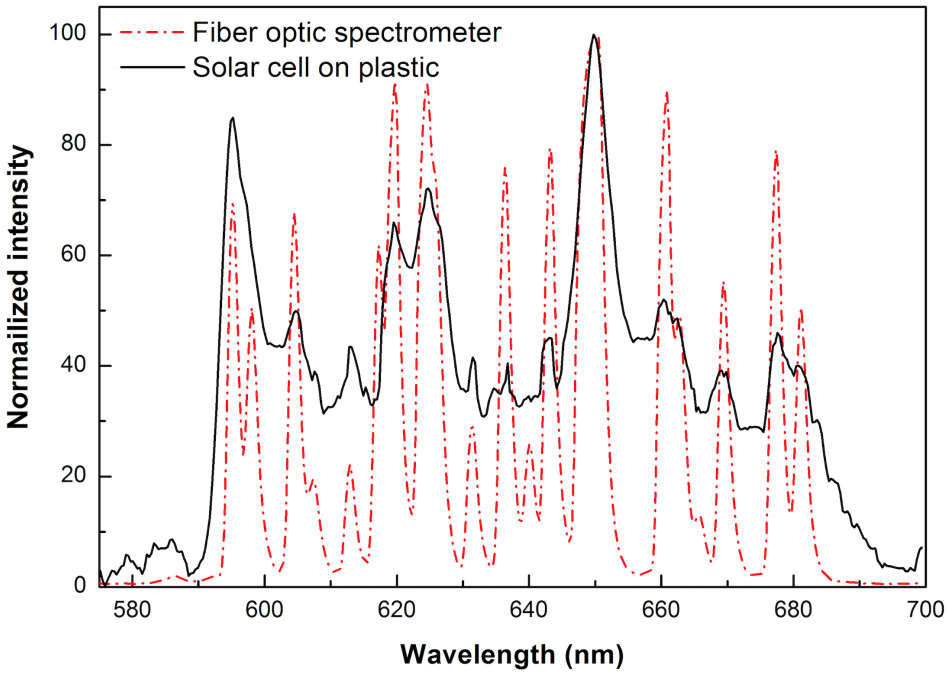

Figure 6.10: The comparison of the micro-plasma spectral background obtained using both spectrometers.

The a-Si detector used in this study is mainly designed as a solar cell, and the device size is not well fitted to receive all optical signal. In order to improve the sensitivity of a-Si detector, further characterization processing is needed.

6.4 Chapter summary

In this chapter, semi-transparent p-i-n solar cells were fabricated on glass and plastic substrates. A barrier-layer was introduced into cell fabrication on plastic substrate to enhance the adhesion, and details of different barrier-layers were studied. We found a-SiO_x:H is very important because of its great absorption for optical index, for this reason,

less recombination happened, and gave an significant improvement of J_{sc} [77].

The results for efficiency tested agree with previously reported values for a-Si:H p-i-n solar cells. The best measured efficiency was 4.98 % for a semi-transparent a-Si:H p-i-n solar cell fabricated on glass substrate, and 4.77 % on plastic substrate with a 0.6 of transmittance. A 6.3 % semi-transparent solar cell fabricated on glass substrate was reported with textured intrinsic a-Si:H layer, and the transmittance was 0.114 [82].

The semi-transparent a-Si:H p-i-n solar cell was also used as a-Si detector with the response in the visible part of the spectrum. From the Ne spectral lines, the micro-plasma spectral from a-Si detector obtained similar response comparable with fiber optic detector.

Chapter 7

Conclusion and Future Work

a-Si:H solar cells based on both substrate and superstrate configurations have been fabricated on glass and plastic substrates at the maximum substrate temperature of 150 °C.

Intrinsic a-Si:H film shows σ_{photo} of 3.3×10^{-5} $(\Omega\text{cm})^{-1}$ and σ_{dark} of 5.47×10^{-10} $(\Omega\text{cm})^{-1}$, yielding the photoresponse of a 6×10^{4}. p-a-SiC:H window layer was introduced to enhance V_{oc} and J_{sc}. For large-are applications, a-Si:H n-i-p PV modules (10×10 cm^2 active area and 72 sub-cells) were fabricated using the developed deposition recipes for small-scale devices. The contact layers such as Al and AZO films were simulated to have low Joule loss in module operation. 200 nm AZO film was found to be the optimized thickness. Typical module performance was V_{oc} of 13.10 V, J_{sc} of 7.66 mA/cm^2, FF of 55.18 %, and η of 3.08 %. It is found that the PV module performance is similar to that of single solar cells, showing scalability of module process.

We also fabricated a-Si:H p-i-n solar cells on glass substrate. Here the a-Si:H stack was inverted from n-i-p structure in the first part of the study. From an initial result,

several efficiency refinements were carried out to have better device performance. a-Si:H p-i-n solar cells with p-type buffer-layer produced V_{oc} of 0.885 V, J_{sc} of 8.88 mA/cm^2, FF of 52.01 %, and η of 4.09 %.

Furthermore, we demonstrated semi-transparent a-Si:H p-i-n solar cells using TCO back electrodes instead of opaque metal for functional BIPV applications. Semi-transparent a-Si:H p-i-n cells were showing η of 4.98 % on glass substrate with transmittance of 60 % in the wavelength range of 500∼800 nm. For plastic substrates, a barrier-layer was introduced to improve adhesion, and 4.77 % efficient semi-transparent a-Si:H p-i-n solar cells were demonstrated. Additionally, semi-transparent a-Si:H p-i-n solar cells were used as detectors with the response in the visible part of the spectrum. From availability of Ne spectral lines, the comparison of micro-plasma spectral between a-Si detector and fiber optic detector obtained similar response.

Based on our results in the study, it is believed that a-Si:H thin films should be a good candidate to produce high efficient energy harvesting on the low-cost and large-area substrate applications such as glass and even plastic.

7.1 Recommendations for the future work

The work performed in our study on a-Si:H solar cells provides a large scope for further investigation. Solar cells on plastic substrates were only developed to the point of being functional on the PEN plastic with high yield. The processing requires characterization with respect to use flexible masks in "reel to reel" system. This would further reduce the module cost. Higher conductive AZO film may be characterized to reduce the series resistance. Semi-transparent a-Si:H p-i-n solar cells can be fabricated into PV modules in

the future. In addition, design and fabrication process can be further characterized on solar cells to be suited for functional detectors. For possible inclusion in future, inexpensive and lightweight micro-plasma based spectrometry systems are being developed for use on-site.

Additionally, the investigation into low temperature deposition of a-Si:H films could be extended to lower temperatures. The use of H_2 dilution and higher RF powers could compensate for defects created by the reduced temperatures, the deposition temperature of 75 °C would be a sensible target as it would enable use of a greater variety of plastics that are cheaper than PEN substrate.

Bibliography

[1] D. M. Chapin, C. S. Fuller, and G. L. Pearson. "A new silicon p-n junction photocell for converting solar radiation into electrical power". *Journal of Applied Physics*, 25(5):676–677, 1954.

[2] Czang-Ho Lee. "ECE 639: Characteristics and Applications of Amorphous Silicon. Lecture 9: Solar Cells", 2014.

[3] Martin A. Green, Keith Emery, Yoshihiro Hishikawa, Wilhelm Warta, Dunlop, and Ewan D. "Solar cell efficiency tables (Version 45)". *Prog. Photovolt: Res. Appl.*, 15(Version 45), 2015.

[4] James R. Sites. "Device Physics of Thin-film Polycrystalline Cells and Modules". (September 2001):1–59, 2004.

[5] R. A. Street. *"Hydrogenated Amorphous Silicon"*. Cambridge University Press, Cambridge, 1991.

[6] Solar Energy. "Photovoltaics report". (November), 2015.

[7] Todd Foley, Kane Thornton, Rainer Hinrichs-rahlwes, Steve Sawyer, Marietta Sander, Richard Taylor, Sven Teske, Harry Lehmann, Marcel Alers, and David Hales. *"Renewable 2015: Global status report"*. 2015.

[8] Pradeep Chakraborty. "PC's Solar Photovoltaics Blog: Yingli gains crown as top producer in 36 GW global PV market", Mar 2016.

[9] M. Shiao. "Thin Film 2012-2016: Technologies, Markets and Strategies for Survival". *GTM Research*, 2012.

[10] M. A. Green. "Recent developments in photovoltaics". *Solar Energy*, 76(1-3):3–8, 2004.

[11] A. V. Shah, M. Vanecek, J. Meier, F. Meillaud, J. Guillet, D. Fischer, C. Droz, X. Niquille, S. Fay, E. Vallat-Sauvain, V. Terrazzoni-Daudrix, and J. Bailat. "Basic efficiency limits, recent experimental results and novel light-trapping schemes in a-Si:H, μc-Si:H and 'micromorph tandem' solar cells". *Journal of Non-Crystalline Solids*, 338:639–645, 2004.

[12] M. Kondo, I. Yoshida, K. Saito, M. Matsumoto, T. Suezaki, H. Sai, and T. Matsui. "Development of Highly Stable and Efficient Amorphous Silicon Based Solar Cells". *28th European Photovoltaic Solar Energy Conference and Exhibition*, pages 2213–2217, Nov 2013.

[13] Panasonic Newsroom Global. "Panasonic HIT Solar Cell Achieves World's Highest Energy Conversion Efficiency of 25.6% at Research Level", Apr 2014.

[14] Barry P. Rand, Jan Genoe, Paul Heremans, and Jef Poortmans. "Solar Cells Utilizing Small Molecular Weight Organic Semiconductors". *Prog. Photovolt: Res. Appl.*, 15:659–676, 2007.

[15] Mario Pagliaro, Giovanni Palmisano, and Rosaria. Ciriminna. "Flexible Solar Cells". 2008.

[16] Https://order.universitywafer.com/default.aspx?cat=Silicon. "University wafer: Silicon wafer price", [accessed on May 11, 2016].

[17] Nandar Lynn, Lipi Mohanty, and Stephen Wittkopf. "Color rendering properties of semi-transparent thin-film PV modules". *Building and Environment*, 54:148–158, 2012.

[18] Jun Han, Lin Lu, and Hongxing Yang. "Numerical evaluation of the mixed convective heat transfer in a double-pane window integrated with see-through a-Si PV cells with low-e coatings". *Applied Energy*, 87(11):3431–3437, 2010.

[19] P. G. O'Brien, A. Chutinan, P. Mahtani, K. Leong, G. A. Ozin, and N. P. Kherani. "Selectively transparent and conducting photonic crystal rear-contacts for thin-film silicon-based building integrated photovoltaics". *Optics Express*, 19(18):17040, 2011.

[20] Won Jae Lee, Easwaramoorthi Ramasamy, Dong Yoon Lee, and Jae Sung Song. "Grid type dye-sensitized solar cell module with carbon counter electrode". *Journal of Photochemistry and Photobiology A: Chemistry*, 194(1):27–30, 2008.

[21] Hideo Otaka, Michie Kira, Kentaro Yano, Shunichiro Ito, Hirofumi Mitekura, Toshio Kawata, and Fumio Matsui. "Multi-colored dye-sensitized solar cells". *Journal of Photochemistry and Photobiology A: Chemistry*, 164(1-3):67–73, 2004.

[22] Hung-Jen Yang, Chien-Hsun Chen, Wei-Cheng Lai, Chien-Liang Wu, Chien-Fu Huang, Yu-Hung Chen, and Jenn-Chang Hwang. "Adjusted Colorful Amorphous Silicon Thin Film Solar Cells by a Multilayer Film Design". *Journal of The Electrochemical Society*, 158(9):H851, 2011.

[23] D. E. Carlson and C. R. Wronski. "Amorphous silicon solar cell". *Applied Physics Letters*, 28(11):671, Aug 1976.

[24] Y. Tawada. "a-SiC:H/a-Si:H heterojunction solar cell having more than 7.1% conversion efficiency". *Applied Physics Letters*, 39(3):237, 1981.

[25] H. W. Deckman. "Optically enhanced amorphous silicon solar cells". *Applied Physics Letters*, 42(11):968, Jun 1983.

[26] R. R. Arya and D. E. Carlson. "Amorphous silicon PV module manufacturing at BP solar". *Progress in Photovoltaics: Research and Applications*, 10(2):69–76, Mar 2002.

[27] Sarah Kurtz. "Photovoltaic Module Reliability Workshop 2011". (November), 2013.

[28] Yukimi Ichikawa, Takashi Yoshida, Toshio Hama, Hiroshi Sakai, and Kouichi Harashima. "Production technology for amorphous silicon-based flexible solar cells". *Solar Energy Materials and Solar Cells*, 66(1-4):107–115, Feb 2001.

[29] S. Guha, J. Yang, and A. Banerjee. "Amorphous silicon alloy photovoltaic research: present and future". *Progress in Photovoltaics: Research and Applications*, 8(1):141–150, Jan 2000.

[30] J. Meier, S. Dubail, R. Fluckiger, D. Fischer, H. Keppner, and A. Shah. "Intrinsic microcrystalline silicon (μc-Si:H)-a promising new thin film solar cell material". In *Proceedings of 1994 IEEE 1st World Conference on Photovoltaic Energy Conversion - WCPEC (A Joint Conference of PVSC, PVSEC and PSEC)*, volume 1, pages 409–412. IEEE, 1994.

[31] J. Meier, S. Dubail, J. Cuperus, U. Kroll, R. Platz, P. Torres, J.A. Anna Selvan, P. Pernet, N. Beck, N. Pellaton Vaucher, C. Hof, D. Fischer, H. Keppner, and A. Shah. "Recent progress in micromorph solar cells". *Journal of Non-Crystalline Solids*, 227-230:1250–1256, May 1998.

[32] Kenji Yamamoto, Masashi Yoshimi, Yuko Tawada, Yoshifumi Okamoto, and Akihiko Nakajima. "Thin film Si solar cell fabricated at low temperature". *Journal of Non-Crystalline Solids*, 266-269:1082–1087, May 2000.

[33] J. Meier, U. Kroll, S. Dubail, S. Golay, S. Fay, J. Dubail, and A. Shah. "Efficiency enhancement of amorphous silicon p-i-n solar cells by LP-CVD ZnO". In *Conference Record of the Twenty-Eighth IEEE Photovoltaic Specialists Conference - 2000 (Cat. No.00CH37036)*, pages 746–749. IEEE, 2000.

[34] J. Müller, B. Rech, G. Schöpe, V. Sittinger, M. Ruske, O. Kluth, H. Schade, G. Bräuer, T. Höing, P. Lechner, X. Jiang, B. Szyszka, and R. Geyer. "Large area mid-frequency magnetron sputtered ZnO films as substrates for silicon thin-film solar cells". 2002.

[35] J. Meier, U. Kroll, J. Spitznagel, S. Benagli, T. Roschek, G. Pfanner, C. Ellert, G. Androutsopoulos, A. Hugli, M. Nagel, C. Bucher, L. Feitknecht, G. Buchel, and A. Buchel. "Progress in up-scaling of thin film silicon solar cells by large-area PECVD KAI systems". In *Conference Record of the Thirty-first IEEE Photovoltaic Specialists Conference, 2005.*, pages 1464–1467, 2005.

[36] T. Söderström, F.-J. Haug, V. Terrazzoni-Daudrix, and C. Ballif. "Development of Micromorph Tandem solar cells on flexible low cost plastic substrates". *20th EU Photovoltaic Solar Energy Conference*, pages 1529–1532, 2009.

[37] J. W. Lim, D. J. Lee, and S. J. Yun. "Semi-Transparent Amorphous Silicon Solar Cells Using a Thin p-Si Layer and a Buffer Layer". *ECS Solid State Letters*, 2(6):Q47–Q49, 2013.

[38] R. A. Street. "Doping and the Fermi Energy in Amorphous Silicon". 49, 1982.

[39] Xunming Deng and Eric Schiff. *"Amorphous Silicon-based Solar Cells"*. 2003.

[40] Jef Poortmans and Vladimir Arkhipov. *"Thin Film Solar Cells Fabrication , Characterization and Applications"*, volume 1. 2006.

[41] Harvey Scher and Elliott N. Montroll. "Anomalous transit-time dispersion in amorphous solids". 12, Sep 1975.

[42] Bhushan Sopori. "Thin-film Silicon Solar Cells". 8:1193–1196, 2003.

[43] Ruud E. I. Schropp and Miro Zeman. "Amorphous and Microcrystalline Silicon Solar Cells: Modeling, Materials and Device Technology". Jan 1998.

[44] Czang-Ho Lee. "Nanocrystalline Silicon Thin-Film Transistors". 2006.

[45] Jérôme Perrin, Akihisa Matsuda, Katsuhiko Nomoto, Yoshiaki Takeuchi, Atsushi Suzuki, and Akimasa Yuuki. "Temperature dependence of the sticking and loss probabilities of silyl radicals on hydrogenated amorphous silicon". *Surface Science*, 227(1-2):50–56, Mar 1990.

[46] Grazia Cicala. *"Plasma Deposition of Amorphous Silicon-Based Materials"*. Elsevier, 1995.

[47] Yasutake Toyoshima, Kazuo Arai, Akihisa Matsuda, and Kazunobu Tanaka. "In situ characterization of the growing a-Si:H surface by IR spectroscopy". *Journal of Non-Crystalline Solids*, 137-138:765–770, Jan 1991.

[48] E. A. G. Hamers, J. Bezemer, and W. F. Van der Weg. "Positive ions as growth precursors in plasma enhanced chemical vapor deposition of hydrogenated amorphous silicon". *Applied Physics Letters*, 75(5):609, Aug 1999.

[49] R. A. Street. *"Technology and Applications of Amorphous Silicon"*. Springer Science & Business Media, 2000.

[50] M. Moravej and Et al. "Plasma enhanced chemical vapour deposition of hydrogenated amorphous silicon at atmospheric pressure". *Plasma Sources Science and Technology*, 13(1):8, 2004.

[51] Petra Cameron. "Solar Energy", Aug 2013.

[52] S. Bowden and A. Rohatgi. "Rapid and Accurate Determination of Series Resistance and Fill Factor Losses in Industrial Silicon Solar Cells".

[53] Siva Sivoththaman and Andrei Sazonov. "ECE 632: Photovoltaic Energy Conversion". *University of Waterloo course notes*, (9), 2013.

[54] Lumen Electronic Jewelry. "Solar cells: a powerful sandwich!", Apr 2016.

[55] http://www.solardirect.com/pv/pvlist/pvlist.htm. "Solar Electric Photovoltaic Modules", [accessed on May 12, 2016].

[56] Polymerdatabase.com. "Properties of Polyesters", [accessed on May12, 2016].

[57] Http://www.teijindupontfilms.jp/english/product/pen_teo.html. "Teonex® - PEN Film - Teijin DuPont Films", [accessed on May 12, 2016].

[58] T. F. Schulze. "Structural, electronic and transport properties of amorphous/crystalline silicon heterojunctions". *Thesis Silizium-Photovoltaik*, pages 1–268, 2011.

[59] Czang-Ho Lee, William S. Wong, Andrei Sazonov, and Arokia Nathan. "Study of deposition temperature on high crystallinity nanocrystalline silicon thin films with in-situ hydrogen plasma-passivated grains". *Thin Solid Films*, 597:151–157, 2015.

[60] Hyun Jung Lee. "Top-Gate Nanocrystalline Silicon Thin Film Transistors". 2008.

[61] R. C. Chittick, J. H. Alexander, and H. F. Sterling. "The Preparation and Properties of Amorphous Silicon". *Journal of The Electrochemical Society*, 116(1):77, Jan 1969.

[62] Jeung Hun Park, Jong Moon Shin, Su-Young Cha, Jin Woo Park, and Se-Young Jeong. "Deposition-temperature effects on AZO thin films prepared by RF magnetron sputtering and their physical properties". *Journal of the Korean Physical Society*, 49:584–588, Dec 2006.

[63] Vladimír Tvarožek, Pavel Šutta, Ivan Novotný, Peter Ballo, Ladislav Harmatha, Soa Flickyngerová, Lucie Prušáková, Marie Netrvalová, Veronika Vavruková, Andrea Pullmannová, Erik Vavrinský, Pavol Gašpierik, and Miroslav Mikolášek. "Preparation of transparent conductive AZO thin films for solar cells". *ASDAM 2008 - Conference Proceedings of the 7th International Conference on Advanced Semiconductor Devices and Microsystems*, pages 275–278, 2008.

[64] N. Song, X. Hao, J. Huang, Z. Liu, X. Liu, S. Huang, and M. Green. "Film Thickness and Substrate Temperature Effects on Sputtered Al:ZnO Window Layer for Cu_2ZnSnS_4 Thin Film Solar". *COMMAD 2012*, pages 153–154, Dec 2012.

[65] Hung-wei Wu, Chien-hsun Chu, Yu-fu Chen, Yung-wei Chen, Wu-han Tsai, Shih-hua Huang, and Guan-syun Chen. "Study of AZO Thin Films Under Different Ar Flow and Sputtering Power by rf Magnetron". II:13–16, 2013.

[66] Sergey Varlamov, Jing Rao, and Thomas Soderstrom. "Polycrystalline silicon thin-film solar cells with plasmonic-enhanced light-trapping". *Journal of visualized experiments : JoVE*, (65), Jan 2012.

[67] Seung Yeop Myong, Sang Soo Kim, and Koeng Su Lim. "In situ ultraviolet treatment in an Ar ambient upon p-type hydrogenated amorphous silicon-carbide windows of hydrogenated amorphous silicon based solar cells". *Applied Physics Letters*, 84(26):5416–5418, 2004.

[68] E. V. Johnson, F. Dadouche, M. E. Gueunier-Farret, J. P. Kleider, and P. Roca I. Cabarrocas. "Open-circuit voltage increase dynamics in high and low deposition rate polymorphous silicon solar cells". *Physica Status Solidi (a)*, 207(3):691–694, 2010.

[69] Seungsin Baek, Jeong Chul Lee, Youn-Jung Lee, Sk Md Iftiquar, Youngkuk Kim, Jinjoo Park, and Junsin Yi. "Interface modification effect between p-type a-SiC:H and ZnO:Al in p-i-n amorphous silicon solar cells". *Nanoscale research letters*, 7:81, Jan 2012.

[70] Sunghyun Moon, Kangho Kim, Youngjo Kim, Junseok Heo, and Jaejin. Lee. "Highly efficient single-junction GaAs thin-film solar cell on flexible substrate". 2016.

[71] Yang, Gi-Chul and A., Sio-Iong and Gelman, Len. *"Transactions on Engineering Technologies: Special Volume of the World Congress on Engineering 2013"*. Springer Science & Business, 2014.

[72] Liang Fang, Seung Jae Baik, Koeng Su Lim, Seung Hyup Yoo, Myung Soo Seo, Sang Jung Kang, and Jung Won Seo. "Tungsten oxide as a buffer layer inserted at the SnO_2/p-a-SiC interface of pin-type amorphous silicon based solar cells". *Applied Physics Letters*, 96(19):193501, May 2010.

[73] Jinjoo Park, Vinh Ai Dao, Chonghoon Shin, Hyeongsik Park, Minbum Kim, Junhee Jung, Doyoung Kim, and Junsin Yi. "A buffer-layer/a-SiO_x:H(p) window-layer optimization for thin film amorphous silicon based solar cells". *Thin Solid Films*, 546:331–336, Nov 2013.

[74] Ji Eun Lee, Joo Hyung Park, Jun-Sik Cho, Jin-Won Chung, Jinsoo Song, Donghwan Kim, and Jeong Chul Lee. "Analysis on the interfacial properties of transparent conducting oxide and hydrogenated p-type amorphous silicon carbide layers in p-i-n amorphous silicon thin film solar cell structure". *Thin Solid Films*, 520(18):6007–6011, July 2012.

[75] M. Dosmailov, L. N. Leonat, J. Patek, D. Roth, P. Bauer, M. C. Scharber, N. S. Sariciftci, and J. D. Pedarnig. "Transparent conductive ZnO layers on polymer substrates: Thin film deposition and application in organic solar cells". *Thin Solid Films*, 591:97–104, 2015.

[76] T. N. Chen, D. S. Wuu, C. C. Wu, C. C. Chiang, Y. P. Chen, and R. H. Horng. "High-Performance Transparent Barrier Films of SiO_x/SiN_x Stacks on Flexible Polymer Substrates". *Journal of The Electrochemical Society*, 153(10):F244, 2006.

[77] N Sahouane, A Zerga, and I Bensefia. "Influence of SiN_x:H and SiO_x Films on Optical and Electrical Properties of Antireflective Coatings for Silicon Solar Cells". *International Journal of Scientific & Technology Research*, 3(7):3–8, 2014.

[78] Shiva Abbaszadeh, Karim S. Karim, and Vassili Karanassios. "Measurement of UV from a microplasma by a microfabricated amorphous selenium detector", 2013.

[79] Vassili Karanassios, Kara Johnson, and Andrea T. Smith. "Micromachined, planar-geometry, atmospheric-pressure, battery-operated microplasma devices (MPDs) on chips for analysis of microsamples of liquids, solids, or gases by optical-emission spectrometry". *Analytical and bioanalytical chemistry*, 388(8):1595–604, Aug 2007.

[80] Robert Thomas. "Practical Guide to ICP-MS: A Tutorial for Beginners, Third Edition", 2013.

[81] Vassili Karanassios. "Microplasmas for chemical analysis: analytical tools or research toys?". *Spectrochimica Acta Part B: Atomic Spectroscopy*, 59(7):909–928, Jul 2004.

[82] Young Tae Chae, Jeehwan Kim, Hongsik Park, and Byungha Shin. "Building energy performance evaluation of building integrated photovoltaic (BIPV) window with semi-transparent solar cells". *Applied Energy*, 129:217–227, 2014.

[83] Neamen. *"Semiconductor Physics And Devices"*. 1992.

[84] K. M. Azizur Rahman. "Nanocrystalline Silicon Solar Cells Deposited via Pulsed PECVD at 150 °C Substrate Temperature". *Solar Cells*, 2010.

[85] G. M. Ablayev, A. S. Abramov, I. A. Nyapshaev, Y. K. Vygranenko, R. Yang, A. Y. Sazonov, M. Z. Shvarts, and E. I. Terukov. "Flexible photovoltaic modules based on amorphous hydrogenated silicon". *Semiconductors*, 49(5):679–682, 2015.

[86] W. E. Spear and P. G. Le Comber. "Electronic properties of substitutionally doped amorphous Si and Ge". *Philosophical Magazine*, 33(6):935–949, Jun 1976.

[87] J. Meier, J. Spitmagel, U. Kroll, C. Bucher, S. Fay, T. Moria, and A. Shah. "High-efficiency amorphous and "micromorph" silicon solar cells". pages 2801–2805, 2003.

[88] Jenny Nelson. *"The Physics of Solar Cells (Properties of Semiconductor Materials)"*. 2003.

[89] Michael M. Adachi. "Low Temperature Thin Film Silicon Solar". *Solar Energy Materials and Solar Cells*, 2007.

[90] Matthias Pospiech and Sha Liu. “The Physics Behind Laser Diodes”.

[91] P. W. Anderson. “Absence of diffusion in certain random lattices”, 1958.

[92] Denis Striakhilev, Arokia Nathan, Yuri Vygranenko, Peyman Servati, Czang-Ho Lee, and Andrei. Sazonov. “Amorphous Silicon Display Backplanes on Plastic Substrates”. *Journal of Display Technology*, 2:364–371, 2006.